

**THE DEVELOPMENT OF SUPPORTED ELECTROCATALYSTS FOR THE  
OXIDATION OF FUELS IN HYDROXIDE EXCHANGE MEMBRANE  
FUEL CELLS**

by

Elizabeth G. Mahoney

A dissertation submitted to the Faculty of the University of Delaware in partial fulfillment of the requirements for the degree of Doctor of Philosophy in Chemical Engineering

Summer 2015

© 2015 Elizabeth G. Mahoney  
All Rights Reserved

ProQuest Number: 3730241

All rights reserved

INFORMATION TO ALL USERS

The quality of this reproduction is dependent upon the quality of the copy submitted.

In the unlikely event that the author did not send a complete manuscript and there are missing pages, these will be noted. Also, if material had to be removed, a note will indicate the deletion.



ProQuest 3730241

Published by ProQuest LLC (2015). Copyright of the Dissertation is held by the Author.

All rights reserved.

This work is protected against unauthorized copying under Title 17, United States Code  
Microform Edition © ProQuest LLC.

ProQuest LLC.  
789 East Eisenhower Parkway  
P.O. Box 1346  
Ann Arbor, MI 48106 - 1346

**THE DEVELOPMENT OF SUPPORTED ELECTROCATALYSTS FOR THE  
OXIDATION OF FUELS IN HYDROXIDE EXCHANGE MEMBRANE  
FUEL CELLS**

by

Elizabeth G. Mahoney

Approved: \_\_\_\_\_  
Abraham M. Lenhoff, Ph.D.  
Chair of the Department of Chemical and Biomolecular Engineering

Approved: \_\_\_\_\_  
Babatunde A. Ogunnaike, Ph.D.  
Dean of the College of Engineering

Approved: \_\_\_\_\_  
James G. Richards, Ph.D.  
Vice Provost for Graduate and Professional Education

I certify that I have read this dissertation and that in my opinion it meets the academic and professional standard required by the University as a dissertation for the degree of Doctor of Philosophy.

Signed:

---

Jingguang G. Chen, Ph.D.  
Professor in charge of dissertation

I certify that I have read this dissertation and that in my opinion it meets the academic and professional standard required by the University as a dissertation for the degree of Doctor of Philosophy.

Signed:

---

Yushan Yan, Ph.D.  
Member of dissertation committee

I certify that I have read this dissertation and that in my opinion it meets the academic and professional standard required by the University as a dissertation for the degree of Doctor of Philosophy.

Signed:

---

Raul Lobo, Ph.D.  
Member of dissertation committee

I certify that I have read this dissertation and that in my opinion it meets the academic and professional standard required by the University as a dissertation for the degree of Doctor of Philosophy.

Signed:

---

Feng Jiao, Ph.D.  
Member of dissertation committee

## ACKNOWLEDGMENTS

First, I would like to extend my sincere gratitude to my advisors Dr. Jingguang Chen and Dr. Yushan Yan for their support over the past several years. I have learned a lot about what it means to do research during my time at the University of Delaware and it is because of their guidance that I feel confident going forward. Dr. Lobo and Dr. Feng Jiao have also provided me with helpful advice and suggestions as my committee members. Additionally, I would not have been able to learn electrochemistry without the extensive help and training of Dr. Wenchao Sheng, Dr. Emily Carino, and Dr. Dan Esposito. Furthermore, thanks to everyone in the Chen and Yan research groups, including Dr. Yannick Kimmel, Mariah Woodroof, Jarrid Wittkopf, Dr. Laj Xiong, Robert Kaspar, Myat Myint, Marc Porosoff, Ke Xiong, Dr. Weiting Yu, Bobby Forrest, Kevin Lee, Lu Wang, Weiming Wan, Chris Hawxhurst, Elaine Gomez, and Brian Tackett for being such exceptional people to work with. I would also like to thank the entire Department of Chemical and Biomolecular Engineering for helping to create such a positive research environment: George Whitmyre and Gary Wellmaker for their much needed assistance with the distillation column, Kathie Young, and all of the teachers I have had over the years.

My graduate experience would have been incomplete without the friends I have met at both the University of Delaware and Columbia. All of them have become so important to me both as friends I will cherish for life as well as fellow scientists with whom I can discuss research problems and idea. In addition, my family has been with me through both the good times and the bad over the past few years. Many

thanks to my mother and father, Laurie George and Robert Mahoney, as well as my sisters Kathryn Mahoney and Claire Mahoney. I'm eternally grateful to have your continued love and support. Finally, I'd like to thank my husband Zack Whiteman for his dedication, patience, and amazing cooking as we both finish our dissertations together.

## TABLE OF CONTENTS

LIST OF TABLES .....	ix
LIST OF FIGURES .....	xi
ABSTRACT .....	xviii

### Chapter

1	INTRODUCTION .....	1
1.1	More Efficient Sources of Energy and Benefits of Fuel Cell Systems .....	1
1.2	The Transition from Acidic to Alkaline Fuel Cells .....	4
1.3	The Hydrogen Oxidation Reaction (HOR) and Hydrogen Evolution Reaction (HER) .....	10
1.4	Research Strategy and Thesis Scope .....	13
2	EXPERIMENTAL METHODS .....	16
2.1	Electrocatalyst Preparation .....	16
2.1.1	Disk Electrodes .....	16
2.1.2	Electrodes for Supported Electrocatalysts .....	17
2.1.3	Incipient Wetness Impregnation .....	21
2.2	Characterization Techniques .....	22
2.2.1	Transmission Electron Microscopy (TEM) .....	22
2.2.2	X-ray Photoelectron Spectroscopy (XPS) .....	23
2.2.3	Fourier Transform Infrared Spectroscopy (FTIR) .....	24
2.3	Electrochemical Techniques .....	25
2.3.1	Three cell set up .....	25
2.3.2	Voltammetric Techniques .....	27
2.3.2.1	Cyclic Voltammetry (CV) and Linear Sweep Voltammetry (LSV) .....	27
2.3.2.2	Chronoamperometry (CA) .....	28
2.3.2.3	Electrochemical Impedance Spectroscopy (EIS) .....	29

2.3.3	Galvanic Displacement of a Cu Monolayer with Pt.....	31
2.3.4	Determining Electrochemically Active Surface Area .....	31
2.3.4.1	CV Peaks .....	31
2.3.4.2	CO Stripping.....	33
2.3.4.3	Cu Stripping.....	35
2.3.5	Rotating Disk Electrode (RDE) Configuration .....	37
2.3.6	HER/HOR Kinetic Analyses .....	41
2.3.7	Determining Activity of Oxygenate Electrooxidation .....	46
3	<b>SUPPORTED MONOMETALLIC AND BIMETALLIC ELECTROCATALYSTS FOR HYDROGEN OXIDATION IN ALKALINE ELECTROLYTES .....</b>	<b>48</b>
3.1	Supported Electrode Preparation.....	48
3.2	HOR/HER Results on Monometallic Disks and Supported Electrodes ..	49
3.2.1	Ag disk and 40% Ag/C.....	49
3.2.2	Au disk and 40% Au/C.....	54
3.2.3	Co disk and 20% Co/C .....	57
3.2.4	Cu disk and 20% Cu/C .....	60
3.2.5	20% Ir/C .....	63
3.2.6	Ni disk and 60% Ni/C.....	66
3.2.7	Pt disk and 46% Pt/C:.....	68
3.2.8	Pd disk and 40% Pd/C .....	73
3.2.9	20% Rh/C .....	76
3.2.10	W and Fe Disks .....	79
3.3	Volcano Relationship for Supported Monometallic Catalysts .....	80
4	<b>PLATINUM-MODIFIED GOLD ELECTROCATALYSTS FOR THE ALKALINE HYDROGEN OXIDATION REACTION .....</b>	<b>88</b>
4.1	Synthesis of Cu/Au via Cu Underpotential Deposition.....	89
4.2	Characterization of Pt, Au, and Pt/Au Surfaces .....	95
4.2.1	TEM.....	96
4.2.2	XPS.....	97
4.2.3	Cyclic Voltammetry .....	98
4.2.4	Determination of Electrochemically Active Surface Area .....	100
4.2.4.1	Pt H-UPD and AuO Integration .....	101
4.2.4.2	CO Stripping.....	101

4.2.4.3	Comparison of Voltametric and CO Stripping Techniques for Pt/Au.....	105
4.3	HER/HOR Activity of Pt/Au and Pt/Au/C.....	107
5	PLATINUM-MODIFIED TRANSITION METAL CARBIDES FOR THE ALKALINE HYDROGEN OXIDATION REACTION.....	112
6	PLATINUM-MODIFIED GOLD ELECTROCATALYSTS FOR THR OXIDATION OF ETHYLENE GLYCOL AND GLUCOSE.....	124
6.1	Ethylene Glycol Oxidation on Pt/Au Surfaces.....	125
6.1.1	Electrochemical Activity.....	125
6.1.2	Mechanistic Interpretation of EGO on Pt/Au Using FTIR.....	129
6.2	Glucose Oxidation on Pt/Au Surfaces.....	132
6.2.1	Electrochemical Activity.....	132
6.2.2	Mechanistic Interpretation of EtO on Pt/Au Using FTIR.....	136
6.3	Ethanol Oxidation on Pt/Au Surfaces.....	140
6.3.1	Electrochemical Activity.....	140
6.3.2	Mechanistic Interpretation of EtO on Pt/Au Using FTIR.....	143
7	CONCLUSIONS AND FUTURE DIRECTIONS.....	147
	REFERENCES.....	152
	Appendix	
	PERMISSION LETTERS.....	160

## LIST OF TABLES

Table 3.1: Summary of ink recipes used for monometallic supported catalysts. ....	49
Table 3.2: Calculated roughness factors, exchange current densities, and Tafel slopes for each Ag disk and 40% Ag/C electrode.....	52
Table 3.3: Calculated roughness factors, exchange current densities, and Tafel slopes for each Au disk and 40% Au/C electrode.....	56
Table 3.4: Calculated roughness factors, exchange current densities, and Tafel slopes for each Au disk and 40% Au/C electrode.....	59
Table 3.5: Calculated roughness factors, exchange current densities, and Tafel slopes for each Cu disk and 40% Cu/C electrode. ....	62
Table 3.6: Calculated roughness factors and exchange current densities (using both the Butler-Volmer equation and the Tafel equation) for 20% Ir/C...	65
Table 3.7: Calculated roughness factors, exchange current densities, and Tafel slopes for each Ni disk and 60% Ni/C electrode. ....	67
Table 3.8: Calculated roughness factors, exchange current densities, and Tafel slopes for each Pt disk and 46% Pt/C electrode.....	71
Table 3.9 Calculated roughness factors, exchange current densities, and Tafel slopes for each Pt disk and 46% Pt/C electrode.....	75
Table 3.10: Calculated roughness factors and exchange current densities (using both the Butler-Volmer equation and the Tafel equation) for 20% Rh/C. ....	78
Table 3.11: Calculated exchange current densities and Tafel slopes for each W and Fe disk electrode. ....	79
Table 3.12: Summary of hydrogen binding energies, exchange current densities and Tafel slopes for each disk and supported catalyst electrode. The Fe and W disks are normalized by the geometric area of the disk only. ....	83

Table 4.1: Calculated roughness factors and electrochemical surface areas for Au, Pt and Pt/Au catalysts. ....	105
Table 4.2: The HER/HOR exchange current densities for each electrode in 0.1 M KOH, normalized by the electrochemical surface area for each metal...	108
Table 5.1: Ink recipes used for 5% Pt/TMC catalysts. ....	113
Table 5.2: Roughness factors calculated for each Pt/TMC catalyst using copper stripping. ....	116
Table 5.3: Measured exchange current densities for each 5% Pt/TMC catalyst. The Tafel slope or transfer coefficient is also listed for each depending on whether the Tafel or Butler-Volmer method was used, respectively.	121
Table 6.1: Peak assignments for the FTIR spectra of EGO. ....	131
Table 6.2: Peak assignments for the IR spectra of GlcO.....	138
Table 6.3: Peak assignments for the IR spectra of EtO.....	145

## LIST OF FIGURES

Figure 1.1: Gravimetric energy densities of common fuels compared to lead acid batteries. The value for the battery is too low to be shown.[1] .....	2
Figure 1.2: Department of Energy goals for PEMFC development until 2020 and beyond. Figure taken from Reference [8] .....	3
Figure 1.3: Schematic of a proton exchange membrane fuel cell (PEMFC).....	5
Figure 1.4: Estimation of kinetic losses for HOR and ORR in a PEMFC using kinetic parameters from literature.[1,9].....	6
Figure 1.5: Schematic of a hydroxide exchange membrane fuel cell (HEMFC). .....	8
Figure 1.6: Estimation of kinetic losses for HOR and ORR in a HEMFC using kinetic parameters from literature.[9].....	9
Figure 1.7: Volcano plot for HOR/HER on bulk monometallic surfaces in acidic electrolytes. Figure taken from reference [14]. .....	12
Figure 1.8: Volcano plot for HOR/HER on bulk monometallic surfaces in alkaline electrolytes. Figure taken from reference [16]. .....	13
Figure 1.9: Research methodology to develop new, practical electrocatalysts. ....	14
Figure 2.1: Visualization of supported electrode preparation. Examples of prepared electrodes are shown, exemplifying (a), (b) poorly prepared electrodes and (c) and ideally prepared electrode. ....	18
Figure 2.2: Illustration of XPS photoelectron emission process. ....	23
Figure 2.3: Three cell configuration including (a) reference electrode, (b) gas sparger, (c) Pt counter electrode, and (d) working electrode. ....	26
Figure 2.4: Illustration of potential control in CV and LSV. ....	27
Figure 2.5: Illustration of potential control in CA.....	29
Figure 2.6: Illustration of the potential signal in EIS. ....	30

Figure 2.7: Sample CVs of 46% Pt/C in 0.1 M KOH using different upper potential limits (red and black curves). .....	32
Figure 2.8: CVs taken at 50 mV/s of 46% Pt/C in 0.5 M H <sub>2</sub> SO <sub>4</sub> with (blue line) and without (black line) 2 mM of CuSO <sub>4</sub> . In the solution containing Cu <sup>2+</sup> ions, both (A) bulk Cu and (B) UPD Cu deposition/stripping are present. ....	36
Figure 2.9: RDE set up including illustration of electrolyte flow toward the disk electrode surface. ....	38
Figure 2.10: Example of a Koutecky-Levich plot at potentials where electron transport is limiting and where mass-transport is limiting ( <i>i<sub>l,c</sub></i> ). ....	40
Figure 2.11: iR-corrected polarization curves of the Pt disk taken at different rotation rates at 10 mV/s. The inset shows the obtained Koutecky-Levich plot. ....	42
Figure 2.12: (a) Pt disk polarization curve at 1600 rpm in 0.1 M KOH for HOR/HER before and after mass-transport correction in the HOR branch. (b) Fit of the Butler-Volmer equation to the polarization curve data. ....	43
Figure 2.13: Example Tafel plot for the Pt disk at 1600 rpm in 0.1 M KOH. The grey line is the obtained polarization curve. The red line is the data selected for the linear fit to obtain log( <i>i</i> <sub>0</sub> ) and the Tafel slope. ....	45
Figure 3.1: (a) CV of Ag disk in deaerated 0.1 M KOH taken at 50 mV/s. (b) CA at 1.16 V vs. RHE corresponding to the formation of a monolayer of either AgOH or Ag <sub>2</sub> O. The dashed line indicates the baseline of integration for surface area calculation. (c) LSV of Ag disk in H <sub>2</sub> -saturated 0.1 M KOH taken at 10 mV/s (grey line) and the data used for Tafel analysis (red line). ....	50
Figure 3.2: (a) CV of 40% Ag/C in deaerated 0.1 M KOH taken at 50 mV/s. (b) CA at 1.16 V vs. RHE corresponding to the formation of a monolayer of either AgOH or Ag <sub>2</sub> O. The dashed line indicates the baseline of integration for surface area calculation. (c) LSV of Ag disk in H <sub>2</sub> -saturated 0.1 M KOH taken at 10 mV/s (grey line) and the data used for Tafel analysis (red line). ....	51

Figure 3.3: Comparison of LSVs for the Ag disk and 40% Ag/C electrode normalized by active Ag area. The substantially higher activity of Ag/C is apparent from the increased HOR current at positive potentials. ....	53
Figure 3.4: (a) CV of Au disk in deaerated 0.1 M KOH taken at 50 mV/s. (b) LSV of Au disk in H <sub>2</sub> -saturated 0.1 M KOH taken at 10 mV/s (grey line) and the data used for Tafel analysis (red line).....	55
Figure 3.5: (a) CV of 40% Au/C in deaerated 0.1 M KOH taken at 50 mV/s. (b) LSV of 40% Au/C in H <sub>2</sub> -saturated 0.1 M KOH taken at 10 mV/s (grey line) and the data used for Tafel analysis (red line). ....	55
Figure 3.6: Comparison of LSVs for the Au disk and 40% Au/C electrode normalized by active Au area. The substantially higher activity of Au/C is apparent from the increased HOR current at positive potentials. ....	57
Figure 3.7: (a) CVs of Co disk at varying scan rates. The surface area was calculated by plotting the current at 0.92 V vs. RHE. The slope of that line divided by the specific capacitance gives the surface area. (b) LSV at 1600 rpm used for Tafel analysis.....	58
Figure 3.8: (a) CVs of 20% Co/C disk at varying scan rates. The surface area was calculated by plotting the current at 0.92 V vs. RHE. 20% of the slope of that line divided by the specific capacitance gives the surface area. (b) LSV at 1600 rpm used for Tafel analysis. ....	58
Figure 3.9: (a) CVs of the Cu disk in deaerated 0.1 M KOH taken at 50 mV/s with differing upper potential limits represented by different line textures. The red CV was used for surface area determination. (b) LSV of Cu disk in H <sub>2</sub> -saturated 0.1 M KOH taken at 10 mV/s (grey line) and the data used for Tafel analysis (red line). ....	61
Figure 3.10: (a) CVs of 20% Cu/C in deaerated 0.1 M KOH taken at 50 mV/s with differing upper potential limits represented by different line textures. The red CV was used for surface area determination. (b) LSV of 20% Cu/C in H <sub>2</sub> -saturated 0.1 M KOH taken at 10 mV/s (grey line) and the data used for Tafel analysis (red line). ....	61

Figure 3.11: (a) CVs of 20% Ir/C at different upper potential limits. (b) HOR/HER polarization curves taken at 10 mV/s with Koutecky-Levich plot (inset). (c) LSV taken at 1600 rpm (black squares) and the fit to the Butler-Volmer equation (red line). (d) LSV taken at 1600 rpm in H <sub>2</sub> -saturated 0.1 M KOH at 10 mV/s (grey line) and the data used for Tafel analysis (red line).	64
Figure 3.12: (a) CV of Ni disk in deaerated 0.1 M KOH taken at 50 mV/s. (b) LSV of Ni disk in H <sub>2</sub> -saturated 0.1 M KOH taken at 10 mV/s (grey line) and the data used for Tafel analysis (red line).	66
Figure 3.13: (a) CV of 60% Ni/C in deaerated 0.1 M KOH taken at 50 mV/s. (b) LSV of 60% Ni/C in H <sub>2</sub> -saturated 0.1 M KOH taken at 10 mV/s (grey line) and the data used for Tafel analysis (red line).	67
Figure 3.14: (a) CVs of the Pt disk at different upper potential limits. (b) HOR/HER polarization curves taken at 10 mV/s with Koutecky-Levich plot (inset). (c) LSV taken at 1600 rpm (black squares) and the fit to the Butler-Volmer equation (red line). (d) LSV taken at 1600 rpm in H <sub>2</sub> -saturated 0.1 M KOH at 10 mV/s (grey line) and the data used for Tafel analysis (red line).	69
Figure 3.15: (a) CVs of 46% Pt/C at different upper potential limits. (b) HOR/HER polarization curves taken at 10 mV/s with Koutecky-Levich plot (inset). (c) LSV taken at 1600 rpm (black squares) and the fit to the Butler-Volmer equation (red line). (d) LSV taken at 1600 rpm in H <sub>2</sub> -saturated 0.1 M KOH at 10 mV/s (grey line) and the data used for Tafel analysis (red line).	70
Figure 3.16: (a) CV of Pd disk in 0.1 M KOH. (b) LSV taken at 1600 rpm in H <sub>2</sub> -saturated 0.1 M KOH at 10 mV/s (grey line) and the data used for Tafel analysis (red line).	73
Figure 3.17: (a) CV of 40% Pd/C in 0.1 M KOH. (b) HOR/HER polarization curves taken at 10 mV/s with Koutecky-Levich plot (inset). (c) LSV taken at 1600 rpm (black squares) and the fit to the Butler-Volmer equation (red line). (d) LSV taken at 1600 rpm in H <sub>2</sub> -saturated 0.1 M KOH at 10 mV/s (grey line) and the data used for Tafel analysis (red line).	74

Figure 3.18: (a) CVs of 20% Rh/C at different upper potential limits. (b) HOR/HER polarization curves taken at 10 mV/s with Koutecky-Levich plot (inset). (c) LSV taken at 1600 rpm (black squares) and the fit to the Butler-Volmer equation (red line). (d) LSV taken at 1600 rpm in H <sub>2</sub> -saturated 0.1 M KOH at 10 mV/s (grey line) and the data used for Tafel analysis (red line).	77
Figure 3.19: (a) LSV taken at 1600 rpm in H <sub>2</sub> -saturated 0.1 M KOH (grey line) and the data used for Tafel analysis on the W disk. (b) LSV taken at 1600 rpm in H <sub>2</sub> -saturated 0.1 M KOH at 10 mV/s (grey line) and the data used for Tafel analysis (red line) on the Fe disk.	79
Figure 3.20: LSVs of (a),(b) monometallic disk electrodes and (c),(d) supported monometallic electrodes. The current densities are normalized both by the geometric and actual area of the electrode.	81
Figure 3.21: Tafel plots of (a),(b) monometallic disk electrodes and (c),(d) supported monometallic electrodes. The current densities are normalized both by the geometric and actual area of the electrode.	82
Figure 3.22: Volcano plot of monometallic disk and supported electrodes.	84
Figure 4.1: Cu underpotential deposition on an Au substrate.	91
Figure 4.2: CVs of the Au disk in 0.05 M H <sub>2</sub> SO <sub>4</sub> with and without 0.05 M CuSO <sub>4</sub> . Potential limits were chosen to show (a) Cu bulk deposition and UPD as well as (b) Cu UPD only.	92
Figure 4.3: CVs of the 40% Au/C electrode in 0.05 M H <sub>2</sub> SO <sub>4</sub> with and without 0.05 M CuSO <sub>4</sub> . Potential limits were chosen to show (a) Cu bulk deposition and UPD as well as (b) Cu UPD only.	94
Figure 4.4: Particle size distributions and transmission electron micrographs (inset) of (a) Au/C and (b) Pt/C. The Pt particles and Au particles are approximately 2.5 ± 0.6 nm and 14 ± 6.9 nm in diameter, respectively.	96
Figure 4.5: Pt 4f XPS spectra of the Pt/Au disk. Both Pt <sup>0</sup> and Pt <sup>4+</sup> species are observed, as marked by vertical dashed lines.	98
Figure 4.6: Cyclic voltammograms (CVs) of (a) disk electrodes and (b) supported catalysts on glassy carbon electrodes in Ar-purged 0.1 M KOH. The CVs for Au samples and Pt samples are taken at 100 mV/s and 50 mV/s, respectively.	100

Figure 4.7:	CO stripping and background curves for the (a) Au, (b) Pt, and (c) Pt/Au disks. Each was obtained at 20 mV/s in 0.1 M KOH. The Pt/Au sample shows similar CO stripping characteristics to bulk Pt. ...	102
Figure 4.8:	CO stripping and background curves for (a) Au/C, (b) Pt/C, and (c) Pt/Au/C. Each was obtained at 20 mV/s in 0.1 M KOH. The Pt/Au/C sample has more defined CO stripping characteristics than Pt/C. ....	103
Figure 4.7:	iR-corrected polarization curves of HER/HOR on (a) Au disk, Pt disk, Pt/Au disk, (b) Au/C, Pt/C, and Pt/Au/C in H <sub>2</sub> saturated 0.1 M KOH. Kinetic current of HER/HOR on (c) the Pt/Au disk electrode and (d) Pt/Au/C (solid blue line) and their fit to the Butler-Volmer equation (dashed black line). The bulk Pt samples and Pt/Au samples exhibit similar activity and are both superior to the Au samples. Au/C shows higher activity than bulk Au. Both Pt/Au and Pt/Au/C show excellent fit to the Butler-Volmer equation. ....	108
Figure 5.1:	Copper stripping LSVs for each Pt/TMC catalyst as well as 46% Pt/C for comparison. Each LSV has had the background current subtracted. Each catalyst displays the general copper stripping features of Cu. ....	115
Figure 5.2:	Polarization curves and fits to the Butler-Volmer equation for (a),(b) 5% Pt/TiC and (c),(d) 5% Pt/Vc. ....	118
Figure 5.3:	LSVs at 1600 rpm in H <sub>2</sub> -saturated 0.1 M KOH for (a) 5% Pt/NbC, (b) 5% Pt/TaC, and 5% Pt/ZrC. The red lines are the data used for the linear fit and extrapolation to 0 V vs. RHE. ....	120
Figure 5.4:	Exchange current densities of each 5% Pt/TMC catalyst compared to Pt/C (black dotted line). ....	122
Figure 6.1:	CVs taken at 50 mV s <sup>-1</sup> of (a) Pt, Au, and Pt/Au disk electrodes and (b) Pt/C, Au/C, and Pt/Au/C electrodes in deaerated 0.1 M KOH and 1 M EG. ....	126
Figure 6.2:	Chronoamperometry measurements for the Au, Pt, and Pt/Au disk electrodes taken at 0.8 V vs. RHE in 0.1 M KOH and 1 M EG. ....	127
Figure 6.3:	Pt 4f XPS spectra of the Pt/Au disk before and after the EGO CA at 0.8 V vs. RHE for 3600 seconds. The Pt surface remains unchanged after EGO at this potential. ....	128

Figure 6.4:	Selected FTIR spectra of the (a) Au, (b) Pt, and (c) Pt/Au disk electrode during EGO. Spectra were obtained in 0.1 M KOH and 0.2 M EG purged in N <sub>2</sub> while the potential was scanned at 1 mV s <sup>-1</sup> . All potentials are referred to RHE.....	130
Figure 6.5:	CVs taken at 50 mV/s of (a) Pt, Au, and Pt/Au disk electrodes and (b) Pt/C, Au/C, and Pt/Au/C electrodes in Ar-purged 0.1 M KOH and 0.1 M Glc. The inset graphs are zoomed in on the Pt CVs to show more detail. ....	133
Figure 6.6:	CA measurements for the Au, Pt, and Pt/Au disk electrodes taken at 0.4 V vs. RHE in Ar-purged 0.1 M KOH and 0.1 M Glc. ....	135
Figure 6.7:	Selected FTIR spectra of the (a) Au disk, (b) Pt disk, and (c) Pt/Au disk during GlcO. Spectra were obtained in 0.1 M KOH and 0.2 M Glyc purged in N <sub>2</sub> while the potential was scanned at 1 mV/s. ....	137
Figure 6.8:	CVs of the (a) Pt, Au, and Pt/Au disk electrodes and (b) Pt/C, Au/C, and Pt ML/Au/C electrodes in 0.1 M KOH and 1 M EtOH. ....	142
Figure 6.9:	CA measurements for the Au, Pt, and Pt/Au disk electrodes taken at 0.8 V vs. RHE in Ar-purged 0.1 M KOH and 1 M EtOH. ....	143
Figure 6.9:	FTIR spectra of the (a) Au disk, (b) Pt disk, and (c) Pt/Au disk during EtO. Spectra were obtained in 0.1 M KOH and 0.2 M EtOH purged in N <sub>2</sub> . The scan rate was 1 mV/s.....	144

## ABSTRACT

Hydroxide exchange membrane fuel cells (HEMFCs) offer a number of advantages over proton exchange membrane fuel cells. One advantage is the higher stability of catalytic materials in the alkaline environment of a HEMFC, which opens the possibility for using non-platinum (Pt) group metals to catalyze the oxygen reduction reaction (ORR) and the hydrogen oxidation reaction (HOR). However, even on Pt, the activity of the HOR is approximately two orders of magnitude slower in alkaline environments relative to acidic environments. Pt is an expensive catalyst and a cheaper catalyst would greatly lower the cost associated with HEMFCs.

In order to develop novel catalysts for the alkaline HOR, catalytic trends must be established. Previously, trends on monometallic polycrystalline disk electrodes were established using hydrogen binding energies calculated by density functional theory as a thermodynamic descriptor. While these trends have helped develop new, Pt-free catalysts for the alkaline HOR, bulk materials such as disk electrodes are not suitable for fuel cell devices. Therefore, catalytic trends were also developed for monometallic, carbon-supported catalysts, which are able to be directly used in a fuel cell device. Gold, silver, copper, iridium, platinum, palladium, rhodium, nickel, and cobalt nanoparticles on carbon supports were tested for the alkaline HOR reaction. While general trends observed for the disk electrodes also hold for the supported catalysts, the silver, gold, and copper nanoparticles were found to be more active than the respective disk electrodes.

While the trends developed on supported catalysts will help the development of new electrocatalysts, Pt is the most active metal for the alkaline HOR. To decrease the amount of Pt needed, gold (Au) substrates were decorated with Pt nanoparticles and tested for the alkaline HOR. Both Pt-decorated disk Au substrates (Pt/Au) and supported Au substrates (Pt/Au/C) were synthesized through the galvanic displacement of an underpotentially-deposited monolayer of copper on the Au substrate. Characterization of these surfaces through standard electrochemical techniques indicates that Pt is present on the Au surface as small nanostructures. The activities of Pt/Au and Pt/Au/C toward the alkaline HOR were shown to be similar to bulk Pt and far higher than bulk Au, while utilizing much less Pt than state-of-the-art fuel cell catalysts. Pt/Au/C catalysts therefore may be used to decrease the loading of Pt required for HEMFC anodes. Though Pt/Au catalysts offer Pt-like activity while utilizing less Pt, the cost of the catalyst may not decrease significantly since Au is an expensive substrate. Therefore, transition metal carbide (TMC) powders were also impregnated with low loadings of Pt and tested for the alkaline HOR, which will decrease the cost of the catalyst further.

The lack of infrastructure for hydrogen storage and transportation currently limits the practicality of using hydrogen as a fuel source. Nevertheless, HEMFCs also have the benefit of utilizing alternative CO<sub>2</sub>-neutral fuels such as ethylene glycol and glucose. The kinetic activity of the alkaline oxidation of these fuels was determined for Pt/Au catalysts. In addition, the stability of each catalyst was compared to bulk Pt. The Pt/Au catalysts were found to have similar activity as bulk Pt as well as improved stability for the alkaline oxidation of ethylene glycol. The mechanism of each oxidation reaction was examined on the Pt/Au surface using in-situ infrared

spectroscopy. The increased stability of the Pt/Au surface toward the oxidation of ethylene glycol is due to the prevention of C-C bond scission, therefore avoiding the poisoning of Pt active sites.

## Chapter 1

### INTRODUCTION

#### 1.1 More Efficient Sources of Energy and Benefits of Fuel Cell Systems

To address the concerns of increasing atmospheric CO<sub>2</sub> levels, an increasing amount of research has been dedicated to the exploration of alternative energy sources and clean energy conversion technologies. Fuel cells are a possible alternative energy conversion device that achieve efficiencies as high as 40-60%. Fuel cells are electrochemical devices that take advantage of chemical energy stored in certain fuels to produce a usable electric current.

While other renewable sources of energy such as solar, wind, and hydroelectric can theoretically provide unlimited amounts of energy, they are inherently intermittent. In order to rely on renewable sources of energy for all energy demands, a storage device is needed. For example, excess power generated by a solar cell on a sunny day can be stored in a battery system for use at night time. However, batteries have a rather low energy storage capacity when compared to using a chemical fuel, as shown in Figure 1.1. Hydrogen, on the other hand, has a much larger gravimetric energy density than even gasoline. If the excess energy produced via renewable energy sources can instead be stored in the chemical bonds of hydrogen or other molecules, the fuel could later be reused where renewable energy sources are not available. Fuel cells are ideal devices to use this hydrogen to produce useful electrical work.

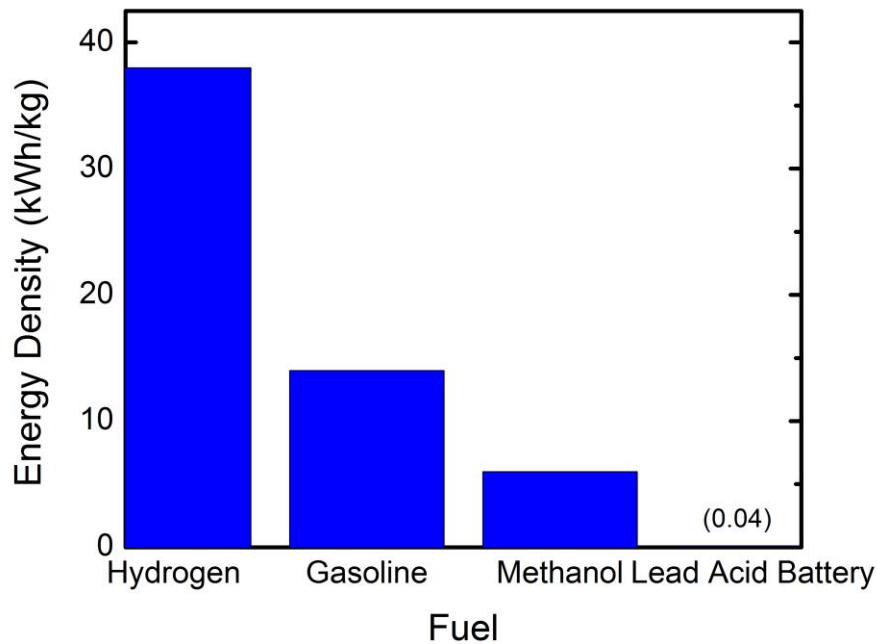


Figure 1.1: Gravimetric energy densities of common fuels compared to lead acid batteries. The value for the battery is too low to be shown.[1]

In addition, fuel cells also provide the benefit of having flexible fuel options that can be tailored to fit a specific need. Among many possible fuel options, hydrogen has been the most studied over the past several decades, but presents concerns associated with its storage and environmentally-unfriendly production routes. However, other feedstock options, particularly oxygen-containing hydrocarbons (i.e., oxygenates), may be more commercially viable due to their compatibility with the existing infrastructure for storage and transportation. Oxygenates that show potential as replacements for hydrogen as a feedstock for fuel cells are methanol, ethanol (Et), ethylene glycol (EG), and glucose (Glc). EG as a fuel cell feedstock is advantageous because it can be produced from non-food competing biomass sources using

inexpensive nickel-based catalysts, rendering the fuel CO<sub>2</sub>-neutral.[2–4] Being one of the simplest oxygenates derived from biomass, it has also been used as a probe molecule to estimate the catalytic behavior for more complicated oxygenates such as Glc, which has the same 1:1 carbon to oxygen ratio as EG.[5,6] Glc is easily produced in nature via photosynthesis in plants, which makes it a promising candidate for a CO<sub>2</sub>-neutral fuel.[7]

Despite the many advantages of fuel cell systems, the technology is still far less widespread than the traditional combustion systems. One reason for this is the prohibitive cost of fuel cells. The United States Department of Energy has established a goal of \$40/kW<sub>net</sub> for fuel cells by 2020, as shown in Figure 1.2. This number

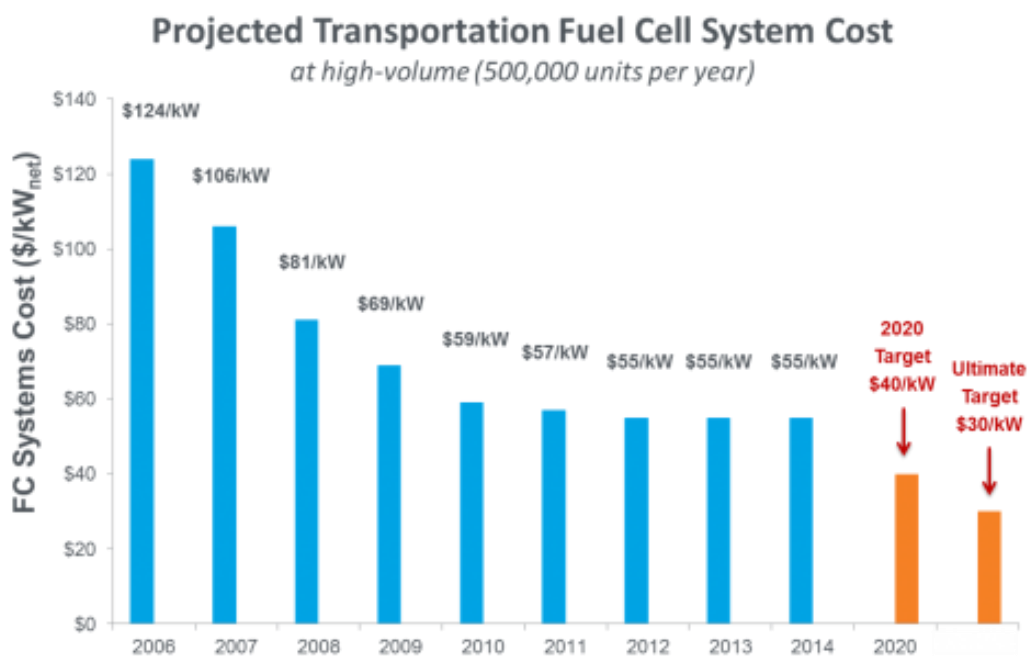


Figure 1.2: Department of Energy goals for PEMFC development until 2020 and beyond. Figure taken from Reference [8]

includes the cost of the fuel cell materials as well as manufacturing and distributions costs. While significant progress has been made since 2006, research is needed to decrease the overall cost.

For a projection of 500,000 fuel cell units per year, approximately 49% of that cost stems from the electrocatalyst cost. Currently, the state-of-the-art fuel cells are proton exchange membrane fuel cells (PEMFCs), which use expensive platinum (Pt) catalysts. Therefore, it is imperative that more efficient and less expensive fuel cell catalysts be developed. One way of doing this is to transition from acidic fuel cells such as PEMFCs to those that operate in alkaline conditions.

## 1.2 The Transition from Acidic to Alkaline Fuel Cells

The overall reaction occurring in a PEMFC is the combination of hydrogen and oxygen to form water:



While the direct combustion of hydrogen and oxygen would produce thermal energy, a fuel cell utilizes the half-cell electrochemical reactions to produce a current. A PEMFC schematic is shown in Figure 1.3. A fuel cell consists of a membrane electrode assembly, or MEA, which includes the electrolyte, electrodes, and electrocatalysts. In the case of PEMFCs, the electrolyte usually used is Nafion, a solid proton conduction polymer. While Nafion conducts protons, it is electrically insulating so that the two electrodes and half-reactions are separated.

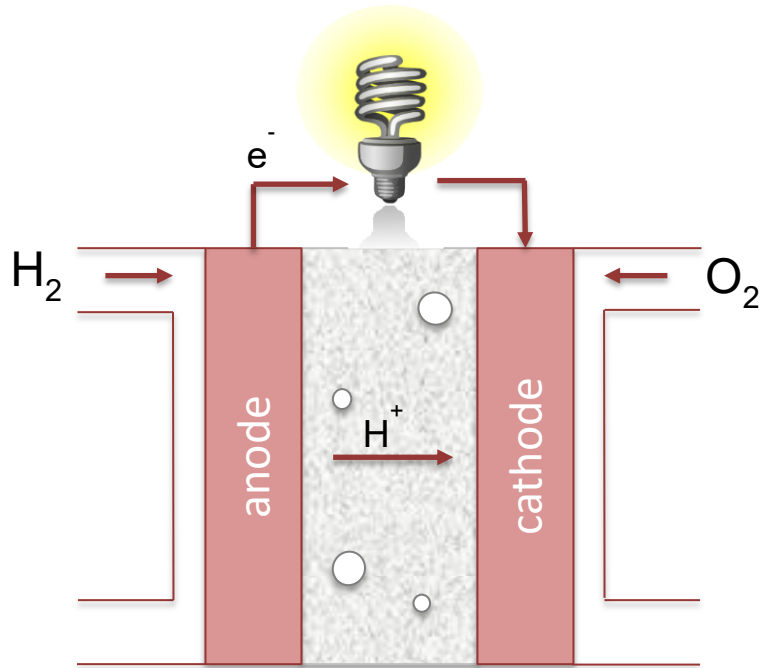


Figure 1.3: Schematic of a proton exchange membrane fuel cell (PEMFC).

The anodic reaction is the oxidation of the fuel, which for the purpose of this introduction will be assumed as hydrogen. In the acidic environment of a PEMFC, the hydrogen oxidation reaction (HOR) can be written as:



which has a standard electrode potential of 0 V vs. Standard Hydrogen Electrode (SHE). The hydrogen is catalytically split on the anode electrocatalyst, which for PEMFCs is generally Pt. Since the membrane is electrically insulating, the electrons produced from this reaction are forced through an external circuit to the cathode, producing a usable current. The protons are then conducted through the membrane.

The half cell reaction at the cathode is the oxygen reduction reaction (ORR):



which has a standard electrode potential of 1.23 V vs. SHE. Here oxygen is reduced on the cathodic electrocatalyst, where it can react with the protons and electrons produced from the hydrogen oxidation reaction to form the exhaustive product, water.

Theoretically, the voltage of the PEMFC should be 1.23 V. However, due to kinetic losses from the electrochemical half reactions, the actual voltage will be much less, as illustrated in Figure 1.3. The actual cell potential depends heavily on the performance of the electrocatalysts. In PEMFCs, the main kinetic losses stem from the ORR reaction, for which Pt-based catalysts are the most effective. However, even

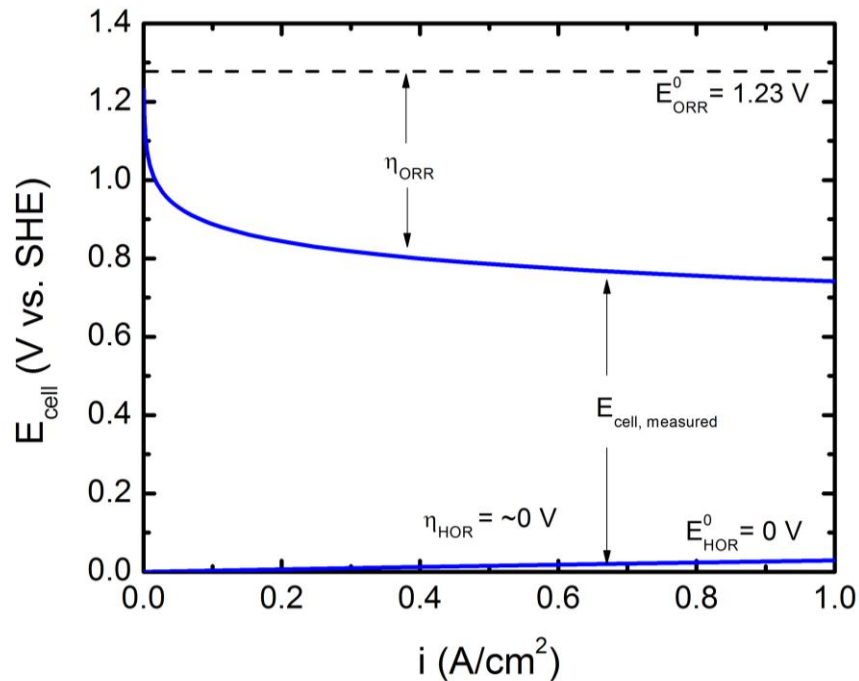


Figure 1.4: Estimation of kinetic losses for HOR and ORR in a PEMFC using kinetic parameters from literature.[1,9]

on Pt, the potential in excess of the standard reaction potential needed to produce a reasonable current density, or the overpotential ( $\eta$ ), is about 300-400 mV. This causes the actual potential of the cell to be much less than the theoretical 1.23 V.

In Figure 1.4, it is clear that the overpotential for the HOR is very low in comparison to the overpotential for ORR. For most commercially-viable PEMFCs, the loading of Pt needed for the anode is on the order of micrograms of Pt nanoparticles. In fact, most PEMFC electrocatalysis research over the past decades has been focused on improving the performance of ORR catalysts.

One of the considerations for PEMFC electrocatalyst development is the acidic environment. At low pH, there are few materials outside of the Pt-group metals that are stable as well as active. Therefore, Pt-based electrocatalysts are considered standard for modern PEMFCs, which is a primary cause for the high total cost of the fuel cell stack.

One way to achieve the Department of Energy fuel cell cost goal is to decrease or eliminate the need for Pt electrocatalysts using an alkaline fuel cell. At high pH, a wider range of inexpensive and abundant electrocatalysts become stable.[10–12] Hydroxide exchange membrane fuel cells (HEMFCs) are an ideal candidate for a PEMFC substitute. As illustrated in Figure 1.5, HEMFCs function similarly to PEMFCs with one main difference: instead of using a proton membrane to conduct protons from the anode to the cathode, a hydroxide exchange membrane is implemented to conduct hydroxide from the cathode to the anode.

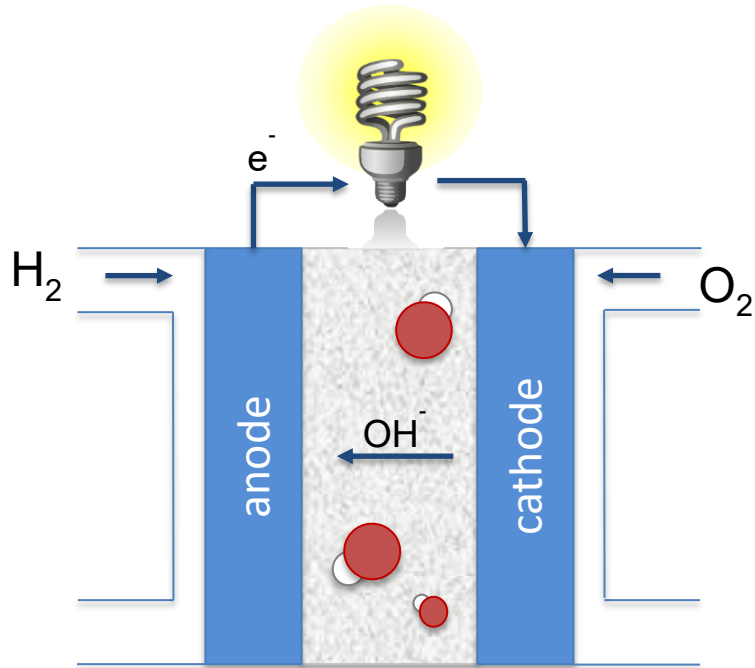
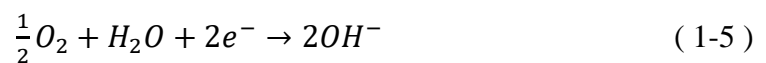


Figure 1.5: Schematic of a hydroxide exchange membrane fuel cell (HEMFC).

While the overall reaction of the fuel cell remains the same for an HEMFC (Equation 1-1), the HOR and ORR reactions occur through mechanisms involving a hydroxide ion. The HOR reaction can be written as:



The ORR reaction also changes to:



The theoretical cell voltage for an HEMFC is still 1.23 V, but the kinetics of the half-cell reactions change, as shown in Figure 1.6. While the overpotential for the

ORR remains approximately the same in alkaline conditions as in acidic conditions, the HOR overpotential is much higher. In fact, the activity of the HOR on Pt in alkaline electrolytes has been shown to be approximately two orders of magnitude lower than in acidic electrolytes.[9] Consequently, more Pt is needed on the anode of a HEMFC to achieve commercially viable power densities.

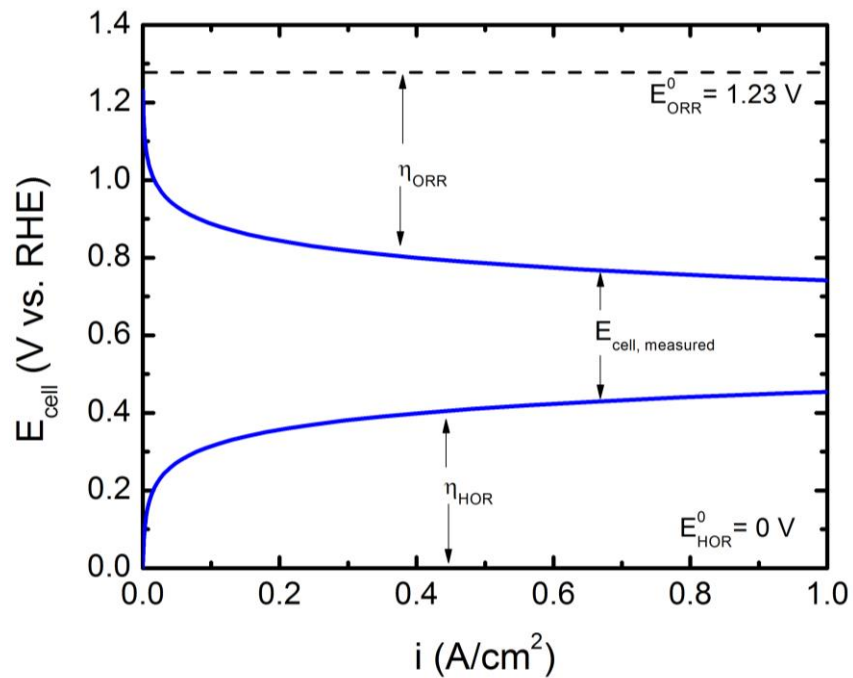
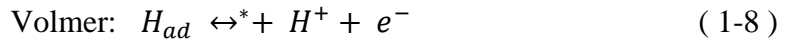
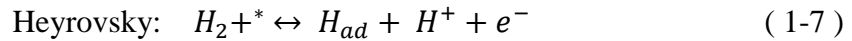


Figure 1.6: Estimation of kinetic losses for HOR and ORR in a HEMFC using kinetic parameters from literature.[9]

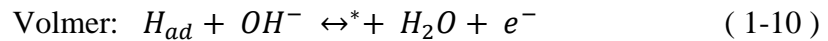
Therefore, while developing more effective ORR catalysts for HEMFCs remains a challenge, it is also important to find more suitable catalysts for the alkaline HOR.

### 1.3 The Hydrogen Oxidation Reaction (HOR) and Hydrogen Evolution Reaction (HER)

While the HOR is of interest for anodic electrocatalysts for fuel cells, the reverse reaction, the HER, is also an important reaction for electrolyzers. In the HOR, hydrogen gas is oxidized and split into protons and electrons. In the HER, protons and electrons are combined to produce hydrogen gas. This dissertation is mostly focused on the HOR, but the kinetics of the HOR and HER are inextricably linked. The HOR and HER are known to proceed through a combination of the two of the three following steps in acidic electrolytes[9,13]:



Here, \* represents an active catalyst adsorption site. In alkaline conditions, the Tafel reaction remains unchanged, but the Heyrovsky and Volmer reactions must be rewritten as the following:



Two mechanisms are possible from these elementary steps: Tafel-Volmer (Equations 1-6 and 1-10) and the Heyrovsky-Volmer (Equations 1-7 and 1-10). The Tafel-Volmer mechanism is the electrochemical equivalent of the Langmuir Hinshelwood reaction mechanism, while the Heyrovsky-Volmer reaction is the electrochemical analogue of the Eley-Rideal mechanism.

Since both mechanisms rely on the adsorption and desorption of hydrogen on the catalyst surface, the activity of a metal can be correlated to the hydrogen binding energy in a volcano relationship. A catalyst with a moderate hydrogen binding energy will be able to both bind hydrogen strongly enough to react and to allow the facile desorption of the adsorbate, leading to a higher activity. In electrochemistry, catalytic activity is usually quantitatively represented by exchange current densities, which are directly measurable currents at the reaction equilibrium potential. Figure 1.7 shows the volcano plot for the HOR/HER in acidic electrolytes. The hydrogen binding energies for each metal were calculated using density-functional theory (DFT) and compared to the corresponding exchange current densities found in literature.

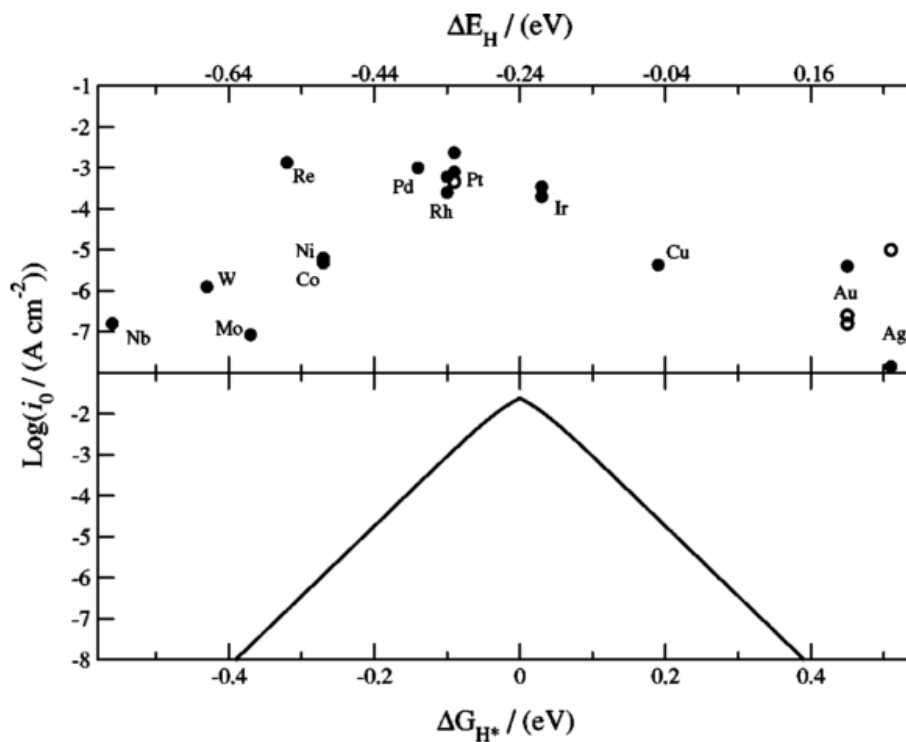


Figure 1.7: Volcano plot for HOR/HER on bulk monometallic surfaces in acidic electrolytes. Figure taken from reference [14].

The result, as expected, is that there is a range of metals with an intermediate binding energy that have the highest activities for HOR/HER. The Pt-group metals fall within the range of very active and stable metals for the acidic HOR/HER.

Pt has the highest activity for HOR/HER in alkaline conditions.[15] In order to develop new HOR/HER catalysts for HEMFCs, it is necessary to establish similar trends for the activity of monometallic surfaces in alkaline electrolytes. A similar volcano plot was developed for the HOR/HER in 0.1 M KOH, as shown in Figure 1.8.

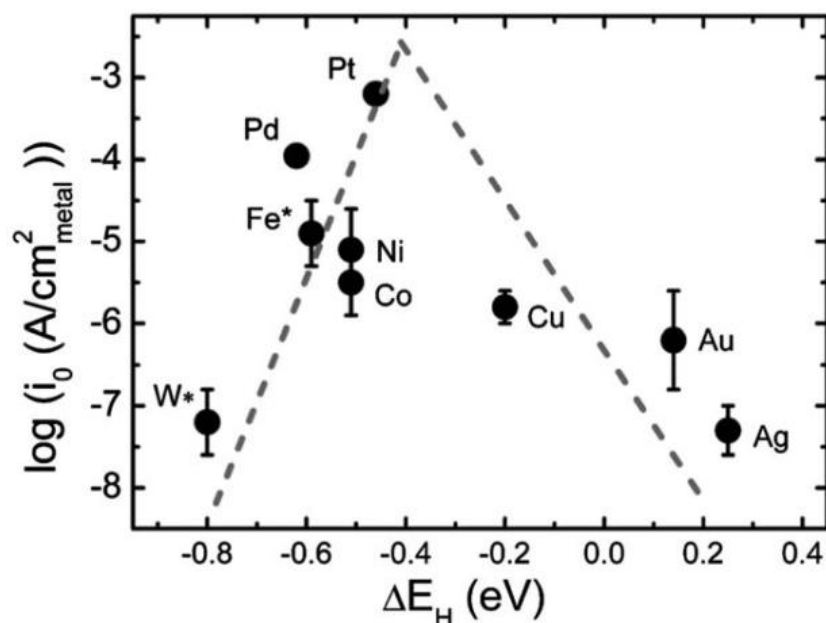


Figure 1.8: Volcano plot for HOR/HER on bulk monometallic surfaces in alkaline electrolytes. Figure taken from reference [16].

Figure 1.8 shows that the trend for the HOR/HER activity remains the same in alkaline conditions; that is, catalysts with an intermediate binding energy will have a higher exchange current density. As expected, Figure 1.8 also confirms that Pt is the most active metal in alkaline conditions.

#### 1.4 Research Strategy and Thesis Scope

Our research group uses both theoretical and experimental methods to rationally design new, novel catalysts for many systems. As illustrated in Figure 1.9, this process involves the combination of DFT calculations and experiments on bulk, idealized surfaces to establish catalytic trends, which are then used to predict more effective catalytic materials for use in commercially-viable systems. In the case of

electrocatalysis, the idealized surfaces generally used are disks of polycrystalline metals. However, supported nanoparticle catalysts are required in actual fuel cell devices.

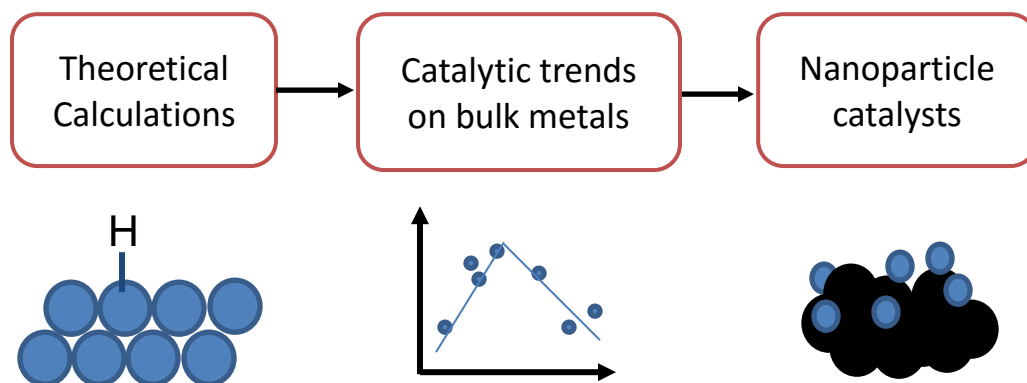


Figure 1.9: Research methodology to develop new, practical electrocatalysts.

This dissertation focuses on bridging the gap between bulk, monometallic electrodes and more practical supported electrocatalysts for anodic oxidation reactions in HEMFCs. In the next chapter, the methods used to synthesize and test various catalysts will be discussed. In addition, electrochemical theory will be outlined in order to bring a greater understanding of the results mentioned in the following chapters.

Chapter 3 first establishes catalytic trends for HOR/HER on supported monometallic and bimetallic electrocatalysts in an alkaline electrolyte. Both bulk disk electrodes and carbon supported metals are studied and related to the corresponding DFT-calculated hydrogen binding energies. These data will help extend the catalytic

trends established for idealized, polycrystalline surfaces to more practical electrocatalysts.

In Chapter 4, monolayer-equivalent loadings of Pt are deposited onto gold (Au) substrates to decrease the total amount of Pt needed for the alkaline HOR. Both disk electrodes and supported catalysts are tested to evaluate the catalysts for fuel cell applications. The catalysts are also further electrochemically characterized and compared to pure Pt and Au catalysts.

Since Au as a support can be too expensive, other support materials for Pt are examined. In Chapter 5, Pt is deposited on a variety of transition metal carbides and tested for alkaline HOR/HER to retain high HOR/HER activities while decreasing the overall cost of the catalyst.

In Chapter 6, the focus is the oxidation of fuels derived from biomass such as ethanol, ethylene glycol, and glucose. The Pt/Au disk and supported catalysts are also tested to decrease the amount of Pt needed for the oxidation of each fuel. Additionally, the Pt/Au surface is analyzed using in-situ FTIR to determine the mechanism of oxidation.

Finally, Chapter 7 concludes the dissertation with a summary of the main conclusions and possible future work to continue this research.

## **Chapter 2**

### **EXPERIMENTAL METHODS**

#### **2.1 Electrocatalyst Preparation**

In this dissertation, both commercially-obtained bulk metallic disk electrodes and supported catalysts were evaluated. Monometallic supported catalysts are compared to their respective disk electrodes in Chapter 3 to establish trends for the alkaline HOR. Since these materials were commercially obtained, replication of the results in this dissertation will be more straightforward for other groups. However, the correct preparation of these electrodes is imperative for acquiring accurate and consistent electrochemical data. The preparation is detailed in this chapter.

Some of the commercially-obtained electrocatalysts were also modified to enhance their activity. Specifically, the commercially obtained gold electrocatalysts were modified with Pt overlayers and tested for oxidation activities, as shown in Chapters 4 and 6. Transition metal carbides were also modified with Pt via incipient wetness impregnation and tested for HOR in Chapter 5.

##### **2.1.1 Disk Electrodes**

The Au, Ag, Co, Cu, Fe, Ni, Pd, Pt, and W disks (Pine Instruments) used for kinetic analyses were all 5 mm in diameter and inset into Teflon sheaths that attached on to the rotator shaft tightly. Quick change Au disks (Pine Instruments) were also used for XPS analysis because the metal puck can be removed from Teflon sheath after electrochemical testing. However, it is important that the interface between the

metal disk and sheath be as tight as possible when used in the rotating disk electrode (RDE) system, so the inset disks were used for most kinetic analyses.[17]

Before use, the disks were lightly polished to a mirror finish by hand using 0.05  $\mu\text{m}$  and a soft polishing pad (Beuhler) and dried with air. In the case that a disk surface was extensively scratched, 1  $\mu\text{m}$  alumina (Beuhler) was used before the 0.05  $\mu\text{m}$  alumina. Mechanical polishing machines were avoided, since the disk surface was found to warp over time with excess polishing. For most disks, a well-polished surface was found to result in a roughness factor of  $\sim 1.2$ .

### **2.1.2 Electrodes for Supported Electrocatalysts**

Supported catalysts are deposited on glassy carbon disk electrodes (5 mm diameter, Pine Instruments) through the use of a controlled amount of catalyst ink. The glassy carbon disk electrodes as prepared as explain in Section 2.1.1. As illustrated in Figure 2.1, the catalyst ink consisted of the supported catalyst dispersed in a solvent. A small amount of the ink is dropped onto the electrode surface and left to dry overnight while covered with a beaker. Ideally, the resulting electrode will have a homogeneous thin film of catalyst covering the entire glassy carbon surface (Figure 2.1c). However, it is very common for the catalyst film on the electrode to be non-uniformly distributed (Figure 2.1a,b). For RDE experiments, it is very important that the electrode surface be covered homogenously for accurate mass-transport contribution calculations, which is further explained in Chapter 2.3.5.

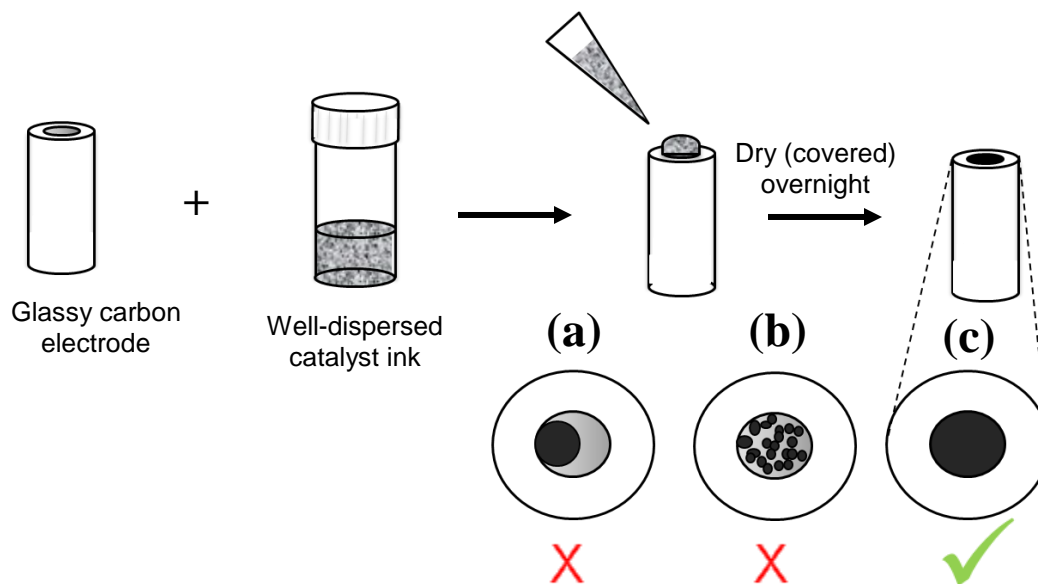


Figure 2.1: Visualization of supported electrode preparation. Examples of prepared electrodes are shown, exemplifying (a), (b) poorly prepared electrodes and (c) and ideally prepared electrode.

The quality of the electrode directly depends on the quality of the ink. However, due to the differing properties of each catalyst tested, the ink recipe generally varies and is optimized through trial and error. The first step in making an ink requires the calculation of the amount of catalyst to be measured using the following equation,

$$\left( \text{electrode metal loading} \left[ \frac{\mu\text{g}_{\text{metal}}}{\text{cm}^2_{\text{disk}}} \right] \right) \cdot (\text{electrode area} [\text{cm}^2_{\text{disk}}]) \cdot (\text{ink volume} [\text{mL}]) \cdot \left( \frac{1}{\text{drop volume} [\mu\text{L}]} \right) \cdot \left( \frac{1}{\text{catalyst metal weight fraction}} \right) = \text{amount of catalyst needed for ink} [\text{mg}] \quad (2-1)$$

where the electrode metal loading is the mass of the active metal per area of the electrode, the electrode area is the geometric area of the glassy carbon electrode (in all cases for this dissertation  $\text{cm}^2_{\text{disk}} = 0.196$ ), the ink volume is the total volume of ink desired, the drop volume is the amount of ink to be placed on the glassy carbon electrode to achieve the desired electrode metal loading, and the catalyst metal weight fraction is the fraction of active metal in the supported catalyst.

In order to determine a proper electrode metal loading, both the metal being tested and the resulting electrode film thickness must be considered. If the metal being tested has a high activity toward the reaction of interest, the electrode metal loading does not need to be more than  $10 \mu\text{g}_{\text{metal}}/\text{cm}^2_{\text{disk}}$ . In fact, having too much of an active metal on the electrode surface may cause difficulties in extracting accurate kinetic data from the HOR polarization curve, as occurs for Pt catalysts in acidic electrolytes. This happens because the HOR branch of the polarization curve reaches the Nerstian diffusion overpotential and cannot be corrected for mass transport contributions, as outlined in Section 2.3.6 .[9]

On the other hand, if the metal is not very active, a higher loading may be considered. However, increasing the metal loading will also increase the support loading. While the supports used here are generally catalytically inactive, they do contribute to the electrode film thickness. A film that is too thick can skew electrochemical measurements due to added mass transport resistances.[18] Therefore, all electrodes were prepared with the aim of keeping the carbon loading beneath  $50 \mu\text{g}_{\text{carbon}}/\text{cm}^2_{\text{disk}}$ . [19]

The total ink volume needed is not fixed, but the type of solvent used for the ink plays a large role in the quality of the final electrode. A good ink will allow the

catalyst to be homogeneously dispersed in the solvent after being sonicated and will remain dispersed over the period of a day. Any ink that crashes out or clumps within a few hours will not result in a good electrode, since the catalyst will not be deposited on the GC surface in a homogeneous manner. A solvent of 100% deionized (DI) H<sub>2</sub>O is preferred because it evaporates slowly after being dropped on the glassy carbon electrode. If DI H<sub>2</sub>O alone does not disperse the catalyst sufficiently, another solvent may be mixed with the water.

The required drop size depends on the composition of the solvent, specifically the surface tension of the mixture. For inks of 100% DI H<sub>2</sub>O, a drop size of 20  $\mu$ L is appropriate. If a solvent such as isopropanol is used, the surface tension of the ink will be lower. Therefore, drops of higher volumes will not stay on the GC surface. As more isopropanol is used, the drop size needs to decrease to about 10-15  $\mu$ L. The drop size should be tailored to suit the ink. No ink should spread onto the Teflon sheath when being deposited. If this occurs, the drop size should be lowered or the ink composition adjusted.

No inks made for the purpose of this dissertation contained Nafion. Nafion is commonly used as a binder in order to help the catalyst stick to the glassy carbon surface. However, it is currently unknown how Nafion, a proton conducting membrane, affects electrochemical kinetics in alkaline media. All inks made here exhibited acceptable adherence to the glassy carbon electrode, so no Nafion was needed.

Before being dropcast onto the glassy carbon electrode, the ink must also be ultrasonicated to fully disperse the catalyst. After the initial preparation of an ink, it was sonicated for 30 minutes. For all following uses of the ink, it was only sonicated

for ~5 minutes or until the ink showed full dispersion. This was tested by holding the ink up to a light. If no large particles are seen, then the ink is well dispersed.

It is worth noting that the above recommendations are heuristics. Even if a good ink recipe has been found, the ink quality can vary from batch to batch. Successful supported electrode preparation is a trial-and-error technique.

### **2.1.3 Incipient Wetness Impregnation**

The aim of Chapter 5 is to compare Pt-modified transition metal carbides to Pt-modified transition metal carbide foils. The foils were synthesized in ultra-high vacuum using physical vapor deposition, which is not a viable technique for the modification of powders with platinum. Therefore, incipient wetness impregnation was used to deposit Pt onto commercially-obtained transition metal carbides. The transition metal carbide powders used were TiC, TaC, NbC, VC, and ZrC (Alfa Aesar).

In a typical impregnation synthesis, a metal precursor salt is dissolved in water and dropped onto the support material. The amount of solution added to the support is equal to the pore volume of the support. The precursor is driven into the pores of the support by capillary forces. The water and salt are then removed by drying the catalyst, leaving the metal behind on the support.

Another form of incipient wetness is known as slurry synthesis, which is appropriate for synthesizing catalysts with high metal loadings on supports with low surface area, such as the transition metal carbide powders. In this case, the volume of precursor solution is larger than the support pore volume. This procedure was used to synthesize 1% Pt on commercially-obtained TiC, TaC, NbC, VC, and ZrC (Alfa-Aesar).  $\text{Pt}(\text{NH}_3)_4(\text{NO}_3)_2$  (Alfa Aesar) was used as a Pt precursor. 0.0099 g of the precursor were dissolved in 5 mL of DI  $\text{H}_2\text{O}$  and added to 0.495 g of the support in a

vial. The solution was then stirred for 12 hours at room temperature to ensure the adsorption of the precursor onto the support. The solution was then placed in an oil bath and heated to ~330 K for another 12 hours to slowly evaporate the water. The vial was then placed in a furnace and heated to 373 K at 0.4 K/min and dried for 10 hours. After the catalyst was fully dried, it was ground to a fine powder with a glass rod. The solid was then transferred to a quartz tube furnace to be reduced under H<sub>2</sub> (20 sccm) at room temperature for 30 minutes. The temperature was then increased at 1 K/min to 563 K and held for 4 hours. The furnace was allowed to cool to room temperature and passivated in 99% N<sub>2</sub> and 1% O<sub>2</sub> (100 sccm) for 1 hour.

## **2.2 Characterization Techniques**

### **2.2.1 Transmission Electron Microscopy (TEM)**

Electron microscopy is a useful technique that allows the imaging of samples on the nanometer scale. The advantage of TEM in particular is that it can image supported electrocatalysts with great precision, as is done in Chapter 4 to determine the average particle diameter. TEM works by producing a beam of electrons from a filament, which is then focused onto the sample using electromagnetic “lenses.” The interactions with the sample cause the electrons to scatter. The resulting diffraction beam is refocused into a Fourier transform image and displayed on a fluorescent viewing screen.

One limitation of TEM is that the sample must be very thin to allow the passage of the electron beam. Therefore, this technique is only applicable to the supported catalysts in this study. Samples were prepared by dropping the catalyst ink onto a 200 mesh holey carbon grid, which was left to dry overnight. The samples

were analyzed with a JEOL 2010f TEM with a Schottky field-emission gun operated at 200 keV.

### 2.2.2 X-ray Photoelectron Spectroscopy (XPS)

XPS is a surface-sensitive technique that can give information on the elemental make-up and chemical or electronic state of a material. Since XPS requires ultra-high vacuum environments to operate, it was limited to the analysis of disk electrodes in this dissertation.

Surface analysis via XPS is performed by irradiating the surface with monoenergetic X-rays provided by a Mg or Al source and measuring the energy of the produced photoelectrons (Figure 2.2). The photons used to irradiate the surface can only penetrate 1-10  $\mu\text{m}$  into the sample, which causes the technique to be inherently surface-sensitive.

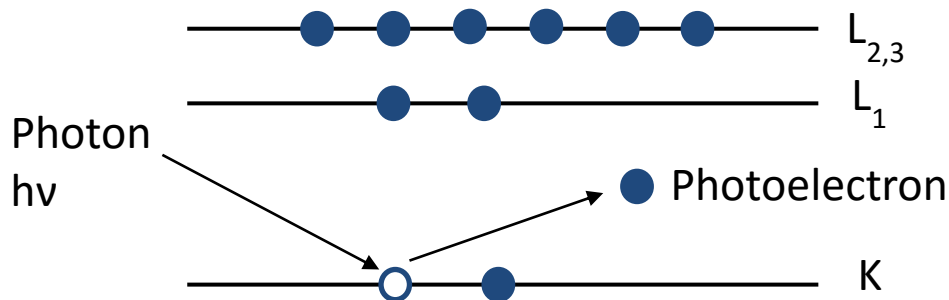


Figure 2.2: Illustration of XPS photoelectron emission process.

The emitted photoelectrons have kinetic energies ( $KE$ ) given by:

$$KE = h\nu - BE - \phi_s \quad (2-2)$$

where  $h\nu$  is the energy of the incident photon,  $BE$  is the binding energy of the electron of the atomic orbital from which the photoelectron is ejected, and  $\phi_s$  is the spectrometer work function. In this dissertation, the incident X-ray used was Al  $K\alpha$  (1486.7 eV). XPS can identify elements in the sample because each element has its own unique sets of binding energies. The binding energies can shift depending on the environment in which the element is contained, and therefore these shifts can be used to identify the chemical state of the sample being analyzed.

### **2.2.3 Fourier Transform Infrared Spectroscopy (FTIR)**

In general, infrared (IR) spectroscopy takes advantage of the fact that molecules will adsorb different frequencies of light depending on their structure. In order for a certain vibrational mode of a molecule to absorb IR radiation, it must undergo a change in dipole. When the frequency of light shone onto or through the sample is the same as the vibrational frequency of a bond, the light is absorbed. Therefore, measurement of the transmitted light will show how much light was absorbed at each wavelength. The resulting spectrum allows for the analysis of chemical species present through the presence of absorption peaks at different wavelengths. The most straight-forward way of doing this is to use a monochromator and collect transmittance data for each wavelength of light. FTIR instead uses a light source emitting a continuum of wavelengths of light and measures how much of that light is absorbed by the sample. A source containing different combination of wavelengths is then used and the process is repeated. The absorption at each wavelength can then be obtained after analysis to give the IR absorption spectra of the sample.

In this dissertation, FTIR is used in tandem with a specialized electrochemical cell to obtain IR spectra at different potentials in Chapter 6. FTIR spectroscopy measurements were conducted with a Nicolet Nexus 870 spectrometer. The spectrometer is equipped with a liquid nitrogen-cooled MCT detector. The electrochemical cell consists of a ZnSe hemisphere window and an electrochemical cell with three electrodes (working electrode, Ag/AgCl as reference electrode, and Pt coil as counter electrode). The IR chamber was purged with N<sub>2</sub> for approximately 3 hours to remove any possible signal interference from CO<sub>2</sub> and water moisture. The absorbance spectra were calculated as the ratio  $\log(S_s/S_R)$ , where S<sub>s</sub> is the absorbing species and S<sub>R</sub> is the corresponding reference. The first spectrum was taken as the reference and all the other spectra were taken at different applied potentials at a scan rate of 1 mV/s. All potentials were converted to the RHE scale using the same calibration as the oxidation CVs. Positive FTIR bands correspond to the formation of products while negative bands represent the consumption of reactants.

## **2.3 Electrochemical Techniques**

### **2.3.1 Three cell set up**

This dissertation focuses on electrochemical analyses, which were all completed in a traditional three cell configuration (Figure 2.3). The glass electrochemical cell (Pine Instruments) is designed to contain an electrolyte, a reference electrode, a gas sparger, a counter electrode, and the working electrode.

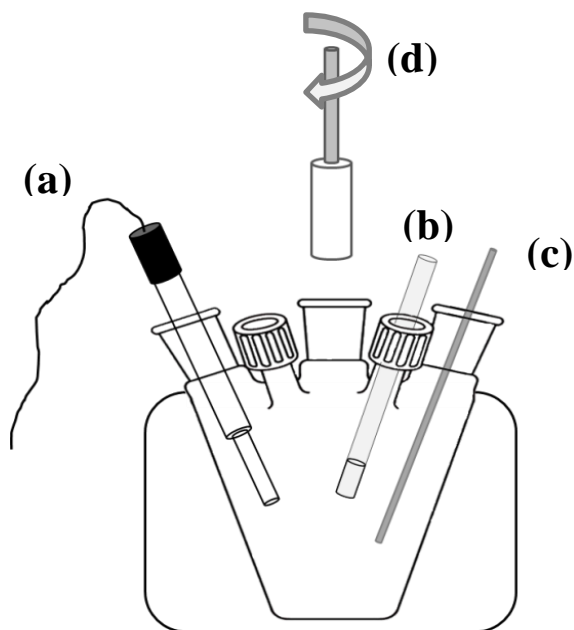


Figure 2.3: Three cell configuration including (a) reference electrode, (b) gas sparger, (c) Pt counter electrode, and (d) working electrode.

The working electrode contains the electrocatalytically active surface under study. Current flows between the working and counter electrode, which for the purpose of this dissertation is a coiled Pt wire (Pine Instruments), and the potential of the working electrode is measured against the reference electrode. Both a saturated double-junction Ag/AgCl (0.197 V from NHE) and a reversible hydrogen electrode (RHE) are used in this dissertation. A Versastat 4F potentiostat (Princeton Applied Research) was used to control the potential between the working and reference electrodes. The purpose of the counter electrode is to provide current for the reaction on the working electrode.

### 2.3.2 Voltammetric Techniques

Using a potentiostat, there are several ways to control the potential of the working electrode to perform different experiments. The techniques relevant to this dissertation are described below.

#### 2.3.2.1 Cyclic Voltammetry (CV) and Linear Sweep Voltammetry (LSV)

CV is a widely used technique to measure redox states on the surface of the working electrode. In essence, the potential of the working electrode is swept between two potentials at a constant rate, as illustrated in Figure 2.4.

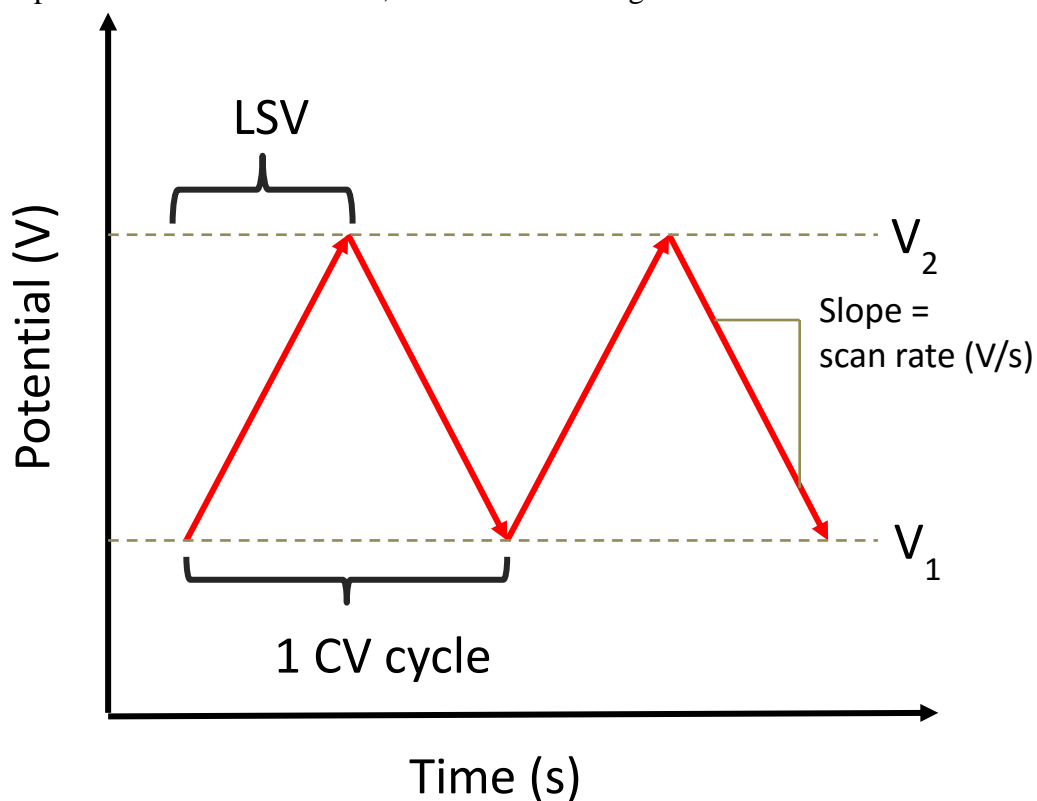


Figure 2.4: Illustration of potential control in CV and LSV.

The upper and lower potential limits of the CV scans are denoted as  $V_1$  and  $V_2$  in Figure 2.4. These are generally chosen based on the properties of the system and what redox information is of interest. The current is obtained at each data point and plotted versus the corresponding potential.

LSV is essentially one sweep of a CV, as shown in Figure 2.4. It is used in this dissertation to gather kinetic data for the hydrogen reaction studies in Chapters 3, 4, and 5.

CV is performed in a static solution and the working electrode is not rotated. Therefore the mass-transfer to the electrode surface is sluggish. In this way CV is inherently a non-steady state technique and varies with time. In order to determine the steady-state properties of a system, chronoamperometry must be used.

#### **2.3.2.2 Chronoamperometry (CA)**

Since CV is not a steady-state technique, CA is used to analyze the behavior of the working electrode over time at one potential, as illustrated in Figure 2.5.

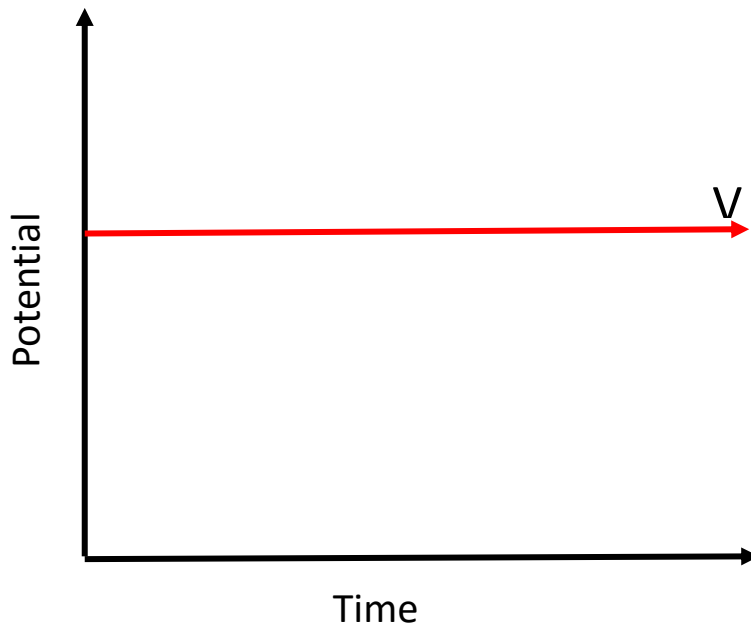


Figure 2.5: Illustration of potential control in CA.

The potential used for CA,  $V$ , is chosen based on the redox reaction of interest found in the CV. At each data point, the current is measured and plotted as a function of time.

### 2.3.2.3 Electrochemical Impedance Spectroscopy (EIS)

For both the Butler-Volmer and Tafel analyses described in Section 2.3.6, the measured current must be  $iR$ -corrected to determine the kinetic current. If this is not done, then kinetic parameters extracted from the data may not be accurate. The resistance of the electrochemical system is found using EIS.

In short, EIS is performed by applying an AC potential to the system as illustrated in Figure 2.6.

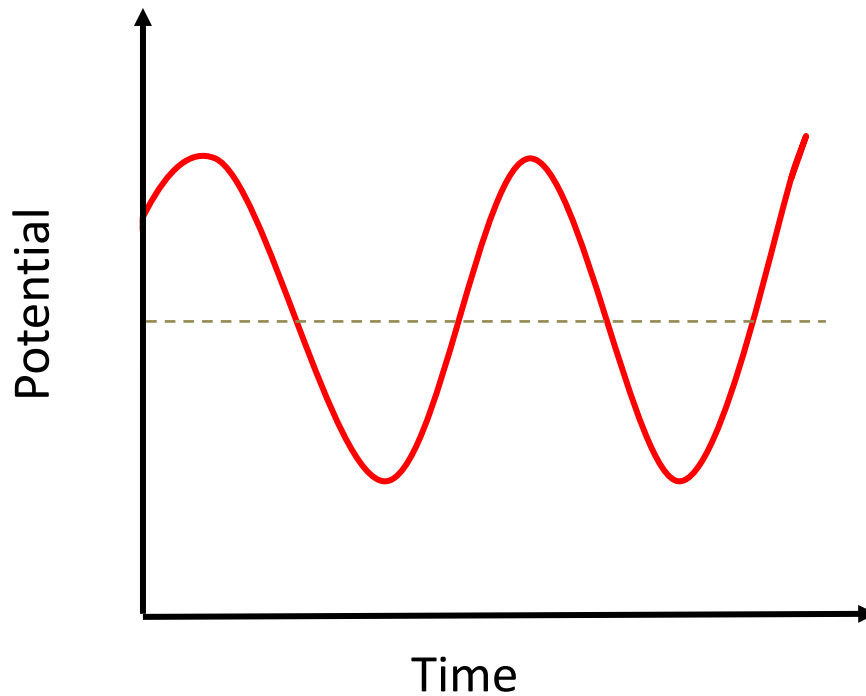


Figure 2.6: Illustration of the potential signal in EIS.

If an AC potential is applied to the electrochemical cell, then an AC current response will be measured and analyzed as a Fourier series. However, electrochemical systems are not necessarily linear. Therefore a small potential perturbation is applied in order to obtain a pseudo-linear current response that has the same frequency as the potential perturbation. By analyzing the relationship of the measured current with the applied potential perturbation, the cell resistance can be measured.

The uncompensated cell resistance was measured directly after electrochemical measurements using the Versastat 4F. The ac impedance spectra were taken from 32 to 0.1 kHz using a voltage perturbation of 10 mV. The cell resistance used to calculate the  $iR$ -corrected potential was taken as the real part of the resistance at 1 kHz.

### **2.3.3 Galvanic Displacement of a Cu Monolayer with Pt**

The synthesis of Pt/Au by the galvanic displacement of underpotential deposited Cu is established in other studies.[20,21] The same protocol was used for depositing Pt on both disk Au electrodes and thin film Au/C electrodes. The Au substrate was placed in a Ar-purged solution of 0.05 M CuSO<sub>4</sub> and 0.05 M H<sub>2</sub>SO<sub>4</sub>. A double junction Ag/AgCl electrode and a coiled Pt wire were used as a reference electrode and counter electrode, respectively. The potential was cycled from 0.8 V to 0.13 V vs. Ag/AgCl at 20 mV/s to deposit a monolayer of Cu on the gold. The electrode was immediately rinsed in deaerated deionized water and transferred to a solution of deaerated 0.001 M K<sub>2</sub>PtCl<sub>4</sub> in 0.05 M H<sub>2</sub>SO<sub>4</sub> for at least two minutes to ensure the complete galvanic displacement of Cu by Pt. The Pt/Au samples were rinsed and tested immediately after synthesis.

### **2.3.4 Determining Electrochemically Active Surface Area**

#### **2.3.4.1 CV Peaks**

This method works for any surface that has well-defined redox peaks with an associated charge density. In this dissertation, this method is used for the surface area determination of Au, Ag, Cu, Ir, Pt, Pd and Rh catalysts. An example CV for Pt is shown in Figure 2.7.

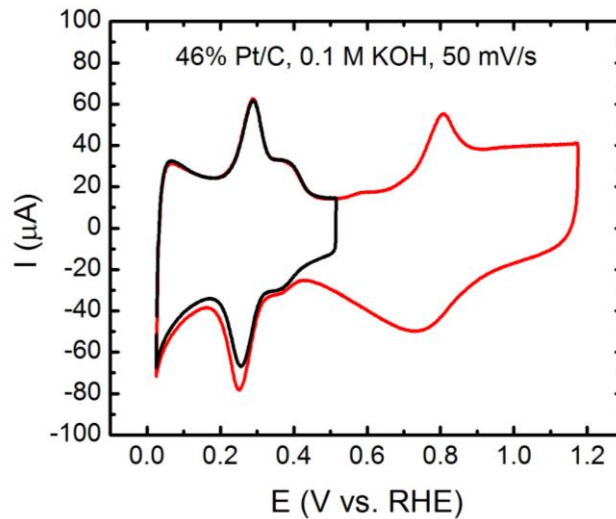


Figure 2.7: Sample CVs of 46% Pt/C in 0.1 M KOH using different upper potential limits (red and black curves).

In this example,  $V_1$  and  $V_2$  are 0.05 V and 1.2 V vs. RHE and the scan rate is 50 mV/s. The peaks seen in the CV correspond to redox reactions occurring on the catalyst surface. In this method, the charge corresponding to one of the redox reactions observed in the CV is compared to a charge density found in literature. This charge is found by integrating the CV peak corresponding to that redox reaction and using the following relationship:

$$\frac{\text{Peak area}_{CV} [\mu\text{A}\cdot\text{V}]}{\text{Scan rate} \left[\frac{\text{V}}{\text{s}}\right]} = \text{Charge} [\mu\text{C}] \quad (2-3)$$

In all cases, the double layer current is used as the baseline. In the example CV in Figure 2.7, the double layer current occurs at approximately 0.5 V vs. RHE, but will vary depending on the catalyst. The charge obtained from the CV and a known charge density are used to calculate the active area of metal on the surface:

$$\frac{\text{Charge } [\mu\text{C}]}{\text{Charge density } \left[\frac{\mu\text{C}}{\text{cm}_{\text{metal}}^2}\right]} = \text{Surface area } [\text{cm}_{\text{metal}}^2] \quad (2-4)$$

The sample should be cycled about 10-20 times to ensure that the CV does not change between cycles before the peak of interest is integrated. The advantage of this technique is that it can be done on a variety of metallic surfaces very quickly before reaction data is obtained. However, compared to other surface area determination techniques, this method is not very accurate.

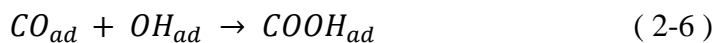
#### 2.3.4.2 CO Stripping

A common, accurate method of determining the surface area of Pt and other Pt-group metals is by calculating the charge associated with the oxidation of one monolayer of CO on the catalyst surface.[22] This can be done in acidic and alkaline media. In this dissertation, CO stripping is used to calculate the surface area of the Pt/Au catalysts in Chapters 4 and 6 for the kinetic analyses of alkaline electrochemical reactions. Au samples were also tested to investigate the CO oxidation activity, though no surface area analyses can be performed with this method. All CO stripping was done in alkaline media to be consistent with the media in which the reactions of interest are taking place.

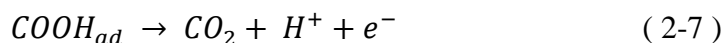
It is generally accepted that the oxidation of CO in alkaline media on Pt occurs via a Langmuir-Hinshwood mechanism in which adsorbed CO reacts with a oxide species.[23] In alkaline media, the oxide species is likely formed from OH<sup>-</sup> ions in solution via the following reaction:



The rate-determining step for this mechanism on most surfaces is the reaction of adsorbed CO with adsorbed OH:



Carbon dioxide is then formed through an additional charge transfer step:



In alkaline media, CO<sub>2</sub> can also be converted to carbonate, which is considered the exhaustive oxidation product.

In alkaline media, CO oxidation on Pt surfaces is very structure-sensitive due to the blockage of active sites by carbonate.[24] This results in the appearance of several oxidation peaks in the CO stripping voltammogram, whereas in acid only one peak is noticeable. Nevertheless, the integration of these peaks corresponds to a charge density of 420 μC/cm<sup>2</sup><sub>Pt</sub>.

In order to obtain the CO stripping voltammogram, the Au, Pt or Pt/Au sample was placed in a solution of 0.1 M KOH. As the sample was held at 0.1 V vs. RHE, a dilute mixture of CO gas was bubbled through the solution for ten minutes to adsorb one monolayer of CO, followed by a pure Ar stream for an additional ten minutes to purge the solution of non-adsorbed CO. The potential was then cycled from ~0 V to ~1.6 V vs. RHE at 20 mV/s for Au samples or ~0 V to ~1.2 V for Pt and Pt/Au samples to oxidize, or strip, the pre-adsorbed monolayer of CO. The background CVs were obtained directly after the CO stripping at 20 mV/s. The total charge associated

with CO stripping was calculated using Equation 2-3 using the background curve as a baseline. The surface area is then found using Equation 2-4.

### 2.3.4.3 Cu Stripping

Similar to the CO stripping method, the surface area of Pt surfaces can also be determined from the stripping of one monolayer of Cu. The drawback of this technique is that it only works for metals with a similar atomic radii as Cu, such as Pt or Ru. However, whereas in CO stripping the monolayer of CO is preadsorbed before oxidation, the monolayer of Cu is underpotentially deposited in a solution of  $\text{Cu}^{2+}$  ions. Underpotential deposition (UPD) occurs because, at certain potentials, the interactions between the Cu and the substrate are stronger than the bulk deposition Cu-Cu interactions, which only allows the deposition of one layer of Cu. This is shown in an example CV of Pt in a solution containing  $\text{Cu}^{2+}$  ions (Figure 2.8). Between 0 and 0.3 V vs. RHE, bulk Cu deposition and stripping are observed. However, in the anodic scan between 0.25 V and 0.8 V vs. RHE, distinct peaks are observed that correspond to the deposition of one monolayer of Cu ions on different Pt crystalline facets following the reaction:



The charge density for this reaction on a polycrystalline Pt surface is  $420 \mu\text{C}/\text{cm}^2_{\text{Pt}}$ .

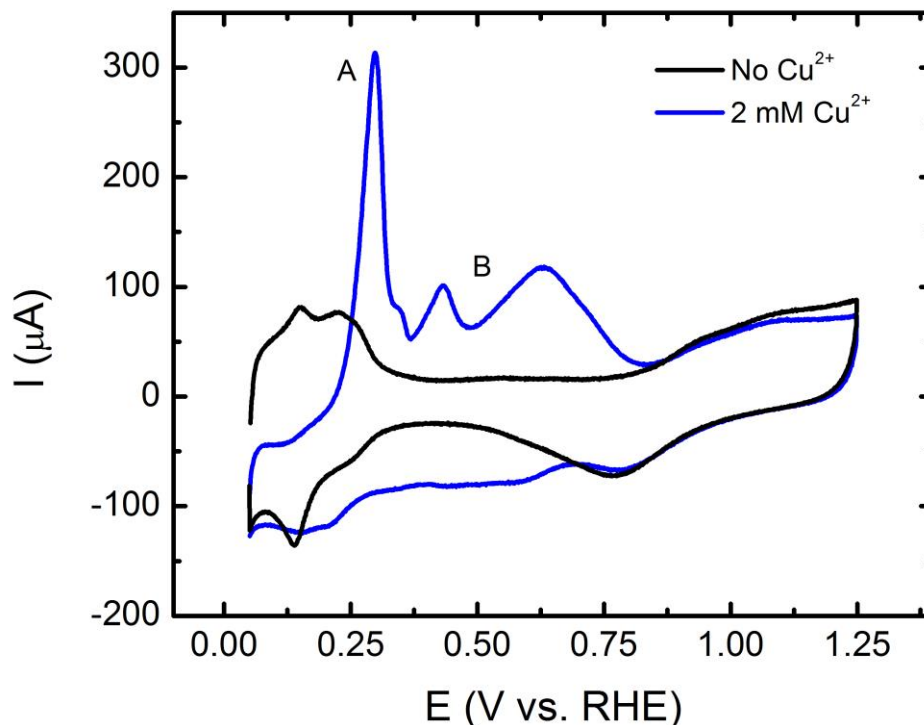


Figure 2.8: CVs taken at 50 mV/s of 46% Pt/C in 0.5 M H<sub>2</sub>SO<sub>4</sub> with (blue line) and without (black line) 2 mM of CuSO<sub>4</sub>. In the solution containing Cu<sup>2+</sup> ions, both (A) bulk Cu and (B) UPD Cu deposition/stripping are present.

If a lower potential limit is chosen where bulk Cu deposition does not occur, the Cu UPD region can be successfully isolated for the determination of the Pt surface area. A lower potential limit of 0.25 V vs. RHE was used for all Pt samples in this dissertation. Since CV is inherently a non-steady state technique, a full monolayer of UPD Cu will not be formed at this potential. Therefore, LSV was used after an equilibration at 0.25 V vs. RHE for 60 seconds to ensure the formation of a full Cu monolayer.[25] In addition, the background current due to the Pt catalyst itself must be subtracted from the Cu stripping curve to obtain an accurate Cu UPD current.

The following procedure was implemented for all Cu stripping experiments: first, the Pt-containing electrode was placed in a three-electrode cell configuration containing 0.5 M H<sub>2</sub>SO<sub>4</sub> and cycled 20-25 times to clean the Pt surface. The potential was then held at 0.25 V vs. RHE for 60 seconds. Using LSV, the potential was immediately scanned from 0.25 V to 0.8 V vs. RHE after equilibration to obtain the background current. The electrode was then transferred to a separate cell containing 0.5 M H<sub>2</sub>SO<sub>4</sub> and 2 mM CuSO<sub>4</sub>. The same equilibration and LSV was then performed in the presence of Cu<sup>2+</sup> ions to obtain the Cu stripping curve. To find the total charge transferred in the Cu stripping process, the background current was subtracted from the Cu stripping curve. Equations 2-3 and 2-4 are then used to calculate the surface area, as described in Chapter 2.3.4.1 using the charge density of 420 μC/cm<sup>2</sup><sub>Pt</sub>.

### **2.3.5 Rotating Disk Electrode (RDE) Configuration**

All of the electrochemical methods mentioned thus far are conducted in a static electrolyte, which depends on the diffusion of reactive species to the electrode surface. However, if the electrode is well-stirred, then the diffusive contribution of the reactive species to the surface becomes negligible and allows the measurement of true kinetic current. The hydrodynamic equations for the RDE configuration have been solved for steady state and therefore make the ideal system for analyzing electrochemical kinetics. In the RDE system, the disk electrodes explained in Section 2.1.1 are attached to a shaft that is rotated at a certain rotation frequency. The electrical connection is completed with brush contacts to minimize noise.

The solution of the convective-diffusion equation for the RDE set up is shown in Figure 2.9.

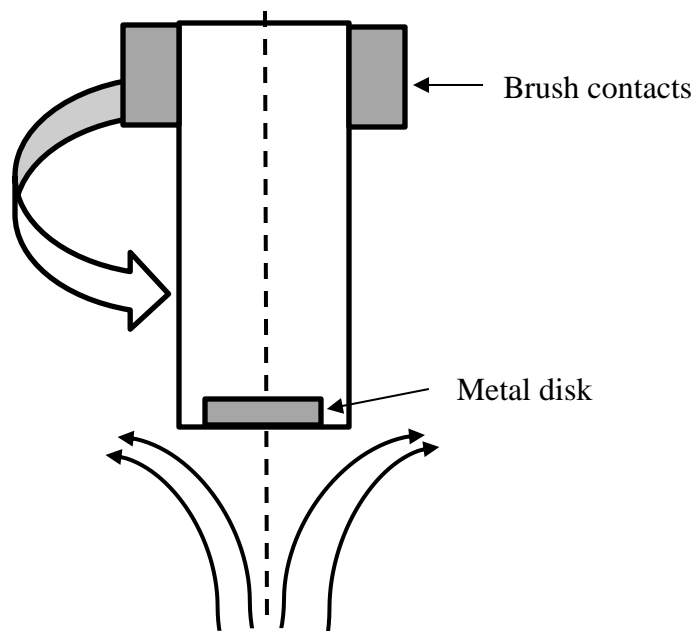


Figure 2.9: RDE set up including illustration of electrolyte flow toward the disk electrode surface.

By rotating the electrode, laminar flow is induced at the electrode surface. At a constant rotation rate and a steady-state velocity profile, the kinetic current of the reaction being measured will plateau at the mass-transport limiting current density ( $i_{l,c}$ ), which is given in the Levich equation as [17]:

$$i_{l,c} = 0.62nFAD_0^{2/3}\omega^{1/2}\nu^{-1/6}C_0^* \quad (2-9)$$

where  $n$  is the number of electrons transferred in the reaction,  $F$  is Faraday's constant (96,485 C/mol),  $A$  is the geometric area of the active disk surface,  $D_0$  is the diffusion

coefficient of the reactant,  $\omega$  is the angular velocity,  $\nu$  is the viscosity of the solution, and  $C_O^*$  is the equilibrium concentration of the reactant in solution. In all cases in this dissertation where this analysis is used, the reactant of interest is hydrogen gas.

In a system where mass-transport effects are significant, such as the alkaline HOR, the measured current ( $i$ ) must be corrected in order to obtain the true kinetic current ( $i_k$ ):

$$\frac{1}{i} = \frac{1}{i_k} + \frac{1}{i_{l,c}} \quad (2-10)$$

Substituting Equation 2-10 into the Levich equation, the Koutecky-Levich equation is obtained [17]:

$$\frac{1}{i} = \frac{1}{i_k} + \frac{1}{0.62nFAD_O^{2/3}\omega^{1/2}\nu^{-1/6}C_O^*} \quad (2-11)$$

In the settings in which HOR/HER kinetics are measured,  $n$ ,  $F$ ,  $A$ ,  $D_O$ ,  $\nu$ , and  $C_O^*$  will be constant. Therefore, the mass-transport limiting current density only depends on the rotation rate. The relationship between  $1/i_k$  and  $\omega^{-1/2}$  is linear and is called a Koutecky-Levich plot, as shown in Figure 2.10.

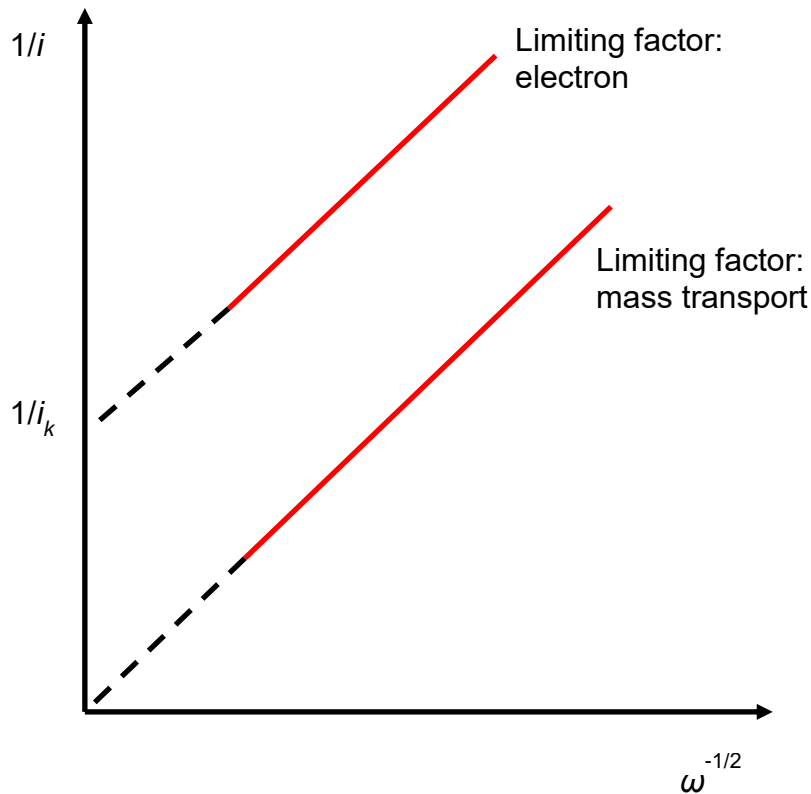


Figure 2.10: Example of a Koutecky-Levich plot at potentials where electron transport is limiting and where mass-transport is limiting ( $i_{l,c}$ ).

The slope of all lines in the Koutecky-Levich plot is  $(0.62nFAD_0^{2/3}v^{-1/6}C_0^*)^{-1}$ .

Therefore, by finding the slope of the Koutecky-Levich plot in potential regions where  $i_{l,c}$  holds,  $i_k$  can be calculated for all other potential regions of interest. This is especially important for calculating kinetic parameters from raw data, as is done for all HOR/HER analyses in this dissertation.

### 2.3.6 HER/HOR Kinetic Analyses

It is important to note that the HOR consumes hydrogen while the HER produces it. This becomes important when reconciling mass-transport effects in the measured polarization curves.

Regardless of the HOR/HER mechanism, the overall current-potential relationship of the reaction can be modeled using the Butler-Volmer equation:

$$i_k = i_0 [e^{(\alpha F/RT)\eta} - e^{-(1-\alpha)F/RT}\eta] \quad (2-12)$$

where  $i_0$  is the exchange current density,  $\alpha$  is the charge transfer coefficient,  $F$  is Faraday's constant (96,485 A s/mol),  $R$  is the universal gas constant (8.314 J/mol K),  $T$  is the temperature (K), and  $\eta$  is the overpotential. Overpotential is defined as the difference between the equilibrium potential and the potential being observed. For HOR/HER, the equilibrium potential is 0 V vs. RHE. The exchange current density,  $i_0$ , can be thought of as the background current occurring at that potential, when the HOR and HER are in equilibrium. It is the kinetic parameter that is used to compare the activity of different catalysts; a higher  $i_0$  value or less negative  $\log(i_0)$  value means a catalyst is more active. The physical meaning of the transfer coefficient  $\alpha$  can be considered as the fraction of interfacial potential associated with lowering the energy barrier of the redox reaction of interest or the symmetry of the reaction energy barrier.[17]

For catalysts that are active enough to reach the mass-transport limited current density, a polarization curve is fit to the Butler-Volmer equation. Using LSV, polarization curves are obtained for an electrode at 400, 900, 1600, and 2500 rpm by sweeping the potential from ~ 1.0 V (RHE) to ~ -1.5 V (RHE) at 10 mV/s in a

hydrogen-saturated solution. An example of this is shown for the Pt disk in Figure 2.11. All polarization curves are then corrected using the cell resistance found through EIS (Section 2.3.2.3).

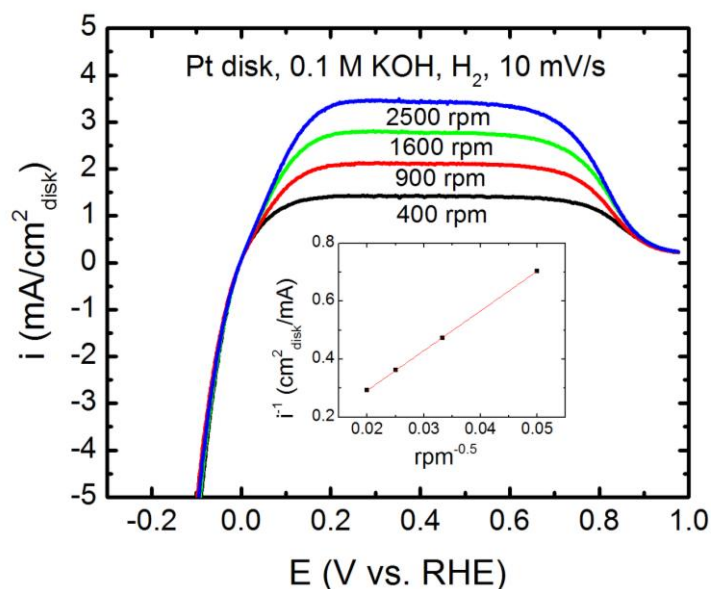


Figure 2.11:  $iR$ -corrected polarization curves of the Pt disk taken at different rotation rates at 10 mV/s. The inset shows the obtained Koutecky-Levich plot.

The polarization curves obtained at 1600 rpm were chosen for kinetic analyses. This rotation speed was chosen to ensure that bubbles are removed from the surface quickly in the HER branch. These bubbles can interfere with the polarization curve and skew the calculated kinetic parameters. The polarization curve at 2500 rpm was not chosen since this faster rotation rate may increase the chances of the supported catalysts falling off of the electrode surface. Before fitting to the Butler-Volmer equation, the polarization curves were corrected for mass-transport contributions using the Koutecky-Levich equation (inset of Figure 2.11). Since the HOR reaction is

dependent on diffusion of hydrogen gas to the surface of the electrode and the diffusivity of hydrogen in the electrolyte is low, the HOR branch must be corrected using the Koutecky-Levich equation to obtain  $i_k$ . However, since water is the reactant for the HER and is readily available in solution, the HER branch of the polarization curve did not attain the mass-transport limited regime. Therefore,  $i_k$  values were calculated using the Koutecky-Levich equation for the HOR branch only. For the HER branch, the  $iR$ -corrected current was used as is. Figure 2.12 shows the polarization curve for the Pt disk before and after mass-transport correction.

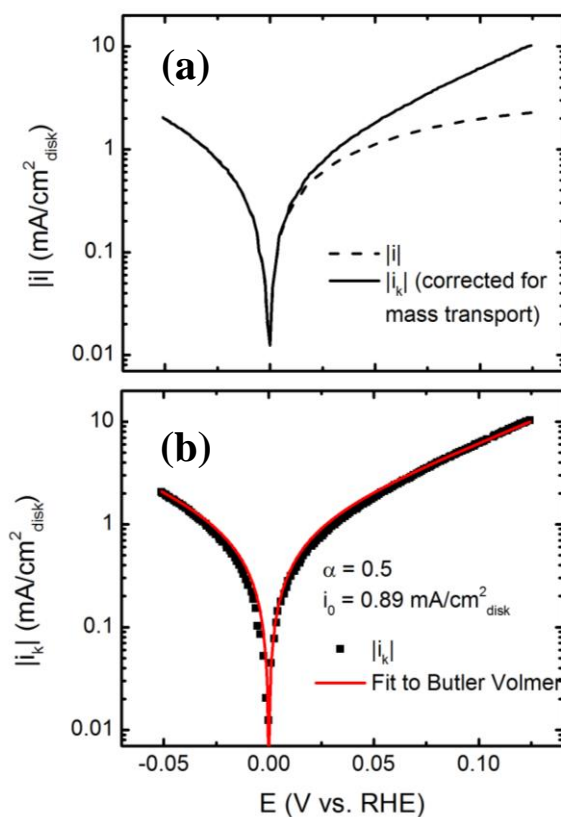


Figure 2.12: (a) Pt disk polarization curve at 1600 rpm in 0.1 M KOH for HOR/HER before and after mass-transport correction in the HOR branch. (b) Fit of the Butler-Volmer equation to the polarization curve data.

Before being fit to the Butler-Volmer equation, the polarization curve was truncated. The HOR branch was truncated at the point where the current was equal to 80% of the mass-transport limiting current density to remain within the kinetically-controlled potential regime. The HER branch was truncated at approximately  $-2 \text{ mA/cm}^2_{\text{disk}}$  to avoid potentials regions where hydrogen bubbles form extensively on the surface. These bubbles can interfere with the active surface area of the electrode and affect the measured current. A high electrode rotation rate can help whisk bubbles off of the electrode surface, which is why the polarization curve at 1600 rpm was chosen for the extraction of kinetic parameters. 2500 rpm was not used to ensure the supported catalysts adhered to the glassy carbon electrodes.

The fit of  $i_k$  to the Butler-Volmer equation was done using a numerical non-linear fitting program in Origin. Both  $\alpha$  and  $i_0$  were allowed to vary. All fits in this dissertation had a  $R^2$  value of 0.990 or higher.

For catalysts that are not active enough to reach the mass-transport limiting regime, a simplified analysis can be used. At high overpotential, one of the exponential terms in the Butler-Volmer equation (Equation 2-17) can be discarded since the current from the back-reaction becomes negligible. For instance, at high negative overpotential (in this case, the HER branch), the Butler-Volmer equation simplifies to

$$i_k = i_0 [e^{(-\alpha F/RT)\eta}] \quad (2-13)$$

which can be rewritten as

$$\eta = \frac{2.3RT}{\alpha F} \log(i_0) - \frac{2.3RT}{\alpha F} \log(i) \quad (2-14)$$

Plotting  $\log(i)$  vs.  $\eta$  gives what is known as a Tafel plot. An example for the Pt disk is shown in Figure 2.13.

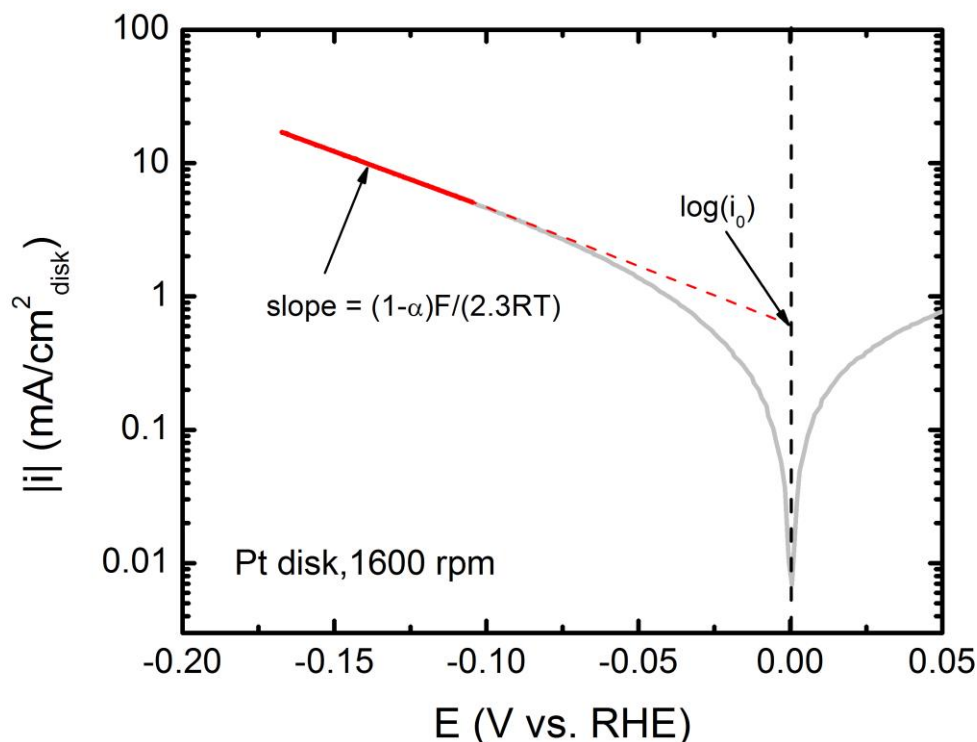


Figure 2.13: Example Tafel plot for the Pt disk at 1600 rpm in 0.1 M KOH. The grey line is the obtained polarization curve. The red line is the data selected for the linear fit to obtain  $\log(i_0)$  and the Tafel slope.

For Tafel analysis, LSV is again used to obtain a polarization curve at 1600 rpm at 10 mV/s. The potential is swept from  $\sim 1.0$  V vs. RHE to the potential corresponding to a current density of  $\sim -4.0$  mA. The polarization curve is  $iR$ -corrected using the cell resistance found with EIS, but the polarization curve is not modified to account for mass-transport, since only the HER branch of the polarization

curve is used for the Tafel analysis. A linear region of the polarization curve is chosen for a linear fit, shown in Figure 2.9 as a red line. The exchange current density is found by extrapolating the linear region to the equilibrium potential, or 0 V vs. RHE. The slope of this region is known as the Tafel slope, which is directly related to the transfer coefficient of the reaction.

It is important to note that obtaining the exchange current density using both of these methods gives a current density normalized by the geometric area of the disk. However, it is important to calculate the exchange current density normalized by the true surface area of the catalyst to compare activity between different surfaces. Therefore an appropriate surface area determination method from Chapter 2.3.4 is selected for each catalyst so that the activity can be expressed as a current density per area of catalyst and compared to other systems.

### **2.3.7 Determining Activity of Oxygenate Electrooxidation**

The measurement of the oxidation of hydrocarbon fuels, as done in Chapter 6, is simpler than for HOR/HER. In this case, CVs are collected in an electrolyte containing the feedstock of interest. The values that are important for qualitative comparison are the maximum current density and the onset potential. A high maximum current density indicates a more active catalyst, but the onset potential is more important for fuel cell applications. The onset potential is the potential at which oxidation current is first observed; a lower onset potential indicates that a catalyst is more effective for the oxidation reaction.

Before performing oxidation CVs, the electrodes were cycled in deaerated 0.1 M KOH to obtain background cyclic voltammograms for surface area determination. Ethylene glycol, glucose, or ethanol was then added to bring the solution to a

concentration of 1 M ethylene glycol, 0.1 M glucose, or 1 M ethanol. 50 CV cycles were taken to allow the system to equilibrate. CA was also completed for 3600 seconds under the same conditions to assess the steady state current at a selected potential. The system was allowed to equilibrate for 3 seconds at the chosen potential before data were collected.

## Chapter 3

### SUPPORTED MONOMETALLIC AND BIMETALLIC ELECTROCATALYSTS FOR HYDROGEN OXIDATION IN ALKALINE ELECTROLYTES

A critical aspect of developing new novel catalysts for the HOR in alkaline electrolytes is establishing trends on monometallic surfaces. In the case of HOR/HER, the thermodynamic descriptor used is the hydrogen binding energy, which is calculated using density-functional theory (DFT). Correlations between the exchange current density and the hydrogen binding energy were established for the HOR/HER in acidic and alkaline media.[14,16] However, these studies were completed on bulk foil or disk samples. Since fuel cell devices operate using carbon-supported metallic nanoparticles, it is imperative to verify the trends on more practical catalysts.

This chapter focuses on measuring exchange current densities for monometallic carbon-supported electrocatalysts and comparing the activity to the corresponding disk electrodes. Each disk electrode was tested in 0.1 M KOH to confirm the activities found in literature.

#### 3.1 Supported Electrode Preparation

Table 3.1 lists the ink recipes used for the monometallic supported catalysts. The amount of catalyst used for the ink is reported in  $\text{mg}_{\text{catalyst}}/\text{mL}_{\text{ink}}$  for simplicity.

Table 3.1: Summary of ink recipes used for monometallic supported catalysts.

Catalyst	$\text{mg}_{\text{catalyst}}/\text{mL}_{\text{ink}}$	Solvent	Drop Volume ( $\mu\text{L}$ )	$\mu\text{g}_{\text{metal}}/\text{cm}^2_{\text{disk}}$	$\mu\text{g}_{\text{carbon}}/\text{cm}^2_{\text{disk}}$
<b>40% Ag/C</b>	0.81	100% H <sub>2</sub> O	20	33	49.5
<b>40% Au/C (14 nm)</b>	1.62	50% isopropanol 50% H <sub>2</sub> O	10	33	50
<b>20% Co/C</b>	0.98	100% H <sub>2</sub> O	20	20	80
<b>20% Cu/C</b>	0.73	100% H <sub>2</sub> O	20	15	60
<b>20% Ir/C</b>	0.32	100% H <sub>2</sub> O	20	13	19.5
<b>60% Ni/C</b>	1.21	100% H <sub>2</sub> O	20	75	50
<b>40% Pd/C</b>	0.40	100% H <sub>2</sub> O	20	15	22.5
<b>46% Pt/C</b>	0.15	100% H <sub>2</sub> O	20	7	8
<b>20% Rh/C</b>	0.54	100% H <sub>2</sub> O	20	11	44

After the ink was prepared, it was sonicated in ice water for 30 minutes. The drop of ink was then deposited onto a clean, polished GC electrode with a micropipette. The electrode was covered with a beaker and left to dry overnight before use. All of the recipes listed in Table 1 resulted in homogeneous electrodes to be used for testing.

## 3.2 HOR/HER Results on Monometallic Disks and Supported Electrodes

### 3.2.1 Ag disk and 40% Ag/C

The Ag disk CV in 0.1 M KOH exhibits three anodic peaks in the forward scan and one large cathodic peak in the backward scan (Figure 3.1). The first of the anodic peaks occurs at 1.16 V vs. RHE and corresponds to the formation of a monolayer of either AgOH or Ag<sub>2</sub>O with a charge density of 400  $\mu\text{C}/\text{cm}^2_{\text{Ag}}$ . [26] The two anodic peaks at higher potentials occur due to the formation of bulk Ag oxides, which are reduced in the backward scan at 1.05 V vs. RHE. Due to the well-defined monolayer

formation associated with the first anodic peak, the surface area of Ag was calculated from the charge transferred in this process. However, integration of the peak in the CV is not accurate due to the interference from the next oxidation peak. Therefore, in order to accurately measure the charge associated with the formation of AgOH or Ag<sub>2</sub>O, the potential was held at 1.16 V vs. RHE after being equilibrated at 0.5 V vs. RHE for 60 seconds to fully reduce the surface.[27] The resulting charge transient was then integrated to find the total charge transferred (Figure 3.1b).

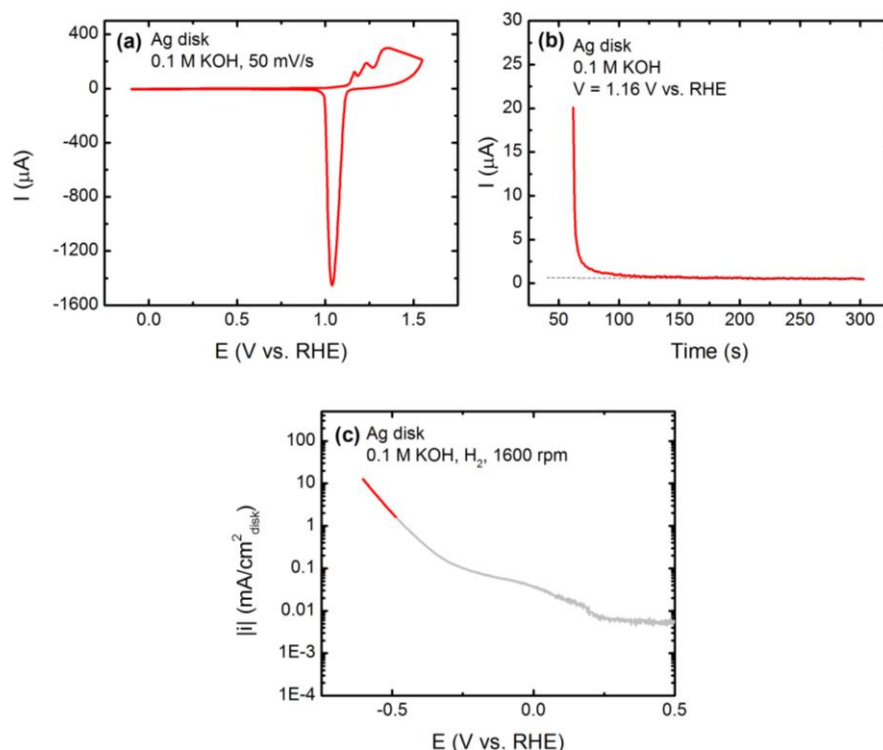


Figure 3.1: (a) CV of Ag disk in deaerated 0.1 M KOH taken at 50 mV/s. (b) CA at 1.16 V vs. RHE corresponding to the formation of a monolayer of either AgOH or Ag<sub>2</sub>O. The dashed line indicates the baseline of integration for surface area calculation. (c) LSV of Ag disk in H<sub>2</sub>-saturated 0.1 M KOH taken at 10 mV/s (grey line) and the data used for Tafel analysis (red line).

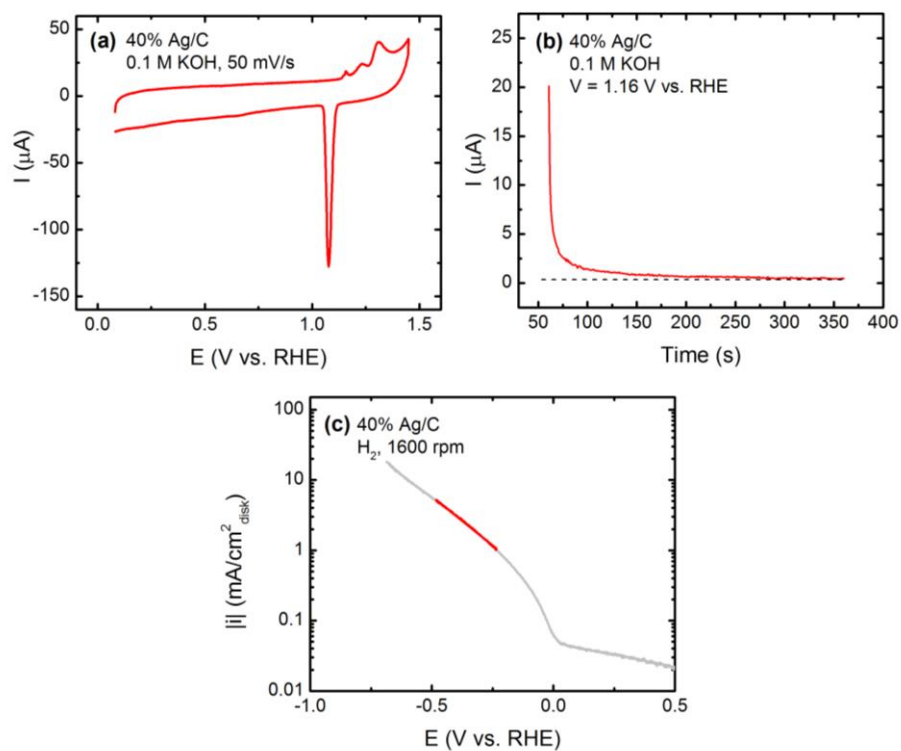


Figure 3.2: (a) CV of 40% Ag/C in deaerated 0.1 M KOH taken at 50 mV/s. (b) CA at 1.16 V vs. RHE corresponding to the formation of a monolayer of either AgOH or Ag<sub>2</sub>O. The dashed line indicates the baseline of integration for surface area calculation. (c) LSV of Ag disk in H<sub>2</sub>-saturated 0.1 M KOH taken at 10 mV/s (grey line) and the data used for Tafel analysis (red line).

This process was also used for Ag/C with similar behavior observed (Figure 3.2a,b). The CV for Ag/C displays the same anodic and cathodic peaks as the Ag disk, but the double layer current is increased due to the presence of the carbon support.

Table 3.2: Calculated roughness factors, exchange current densities, and Tafel slopes for each Ag disk and 40% Ag/C electrode.

		#1	#2	#3	#4	Average
Ag disk	<b>Roughness Factor</b> ( $\text{cm}^2_{\text{Ag}}/\text{cm}^2_{\text{disk}}$ )	1.3	1.9	1.6	1.5	<b><math>1.6 \pm 0.1</math></b>
	<b><math>\log(i_0 \text{ A}/\text{cm}^2_{\text{Ag}})</math></b>	-6.7	-6.4	-6.4	-6.2	<b><math>-6.4 \pm 0.1</math></b>
	<b>Tafel Slope</b> (mV/dec)	-129	-133	-131	-134	<b><math>-132 \pm 1</math></b>
40% Ag/C	<b>Roughness Factor</b> ( $\text{cm}^2_{\text{Ag}}/\text{cm}^2_{\text{disk}}$ )	1.7	2.3	2.2	1.9	<b><math>2.0 \pm 0.1</math></b>
	<b><math>\log(i_0 \text{ A}/\text{cm}^2_{\text{Ag}})</math></b>	-4.0	-4.0	-4.0	-4.4	<b><math>-4.1 \pm 0.1</math></b>
	<b>Tafel Slope</b> (mV/dec)	-329	-355	-303	-283	<b><math>-318 \pm 16</math></b>

Table 1 shows the exchange current densities normalized by the active Ag surface area found for each sample. The  $\log(i_0 \text{ A}/\text{cm}^2_{\text{Ag}})$  for the Ag disk was found to be  $-6.43 \pm 0.19$ , which is slightly higher than the value found by Sheng et.al.[16] The calculated  $\log(i_0 \text{ A}/\text{cm}^2_{\text{Ag}})$  for Ag/C was found to be  $-4.1 \pm 0.2$ , which is significantly larger than the value obtained for the Ag disk. In addition, the Tafel slope for Ag/C ( $-318 \pm 16$ ) is approximately twice as high as for the Ag disk ( $-132 \pm 1$ ), indicating that there is a different mechanism for Ag/C. This may be due to the increased presence of stepped surfaces on the Ag nanoparticles, which will be discussed further in section 3.3. In fact, the Tafel slope for Ag/C corresponds to a transfer coefficient of 0.19 at 298 K, while the Tafel slope of the Ag disk corresponds to 0.45. This difference is more clearly illustrated by directly comparing the LSVs for the disk and supported electrodes (Figure 3.3). While the Ag disk shows no HOR current, the 40% Ag/C attains a maximum HOR current density of  $\sim 0.40 \text{ mA}/\text{cm}^2_{\text{Ag}}$ . Ag/C also has a lower

overpotential for HER. At -0.5 V vs. RHE, the two LSVs intersect, indicating the difference in Tafel slope between the two electrodes.

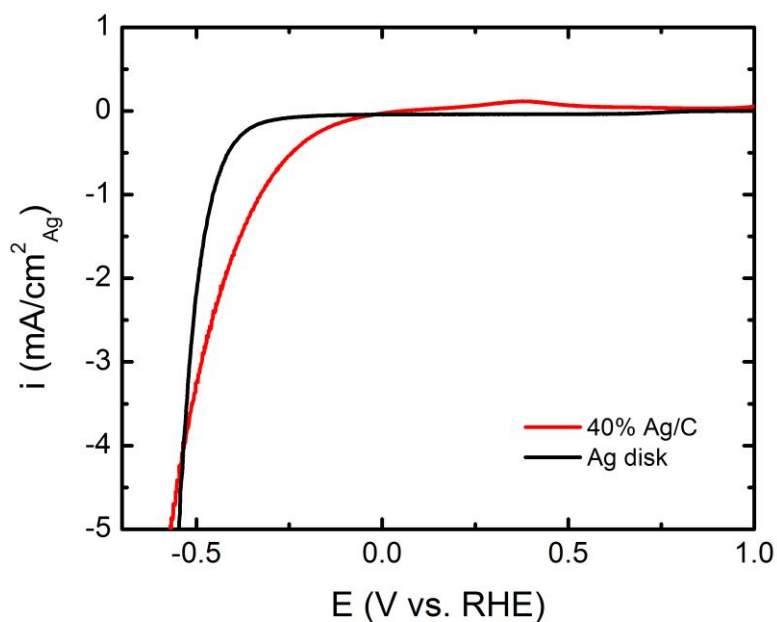


Figure 3.3: Comparison of LSVs for the Ag disk and 40% Ag/C electrode normalized by active Ag area. The substantially higher activity of Ag/C is apparent from the increased HOR current at positive potentials.

Beyond the disk electrode studies completed in Reference [16], there have not been any in-depth studies of Ag-based catalysts for the alkaline HOR. However, Ag/C catalysts have been recommended as a replacement for Pt for the alkaline ORR.[28] Although Ag/C may not be active enough alone to replace Pt for the alkaline HOR, it may be a good candidate for further experimentation through alloying.

### 3.2.2 Au disk and 40% Au/C

The Au disk CV in 0.1 M KOH exhibits features similar to Au features in NaOH; at  $\sim 0.75$  V, small, reversible features appear that are associated with the adsorption of OH on the surface, followed by the formation and reduction of AuO above  $\sim 1.0$  V (Figure 3.4a).[29] The CV for 40% Au/C retains many of the main features as the Au disk, with the main differences being a thicker double layer region and a larger cathodic current at the upper potential limit due to the carbon support (Figure 3.5a).

The surface area of Au catalysts can be determined electrochemically through the charge associated with the reduction of a monolayer of oxide at  $\sim 1.1$  V. In acidic electrolytes, the Burshtein minimum method is used to calculate the surface area of polycrystalline gold electrodes using the CV by setting the upper potential limit corresponding to the minimum cathodic current before oxygen evolution.[30,31] This same method is used here for alkaline electrolytes. For the Au disk, this upper potential limit is found to be 1.57 V vs. RHE. Using this upper potential limit ensures that one monolayer of oxide is formed, for which the charge density associated with reducing has been estimated to be  $390 \mu\text{C}/\text{cm}^2$  for polycrystalline Au electrodes.[32] Using this method, the Au disk roughness factor was calculated to be  $1.14 \pm 0.09$ , indicating that the disk is well polished. The Burshtein minimum was difficult to ascertain for the supported Au/C samples due to the increase in cathodic current at 1.57 V. Therefore, the upper potential limit of 1.57 V was used for the supported Au electrodes. The roughness factor of the supported Au/C electrodes was found to be  $1.8 \pm 0.2$ , with the relatively large error bar being likely related to a degree of variability in actual Au loading on each electrode.

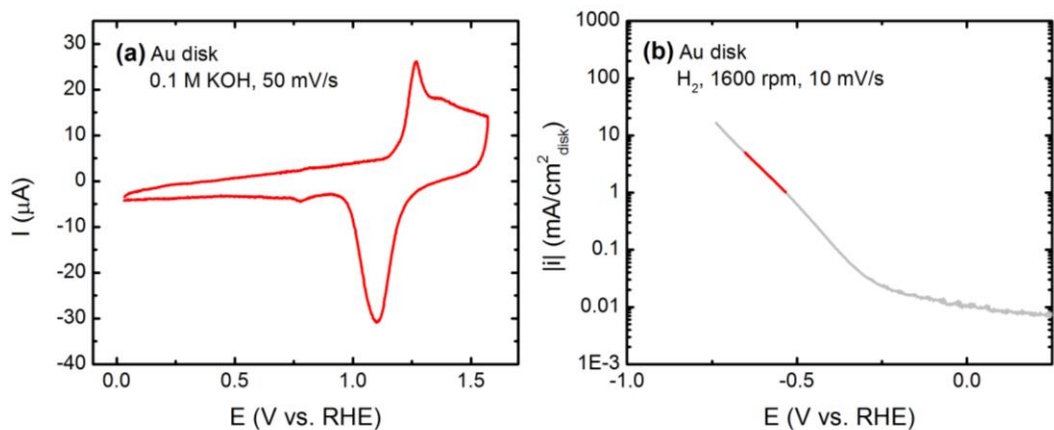


Figure 3.4: (a) CV of Au disk in deaerated 0.1 M KOH taken at 50 mV/s. (b) LSV of Au disk in  $\text{H}_2$ -saturated 0.1 M KOH taken at 10 mV/s (grey line) and the data used for Tafel analysis (red line).

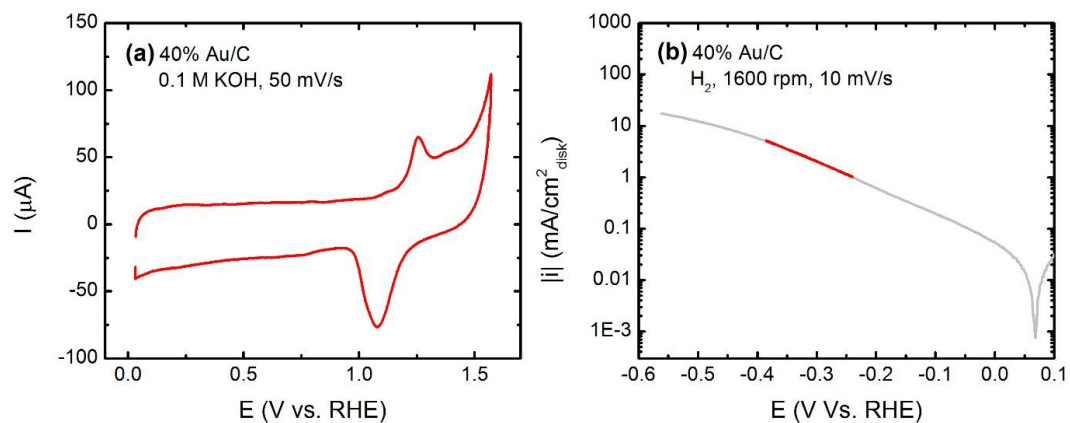


Figure 3.5: (a) CV of 40% Au/C in deaerated 0.1 M KOH taken at 50 mV/s. (b) LSV of 40% Au/C in  $\text{H}_2$ -saturated 0.1 M KOH taken at 10 mV/s (grey line) and the data used for Tafel analysis (red line).

Table 3.3: Calculated roughness factors, exchange current densities, and Tafel slopes for each Au disk and 40% Au/C electrode.

		#1	#2	#3	#4	Average
<b>Au disk</b>	<b>Roughness Factor</b> ( $\text{cm}^2_{\text{Au}}/\text{cm}^2_{\text{disk}}$ )	1.26	1.17	1.07	1.06	<b><math>1.14 \pm 0.05</math></b>
	<b><math>\log(i_0 \text{ A/cm}^2_{\text{Au}})</math></b>	-5.9	-6.0	-6.1	-6.1	<b><math>-6.1 \pm 0.1</math></b>
	<b>Tafel Slope</b> (mV/dec)	-192	-159	-173	-178	<b><math>-175 \pm 7</math></b>
<b>40% Au/C</b>	<b>Roughness Factor</b> ( $\text{cm}^2_{\text{Au}}/\text{cm}^2_{\text{disk}}$ )	1.5	1.6	2.1	1.9	<b><math>1.8 \pm 0.2</math></b>
	<b><math>\log(i_0 \text{ A/cm}^2_{\text{Au}})</math></b>	-4.4	-4.3	-4.5	-3.9	<b><math>-4.2 \pm 0.2</math></b>
	<b>Tafel Slope</b> (mV/dec)	-200	-200	-207	-198	<b><math>-201 \pm 2</math></b>

The estimated  $\log(i_0 \text{ A/cm}^2_{\text{Au}})$  of  $-6.1 \pm 0.10$  and Tafel slope of  $-175 \pm 13.8$  for the Au disk agrees with previous studies.[16,33] The calculated Tafel slope corresponds to a transfer coefficient of 0.34 at 298 K. Similar to the supported Ag/C, 40% Au/C was found to have a higher activity than the Au disk, with an average  $\log(i_0 \text{ A/cm}^2_{\text{Au}})$  value of  $-4.23 \pm 0.29$ . Unlike the Ag electrodes, the Tafel slopes of the Au disk and Au/C electrodes are similar, as the Tafel slope of the Au/C electrodes was calculated to be  $-201 \pm 2$ . This value indicates a transfer coefficient of 0.30 at 298 K. The difference in activities is illustrated by comparing the LSVs of each sample (Figure 3.6Figure ). 40% Au/C achieves a maximum HOR current density of 0.45  $\text{mA/cm}^2_{\text{Au}}$  whereas the Au disk shows almost no HOR current when normalized by the actual metal surface area. The supported electrode also has a lower overpotential for HER, though the Tafel slopes can be inferred to be nearly identical, since the LSVs do

not intersect. This is different than the case for Ag/C, where the supported catalyst has a different Tafel slope than the disk electrode.

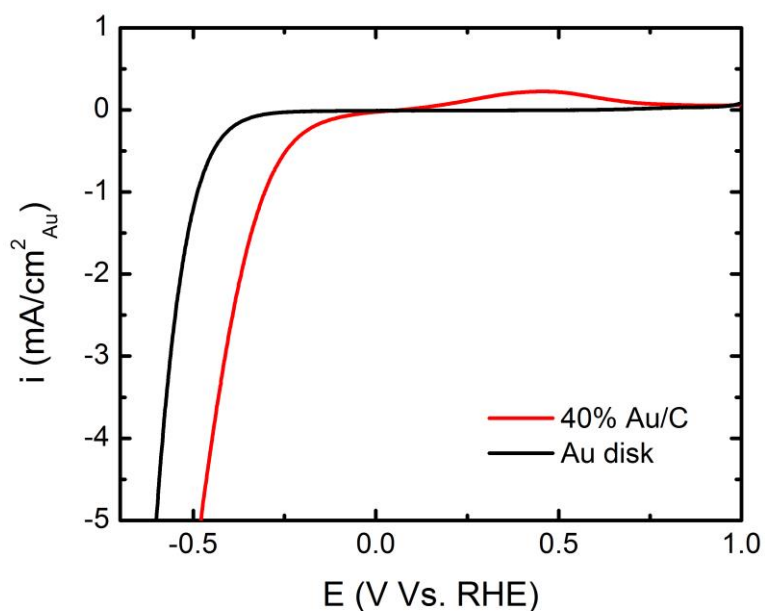


Figure 3.6: Comparison of LSVs for the Au disk and 40% Au/C electrode normalized by active Au area. The substantially higher activity of Au/C is apparent from the increased HOR current at positive potentials.

### 3.2.3 Co disk and 20% Co/C

The roughness factor of the Co disk was determined using a different method than the rest of the monometallic electrodes. First, the Co disk was cycled between  $\sim 0.87$  and  $0.97$  V vs. RHE at  $0.01$  mV/s,  $0.02$  mV/s,  $0.03$  mV/s,  $0.04$  mV/s, and  $0.05$  mV/s (Figure 3.7a). The current density was then taken at  $0.92$  V vs. RHE for each scan and plotted against the scan rate. The slope of this line was then divided by the specific capacitance of Co ( $60 \mu\text{F}/\text{cm}^2_{\text{Co}}$ ) in order to find the roughness factor.[34,35]

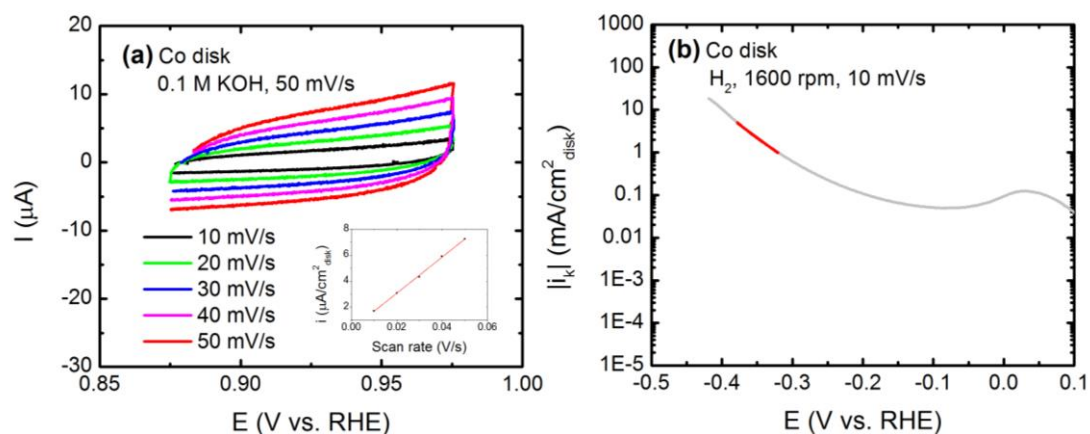


Figure 3.7: (a) CVs of Co disk at varying scan rates. The surface area was calculated by plotting the current at 0.92 V vs. RHE. The slope of that line divided by the specific capacitance gives the surface area. (b) LSV at 1600 rpm used for Tafel analysis.

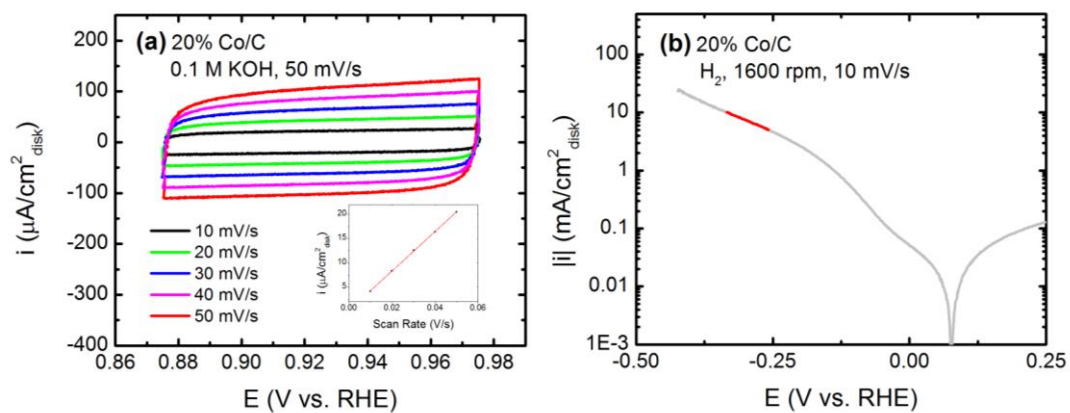


Figure 3.8: (a) CVs of 20% Co/C disk at varying scan rates. The surface area was calculated by plotting the current at 0.92 V vs. RHE. 20% of the slope of that line divided by the specific capacitance gives the surface area. (b) LSV at 1600 rpm used for Tafel analysis.

Table 3.4: Calculated roughness factors, exchange current densities, and Tafel slopes for each Au disk and 40% Au/C electrode.

		#1	#2	#3	#4	Average
Co disk	<b>Roughness Factor</b> ( $\text{cm}^2_{\text{Co}}/\text{cm}^2_{\text{disk}}$ )	2.32	2.23	2.40	2.27	<b>2.31 ± 0.04</b>
	<b>log(<math>i_0</math> A/cm<sup>2</sup><sub>Co</sub>)</b>	-6.0	-5.8	-5.7	-5.8	<b>-5.8 ± 0.1</b>
	<b>Tafel Slope</b> (mV/dec)	-126	-136	-137	-127	<b>-131 ± 3</b>
20% Co/C	<b>Roughness Factor</b> ( $\text{cm}^2_{\text{Co}}/\text{cm}^2_{\text{disk}}$ )	6.8	5.3	5.2	6.3	<b>5.9 ± 0.4</b>
	<b>log(<math>i_0</math> A/cm<sup>2</sup><sub>Co</sub>)</b>	-4.8	-5.0	-4.8	-4.2	<b>-4.7 ± 0.2</b>
	<b>Tafel Slope</b> (mV/dec)	-256	-263	-275	-259	<b>-263 ± 4</b>

The roughness factor of the 20% Co/C was estimated using a similar procedure as the Co disk. However, since the carbon support also contributes to the double layer current, the increase in current at different scan rates will not only be due to the capacitance of Co. [36] In order to find the roughness factor of the Co, an assumption was made that 20% of the slope divided by the Co specific capacitance corresponds to the roughness factor of the 20% Co/C. This assumption resulted in an average calculated roughness factor of  $5.9 \pm 0.4$ .

The average  $\log(i_0 \text{ A/cm}^2_{\text{Co}})$  for the Co disk was calculated to be  $-5.8 \pm 0.1$ , which agrees with the value found by Sheng et. al, as well as the Tafel slope of  $-131 \pm 3$ . [35] The transfer coefficient corresponding to this Tafel slope at 298 K is  $\sim 0.45$ . The Co/C electrodes were found to be more active with an average  $\log(i_0 \text{ A/cm}^2_{\text{Co}})$  of

$-4.7 \pm 0.2$ . The calculated Tafel slope of  $-263 \pm 4$  indicates a transfer coefficient of  $\sim 0.22$  at 298 K for the supported electrodes.

### 3.2.4 Cu disk and 20% Cu/C

The CV of the Cu disk in 0.1 M KOH is similar to that of a polycrystalline Cu disk in 0.1 M LiOH.[37] In the forward scan, there are 4 main peaks, labeled A-D (Figure 3.9a). Region A corresponds to the dissolution of  $\text{Cu}^+$ , region B to the formation of a submonolayer of  $\text{Cu}_2\text{O}$ , region C to the further formation of the monolayer of  $\text{Cu}_2\text{O}$ , and region D to the growth of a bulk layer of  $\text{Cu}_2\text{O}$ .[37] The reverse scan shows a number of reduction peaks at potentials that clearly depend on the upper potential limit used. Due to their variability, they were not considered for surface area calculations. Peak B was used to calculate the active surface area of the electrode, using an estimated value of  $175 \mu\text{C}/\text{cm}^2_{\text{Cu}}$  for the submonolayer of  $\text{Cu}_2\text{O}$  suggested by Fletcher et. al.[37] The calculated roughness factor of  $2.31 \pm 0.71$  agrees with the value of 1.6 – 3.7 found by Fletcher et. al.,[37] but is much lower than the value of 6.1 calculated by Sheng et. al.[16] This may be due to the age of the electrode used; an older Cu electrode will become much rougher upon cycling due to the dissolution of Cu ions. This is also observed by the large error in the roughness factor. Peak B was also used to calculate the surface area for the 20% Cu/C electrodes, which resulted in an average roughness factor of  $1.72 \pm 0.25$  (Figure 3.10a). The lower variance in roughness factor for the supported electrode might be due to the fact that a new surface was used for each test, whereas the disk electrode is used repeatedly without polishing between experiments.

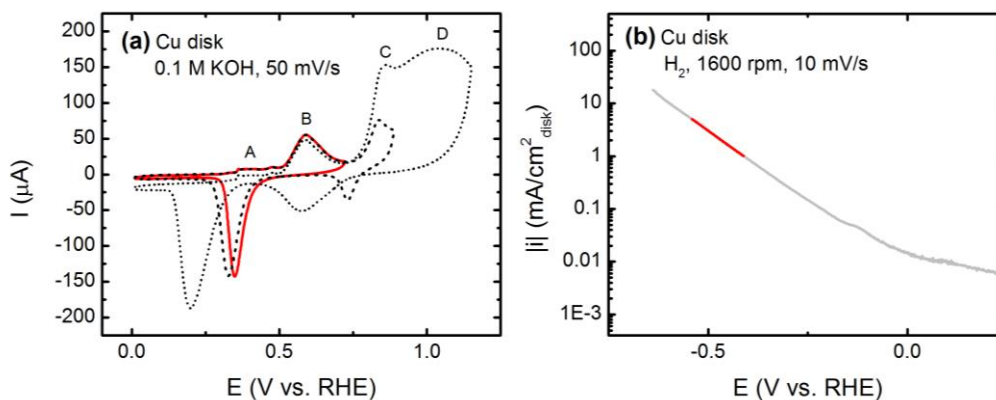


Figure 3.9: (a) CVs of the Cu disk in deaerated 0.1 M KOH taken at 50 mV/s with differing upper potential limits represented by different line textures. The red CV was used for surface area determination. (b) LSV of Cu disk in  $H_2$ -saturated 0.1 M KOH taken at 10 mV/s (grey line) and the data used for Tafel analysis (red line).

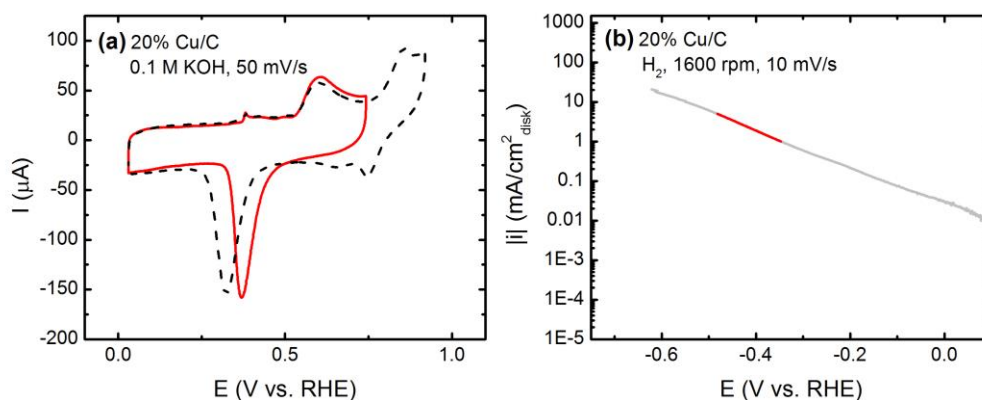


Figure 3.10: (a) CVs of 20% Cu/C in deaerated 0.1 M KOH taken at 50 mV/s with differing upper potential limits represented by different line textures. The red CV was used for surface area determination. (b) LSV of 20% Cu/C in  $H_2$ -saturated 0.1 M KOH taken at 10 mV/s (grey line) and the data used for Tafel analysis (red line).

Table 3.5: Calculated roughness factors, exchange current densities, and Tafel slopes for each Cu disk and 40% Cu/C electrode.

		#1	#2	#3	#4	Average
<b>Cu disk</b>	<b>Roughness Factor</b> ( $\text{cm}^2_{\text{Cu}}/\text{cm}^2_{\text{disk}}$ )	2.4	1.8	3.3	1.9	<b><math>2.3 \pm 0.4</math></b>
	<b><math>\log(i_0 \text{ A/cm}^2_{\text{Cu}})</math></b>	-5.6	-5.3	-5.7	-5.9	<b><math>-5.6 \pm 0.1</math></b>
	<b>Tafel Slope</b> ( <b>mV/dec</b> )	-185	-202	-176	-170	<b><math>-183 \pm 7</math></b>
<b>20% Cu/C</b>	<b>Roughness Factor</b> ( $\text{cm}^2_{\text{Cu}}/\text{cm}^2_{\text{disk}}$ )	1.7	1.6	1.5	2.0	<b><math>1.7 \pm 0.1</math></b>
	<b><math>\log(i_0 \text{ A/cm}^2_{\text{Cu}})</math></b>	-5.0	-3.8	-4.5	-4.0	<b><math>-4.3 \pm 0.3</math></b>
	<b>Tafel Slope</b> ( <b>mV/dec</b> )	-191	-333	-211	-303	<b><math>-260 \pm 35</math></b>

To avoid Cu dissolution in the HOR branch of the LSV, all Cu electrodes were equilibrated at  $\sim 0$  V vs. RHE for 60 seconds to fully reduce the Cu surface before the polarization curve was taken. The polarization curves were started at 0.3 V vs. RHE to avoid the Cu dissolution region. The average  $\log(i_0 \text{ A/cm}^2_{\text{Cu}})$  value of  $-5.62 \pm 0.26$  and the average Tafel slope of  $-183 \pm 14.0$  for the Cu disk agrees well with those found in Reference [16]. Similarly to the Ag/C and Au/C cases, the 20% Cu/C activity is significantly higher than the disk, with an average  $\log(i_0 \text{ A/cm}^2_{\text{Cu}})$  value of  $-4.3 \pm 0.5$ . The Tafel slope of  $-260 \pm 69.0$  was found to also be significantly higher than the Cu disk. The calculated Tafel slopes correspond to a transfer coefficient of 0.32 for the disk electrode and 0.23 for the supported electrodes at 298 K.

A relatively high amount of variability was found both in the exchange current density and Tafel slope for the 20% Cu/C electrodes compared to the Cu disk. A

closer look at each of the samples shows that there seems to be a bimodal distribution of activities and Tafel slopes. Samples #2 and #4 have an average  $\log(i_0 \text{ A/cm}^2_{\text{Cu}})$  value of  $-3.95 \pm 0.01$  and average Tafel slope of  $-318 \pm 15$ . Samples #1 and #3 have an average  $\log(i_0 \text{ A/cm}^2_{\text{Cu}})$  value of  $-4.74 \pm 0.3$  and average Tafel slope of  $-201 \pm 10$ . While the exchange current densities of all Cu/C samples are significantly higher than the Cu disk, the Tafel slopes of Cu/C samples #1 and #3 are equivalent to the Cu disk. However, the Tafel slopes of samples #2 and #4 are significantly higher than the Cu disk, indicating a change in mechanism. Samples #2 and #4 also have a higher activity. This may be due to changes in oxidation states of the catalyst during the LSV.

### **3.2.5 20% Ir/C**

Due to the prohibitively high cost of Ir, no Ir disk was available and therefore only supported electrodes were tested. The CV of 20% Ir/C exhibits HUPD peaks between  $\sim 0.05$  and  $0.35$  V vs. RHE and at more positive potentials, the surface is oxidized (Figure 3.11a). In order to minimize the oxide reduction current on the HUPD region, a second CV was taken after the cessation of the HUPD region to determine the active surface area. The charge density associated with the HUPD current on polycrystalline Ir surfaces in acidic electrolytes is  $198 \mu\text{C/cm}^2_{\text{Ir}}$ .<sup>[18,38]</sup> Some deviation from this value can be expected in alkaline electrolytes, but should still provide an estimate for the active surface area in basic conditions. Using this value as the charge density associated with Ir HUPD between  $0.05$  and  $0.35$  V vs. RHE in  $0.1$  M KOH yields an average calculated roughness factor of  $6.0 \pm 0.2$ .

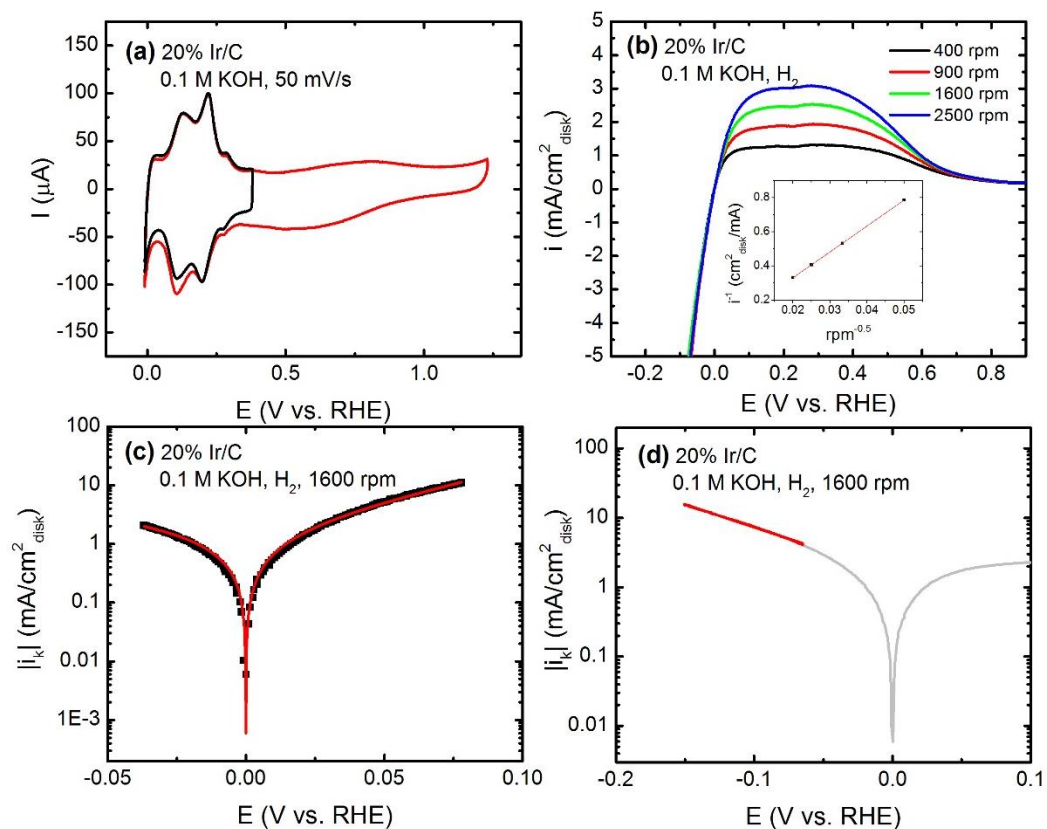


Figure 3.11: (a) CVs of 20% Ir/C at different upper potential limits. (b) HOR/HER polarization curves taken at 10 mV/s with Koutecky-Levich plot (inset). (c) LSV taken at 1600 rpm (black squares) and the fit to the Butler-Volmer equation (red line). (d) LSV taken at 1600 rpm in  $\text{H}_2$ -saturated 0.1 M KOH at 10 mV/s (grey line) and the data used for Tafel analysis (red line).

Table 3.6: Calculated roughness factors and exchange current densities (using both the Butler-Volmer equation and the Tafel equation) for 20% Ir/C.

	#1	#2	#3	#4	Average	
<b>40% Ir/C</b>	<b>Roughness Factor</b> ( $\text{cm}^2_{\text{Ir}}/\text{cm}^2_{\text{disk}}$ )	5.9	6.0	5.5	6.5	<b><math>6.0 \pm 0.2</math></b>
	<b><math>\log(i_0 \text{ A/cm}^2_{\text{Ir}})</math></b> Butler-Volmer	-3.56	-3.58	-3.53	-3.56	<b><math>-3.56 \pm 0.01</math></b>
	<b><math>\alpha_a</math></b> ( $\alpha_a + \alpha_c = 1$ )	0.66	0.52	0.63	0.54	<b><math>0.59 \pm 0.03</math></b>
	<b><math>\log(i_0 \text{ A/cm}^2_{\text{Ir}})</math></b> Tafel	-3.57	-3.51	-3.46	-3.44	<b><math>-3.50 \pm 0.03</math></b>
	<b>Tafel Slope</b> (mV/dec)	-152	-164	-161	-173	<b><math>-163 \pm 4</math></b>

Due to the high activity of Ir/C, both the Butler-Volmer and Tafel equations were used to calculate the exchange current density. The polarization curves at four different rotation rates shown in Figure 3.11b all attain a mass transport limiting current at 0.2 V vs. RHE that scale linearly with the inverse square root of the rotation rate shown. The limiting current at 2500 rpm is 3.08 as shown in Figure 3.11Figure b, which is lower than that of a Pt disk in the same conditions.[9] This has been attributed to the early onset of OH formation on the more oxophilic surface of Ir.[18] The average values of  $\log(i_0 \text{ A/cm}^2_{\text{Ir}})$  of  $-3.56 \pm 0.02$  and  $-3.50 \pm 0.06$  calculated by the Butler-Volmer and Tafel equations, respectively, are in excellent agreement and are similar to the values reported by Durst et. al. for Ir/C in 0.1 M NaOH.[18] The average  $\alpha_a$ -value of  $0.59 \pm 0.02$  obtained from a fit to the Butler-Volmer equation is significantly higher than the value of  $0.48 \pm 0.02$  found by Durst et. al., and the transfer coefficient of 0.36 obtained from the Tafel slope is much lower.[18]

### 3.2.6 Ni disk and 60% Ni/C

The CV of the Ni disk shows an oxidation peak in the anodic scan between  $\sim 0.2$  and  $0.5$  V vs. RHE corresponding to the formation of a monolayer of  $\text{Ni}(\text{OH})_2$ , which has a charge density of  $514 \mu\text{C}/\text{cm}^2_{\text{Ni}}$  (Figure 3.12a).[39] The reduction of this monolayer occurs at  $0$  V vs. RHE in the reverse scan. Due to the low current of the CV features for surface area determination, a high Ni loading of Ni/C was selected for HOR/HER testing. This made the surface area calculations more accurate since the  $\text{Ni}(\text{OH})_2$  peak is more visible. The CV for the 60% Ni/C electrodes looks qualitatively similar to the Ni disk, though the double layer region is larger due to the contributions from the carbon support (Figure 3.13a).

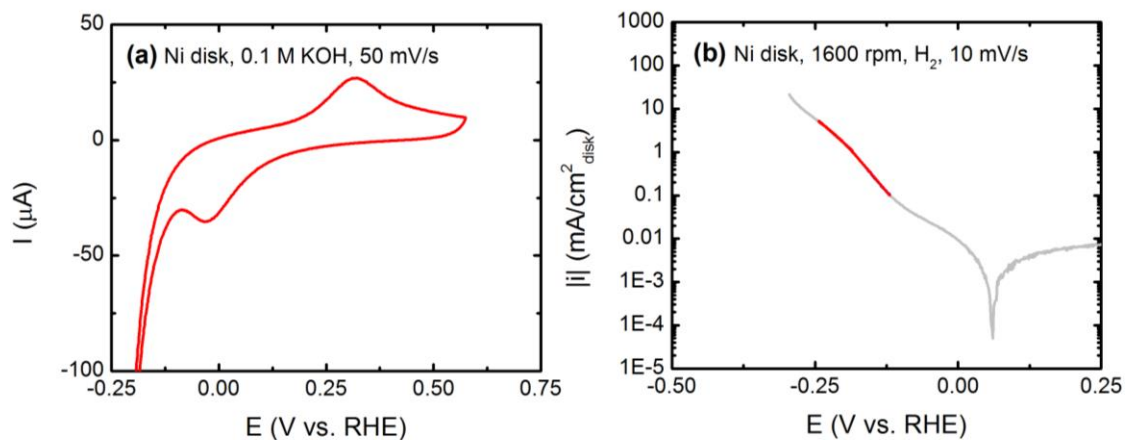


Figure 3.12: (a) CV of Ni disk in deaerated 0.1 M KOH taken at 50 mV/s. (b) LSV of Ni disk in  $\text{H}_2$ -saturated 0.1 M KOH taken at 10 mV/s (grey line) and the data used for Tafel analysis (red line).

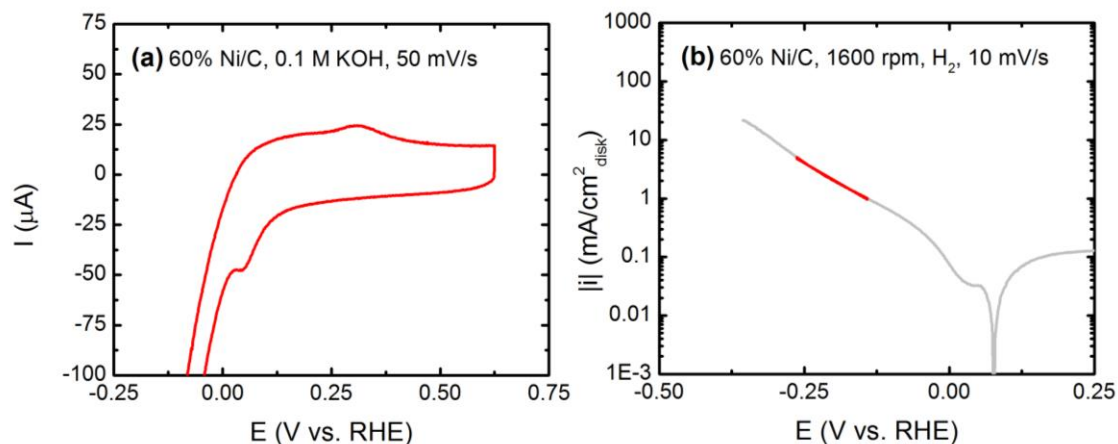


Figure 3:13: (a) CV of 60% Ni/C in deaerated 0.1 M KOH taken at 50 mV/s. (b) LSV of 60% Ni/C in  $\text{H}_2$ -saturated 0.1 M KOH taken at 10 mV/s (grey line) and the data used for Tafel analysis (red line).

Table 3.7: Calculated roughness factors, exchange current densities, and Tafel slopes for each Ni disk and 60% Ni/C electrode.

	#1	#2	#3	#4	Average	
Ni disk	<b>Roughness Factor</b> ( $\text{cm}^2_{\text{Ni}}/\text{cm}^2_{\text{disk}}$ )	1.26	1.47	1.52	1.30	<b><math>1.39 \pm 0.06</math></b>
	<b><math>\log(i_0 \text{ A}/\text{cm}^2_{\text{Ni}})</math></b>	-5.2	-5.6	-5.6	-5.6	<b><math>-5.5 \pm 0.1</math></b>
	<b>Tafel Slope</b> (mV/dec)	-65	-67	-69	-67	<b><math>66.8 \pm 1</math></b>
60% Ni/C	<b>Roughness Factor</b> ( $\text{cm}^2_{\text{Ni}}/\text{cm}^2_{\text{disk}}$ )	4.9	4.3	4.4	4.6	<b><math>4.6 \pm 0.1</math></b>
	<b><math>\log(i_0 \text{ A}/\text{cm}^2_{\text{Ni}})</math></b>	-4.9	-4.5	-4.8	-4.6	<b><math>-4.7 \pm 0.1</math></b>
	<b>Tafel Slope</b> (mV/dec)	-152	-174	-172	-164	<b><math>-166 \pm 5</math></b>

For the disk electrode, the average value of  $\log(i_0 \text{ A}/\text{cm}^2_{\text{Ni}})$  of  $-5.50 \pm 0.18$  is similar to previously reported values for polycrystalline Ni.[16,40] The calculated

Tafel slope of  $-66.8 \pm 1.71$  for the Ni disk found in this study differs significantly from the Tafel slope of  $-135 \pm 32$  reported by Sheng et. al.[16] The supported Ni catalyst is slightly more active than the disk electrode with an average  $\log(i_0 \text{ A/cm}^2_{\text{Ni}})$  of  $-4.67 \pm 0.17$  and has a different Tafel slope than the Ni disk. The Tafel slope of  $-166 \pm 9.92$  calculated for the Ni/C catalyst is closer to that reported by Sheng et al. The transfer coefficients calculated from the Tafel slopes at 298 K are 0.88 and 0.36 for the disk and supported electrodes, respectively.

### **3.2.7 Pt disk and 46% Pt/C:**

Studies of the alkaline HOR/HER on Pt are the most common among monometallic catalysts in literature.[9,18,41,42] The CV of the Pt disk (Figure 3.14a) exhibits peaks corresponding to the Pt HUPD region between 0.1 and 0.5 V vs. RHE, followed by the formation of Pt oxides above 0.6 V.[9,43] In order to find the active surface area, the CV was cut short in order to minimize the influence of the oxide region on the HUPD region, as shown by the black line in Figure 3.14a. The charge density associated with either the formation or stripping of the Pt-H species is  $210 \mu\text{C/cm}^2_{\text{Pt}}$ . Therefore, the surface area of the Pt samples was found using the average area under both the anodic and cathodic HUPD regions integrated from 0.05 V to 0.45 V vs. RHE.[9,44] The average roughness factor of the Pt disk was calculated to be  $1.1 \pm 0.1$ , indicating the disk is well polished for all tests.

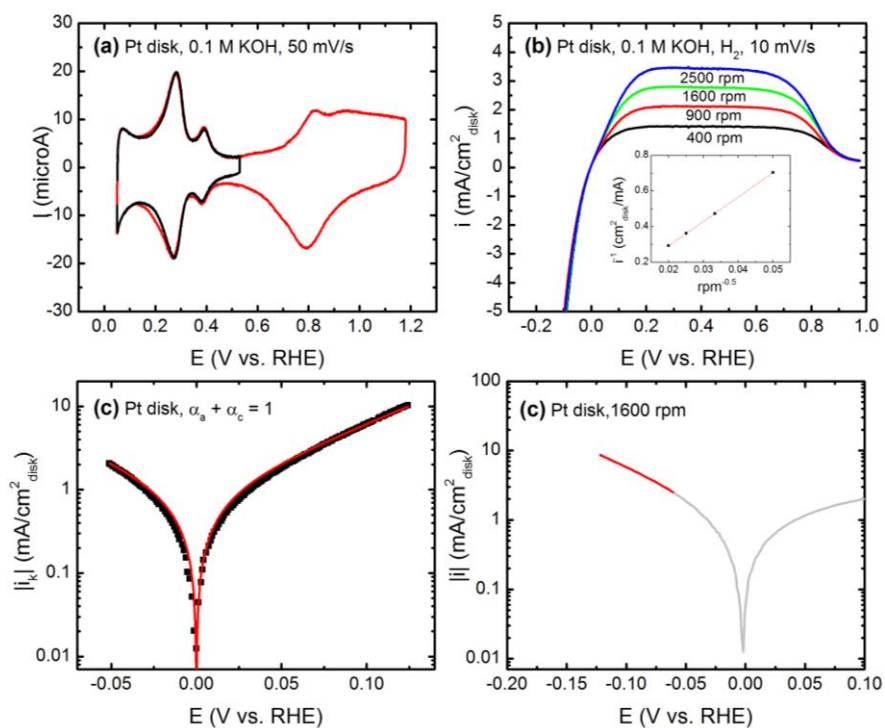


Figure 3.14: (a) CVs of the Pt disk at different upper potential limits. (b) HOR/HER polarization curves taken at 10 mV/s with Koutecky-Levich plot (inset). (c) LSV taken at 1600 rpm (black squares) and the fit to the Butler-Volmer equation (red line). (d) LSV taken at 1600 rpm in  $H_2$ -saturated 0.1 M KOH at 10 mV/s (grey line) and the data used for Tafel analysis (red line).

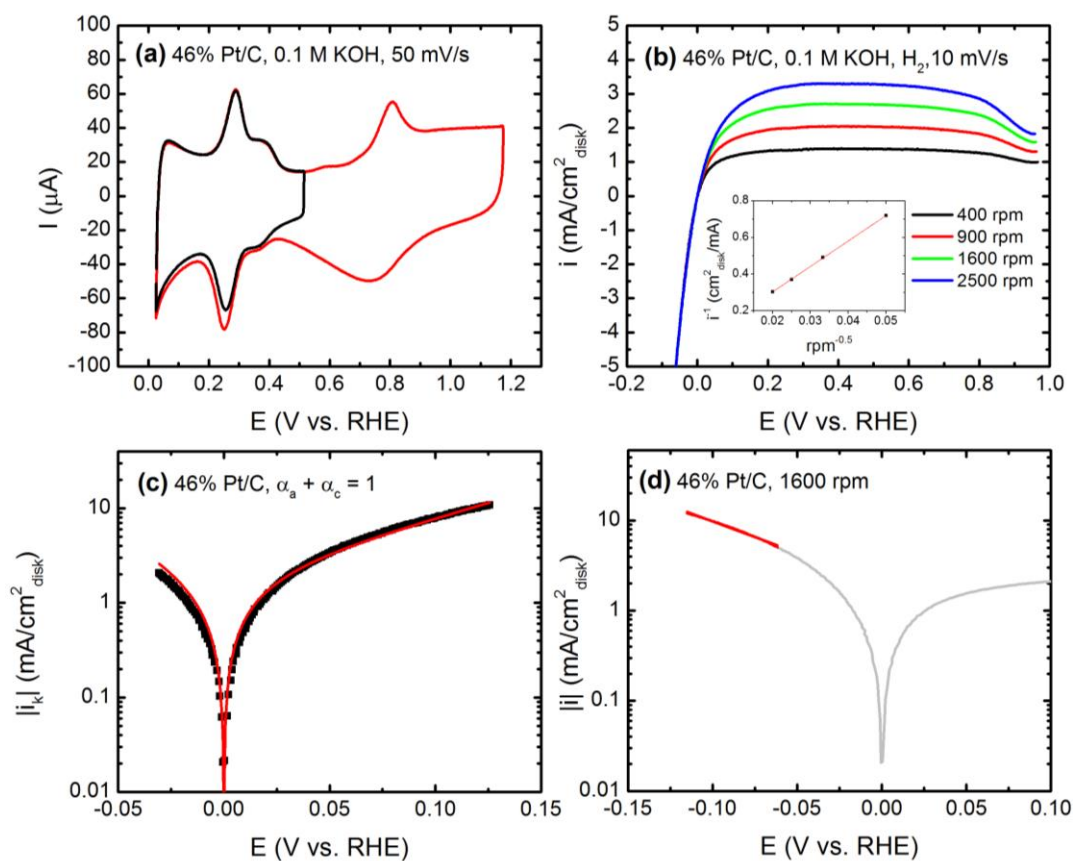


Figure 3.15: (a) CVs of 46% Pt/C at different upper potential limits. (b) HOR/HER polarization curves taken at 10 mV/s with Koutecky-Levich plot (inset). (c) LSV taken at 1600 rpm (black squares) and the fit to the Butler-Volmer equation (red line). (d) LSV taken at 1600 rpm in H<sub>2</sub>-saturated 0.1 M KOH at 10 mV/s (grey line) and the data used for Tafel analysis (red line).

The same procedure was used for the 46% Pt/C, resulting in an average roughness factor of  $4.1 \pm 0.2$ , which agrees with values found for similar electrodes.[9]

Table 3.8: Calculated roughness factors, exchange current densities, and Tafel slopes for each Pt disk and 46% Pt/C electrode.

	#1	#2	#3	#4	Average	
<b>Pt disk</b>	<b>Roughness Factor</b> ( $\text{cm}^2_{\text{Pt}}/\text{cm}^2_{\text{disk}}$ )	1.3	1.0	1.0	1.2	<b><math>1.1 \pm 0.1</math></b>
	<b><math>\log(i_0 \text{ A/cm}^2_{\text{Pt}})</math></b> Butler-Volmer	-3.28	-3.28	-3.19	-3.23	<b><math>-3.23 \pm 0.03</math></b>
	<b><math>\alpha_a</math></b> ( $\alpha_a + \alpha_c = 1$ )	0.57	0.5	0.51	0.49	<b><math>0.52 \pm 0.02</math></b>
	<b><math>\log(i_0 \text{ A/cm}^2_{\text{Pt}})</math></b> Tafel	-3.23	-3.18	-3.08	-3.17	<b><math>-3.17 \pm 0.03</math></b>
	<b>Tafel Slope</b> (mV/dec)	-116	-120	-113	-98.5	<b><math>-112 \pm 5</math></b>
<b>46% Pt/C</b>	<b>Roughness Factor</b> ( $\text{cm}^2_{\text{Pt}}/\text{cm}^2_{\text{disk}}$ )	4.1	4.3	3.5	4.5	<b><math>4.1 \pm 0.2</math></b>
	<b><math>\log(i_0 \text{ A/cm}^2_{\text{Pt}})</math></b> Butler-Volmer	-3.19	-3.38	-3.32	-3.39	<b><math>-3.32 \pm 0.05</math></b>
	<b><math>\alpha_a</math></b> ( $\alpha_a + \alpha_c = 1$ )	0.48	0.38	0.5	0.56	<b><math>0.48 \pm 0.04</math></b>
	<b><math>\log(i_0 \text{ A/cm}^2_{\text{Pt}})</math></b> Tafel	-3.34	-3.34	-3.30	-3.38	<b><math>-3.34 \pm 0.02</math></b>
	<b>Tafel Slope</b> (mV/dec)	-94	-144	-120	-149	<b><math>-127 \pm 13</math></b>

Both the Butler-Volmer equation as well as the Tafel equation were used to calculate the activity of both the Pt disk and the 46% Pt/C to compare the two methods (Table 3.8). For the Pt disk, the calculated activity from each method agrees very well. The Tafel slope of  $-112 \pm 5$  found for the Pt disk corresponds to a transfer coefficient of  $\sim 0.53$  at 298 K, which matches the transfer coefficient of  $0.52 \pm 0.02$  found from the fit to Butler-Volmer. Similarly for the 46% Pt/C electrode, both methods give almost identical exchange current density values. The Tafel slope calculated for the 46% Pt/C electrode is  $-127 \pm 13$ , which corresponds to a transfer

coefficient of  $\sim 0.47$ . This agrees well with the transfer coefficient of  $0.48 \pm 0.04$  calculated using the Butler-Volmer method. Since the transfer coefficients are close to 0.5 for a fit that assumes  $\alpha_a + \alpha_c = 1$ , the HOR and HER are considered symmetric with respect to the equilibrium potential. Sheng et. al. used a fixed value of  $\alpha_a = 0.5$  when fitting Pt and Pt/C kinetic data. In the data reported above, the transfer coefficient parameter was allowed to float, therefore removing the assumption of symmetry. However, the calculated transfer coefficients were very close to 0.5, indicating that it is a good assumption that the HOR and HER are symmetric for Pt. Durst et. al. found a transfer coefficient of  $0.38 \pm 0.08$  for Pt/C in 0.1 M NaOH using an RDE.[18] While the transfer coefficient found for 46% Pt/C is indeed slightly less than 0.5, it is still higher than what is found by Durst et. al. This may be due to the difference in electrolyte used or difference in measurement techniques.

Since HOR/HER is most studied on Pt, the mechanism differences between acidic and alkaline HOR/HER has primarily been discussed on Pt surfaces. The HOR/HER proceeds either by the Tafel-Volmer or Heyrovsky-Volmer mechanism, as discussed in Chapter 1. The only difference between acidic and basic media that can be explicitly drawn from the mechanism is the appearance of the  $\text{OH}^-$  ion in the mechanism written in basic media. This does not explain the decrease in activity of the HOR/HER on Pt in basic media. One preliminary explanation for the decrease in activity is that the active form of OH in the HOR/HER mechanism in alkaline electrolytes is  $\text{OH}_{\text{ad}}$ , and therefore the energetics of that species also become important.[45] However, it has recently been shown that the activity of Pt only depends on the hydrogen binding energy, and likely does not depend on the adsorption

of OH.[46] The shift in hydrogen binding energy on Pt between acidic and alkaline electrolytes may stem from the increased presence of OH<sup>-</sup> near the electrode surface.

### 3.2.8 Pd disk and 40% Pd/C

The CV of the Pd disk (Figure 3.16a) exhibits peaks corresponding Pd-hydrogen interactions between  $\sim 0.05$  V and 0.5 V vs. RHE. Above 0.5 V vs. RHE, the Pd surface is oxidized. In the reverse scan, the Pd oxides are reduced at 0.75 V vs. RHE, which corresponds to charge density of  $424 \mu\text{C}/\text{cm}^2_{\text{Pd}}$ . [47] Although this charge density is only accurate for a 2-electron process on Pd(100), it was recommended as a standard value for all polycrystalline Pd surfaces. [47] Using this reduction peak for the determination of the active surface area results in a roughness factor of  $1.15 \pm 0.04$  (Table 3.9), indicating that the disk electrode is well polished.

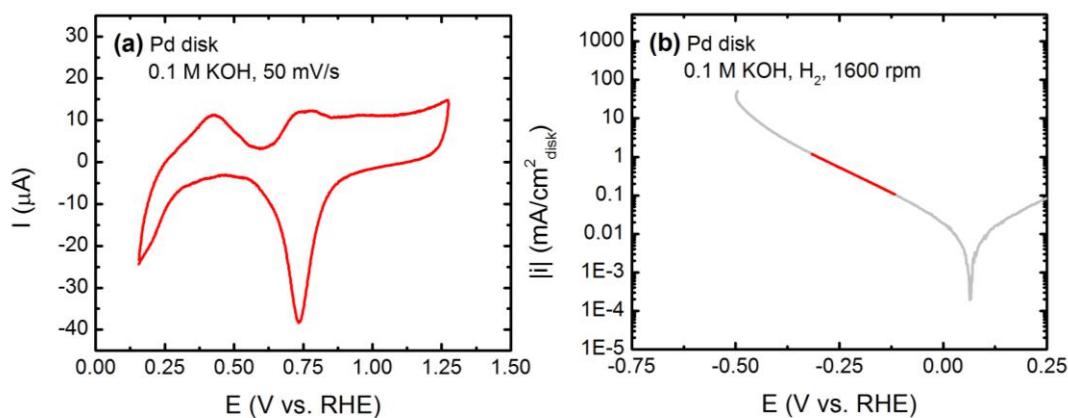


Figure 3.16: (a) CV of Pd disk in 0.1 M KOH. (b) LSV taken at 1600 rpm in H<sub>2</sub>-saturated 0.1 M KOH at 10 mV/s (grey line) and the data used for Tafel analysis (red line).

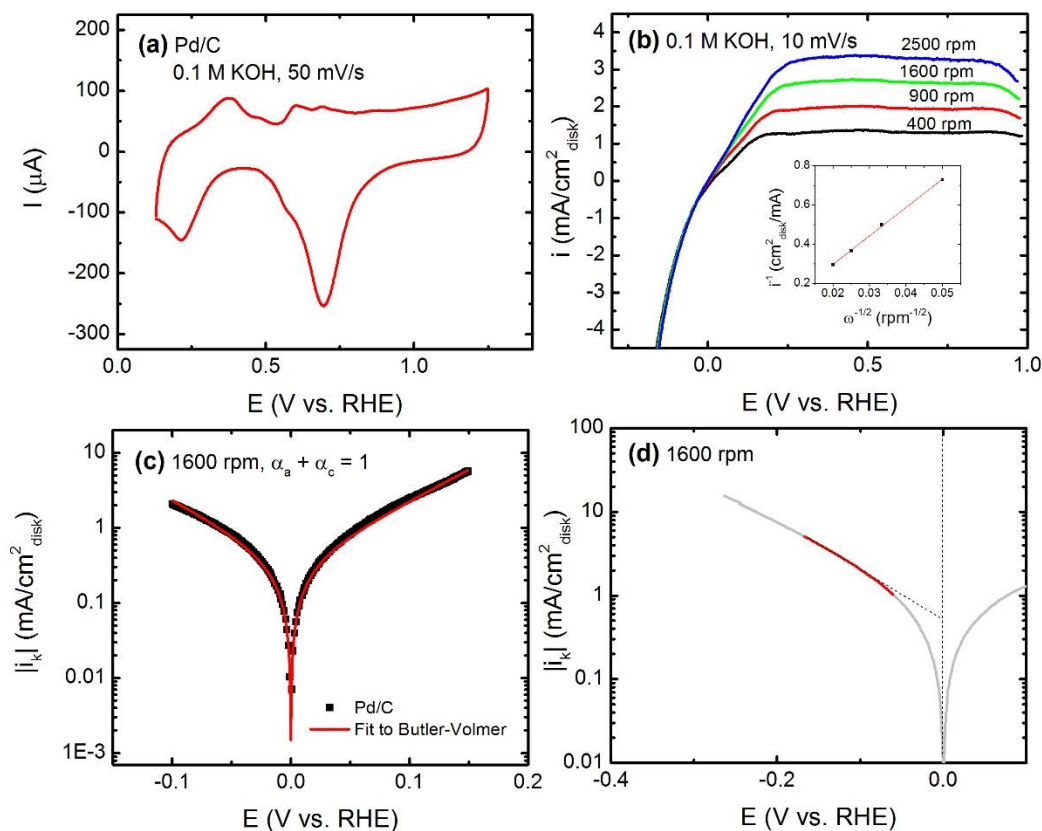


Figure 3.17: (a) CV of 40% Pd/C in 0.1 M KOH. (b) HOR/HER polarization curves taken at 10 mV/s with Koutecky-Levich plot (inset). (c) LSV taken at 1600 rpm (black squares) and the fit to the Butler-Volmer equation (red line). (d) LSV taken at 1600 rpm in  $\text{H}_2$ -saturated 0.1 M KOH at 10 mV/s (grey line) and the data used for Tafel analysis (red line).

The CV of 40% Pd/C appears to be similar to the Pd disk, though more fine CV features are seen in both the Pd-hydrogen and Pd oxide region. This is likely due to the presence of different Pd facets than are present on the Pd disk. Nevertheless, the same reduction peak was used to calculate the roughness factor of the supported electrodes, resulting in an average roughness factor of  $8.5 \pm 0.3$ .

Table 3.9 Calculated roughness factors, exchange current densities, and Tafel slopes for each Pt disk and 46% Pt/C electrode.

		#1	#2	#3	#4	Average
<b>Pd disk</b>	<b>Roughness Factor</b> ( $\text{cm}^2_{\text{Pd}}/\text{cm}^2_{\text{disk}}$ )	1.05	1.17	1.24	1.13	<b>1.15 ± 0.04</b>
	<b>log(<math>i_0</math> A/cm<sup>2</sup><sub>Pd</sub>)</b> Tafel	-4.6	-4.6	-4.1	-4.3	<b>-4.4 ± 0.1</b>
	<b>Tafel Slope</b> (mV/dec)	-192	-177	-220	-203	<b>-198 ± 9</b>
<b>40% Pd/C</b>	<b>Roughness Factor</b> ( $\text{cm}^2_{\text{Pd}}/\text{cm}^2_{\text{disk}}$ )	9.2	8.2	8.1	8.4	<b>8.5 ± 0.3</b>
	<b>log(<math>i_0</math> A/cm<sup>2</sup><sub>Pd</sub>)</b> Butler-Volmer	-4.5	-4.4	-4.6	-4.1	<b>-4.4 ± 0.1</b>
	<b><math>\alpha_a</math></b> ( $\alpha_a + \alpha_c = 1$ )	0.49	0.48	0.43	0.45	<b>0.46 ± 0.01</b>
	<b>log(<math>i_0</math> A/cm<sup>2</sup><sub>Pd</sub>)</b> Tafel	-4.3	-4.2	-4.1	-4.0	<b>-4.2 ± 0.1</b>
	<b>Tafel Slope</b> (mV/dec)	-158	-162	-204	-148	<b>-168 ± 12</b>

The Pd disk was not active enough to achieve the mass transport limiting current density for this study. Therefore, only the Tafel analysis was used to extract kinetic parameters. The average  $\log(i_0 \text{ A/cm}^2_{\text{Pd}})$  value found for the Pd disk was  $-4.4 \pm 0.1$ , slightly lower than the activity found by Sheng et. al.[16] The calculated Tafel slope of the Pd disk was  $-198 \pm 9$ , which corresponds to a transfer coefficient of  $\sim 0.30$  at 298 K.

Since the surface area of the 40% Pd/C electrodes was much higher than the Pd disk, the supported electrodes were able to reach the mass transport limiting current density. Therefore, both the Butler-Volmer and Tafel methods were used to calculate the HOR/HER activity. The Butler-Volmer fitting yields a  $\log(i_0 \text{ A/cm}^2_{\text{Pd}})$  value of -

$4.4 \pm 0.1$ , which agrees excellently with the activity found for the Pd disk. The Tafel equation gives a  $\log(i_0 \text{ A/cm}^2_{\text{Pd}})$  value of  $-4.2 \pm 0.1$ , which is similar to the activity measured by Durst et. al. in 0.1 M NaOH.[18] The Tafel slope calculated for 40% Pd/C was  $-168 \pm 12$ , which corresponds to a transfer coefficient of  $\sim 0.35$  at 298 K. This is much lower than the transfer coefficient of  $0.46 \pm 0.01$  found using the Butler-Volmer equation. Previous studies of Pd/C in acidic environments have found the transfer coefficient to be as low as 0.35, while studies of Pd/C in 0.1 M NaOH calculated a transfer coefficient of 0.43. The large variation in these quantities may be due to the absorption of hydrogen into the crystalline lattice, which occurs easily on Pd. The adsorbed hydrogen may skew the measured kinetics from test to test. However, since Pd/C used in an actual fuel cell is subject to hydrogen, the kinetics parameters found in this study should be considered accurate for a realistic fuel cell system.

### **3.2.9 20% Rh/C**

Similar to the case for Ir, no Rh disk electrode was available. Therefore, only supported Rh/C was tested. The CV of 20% Rh/C is similar to other Pt group metals in that it has a Rh-hydrogen region and an Rh oxide region (Figure 3.18a). CV peaks corresponding to the HUPD region on Rh occur between  $\sim 0$  V and 0.4 V vs. RHE. The Rh oxide region overlaps the HUPD region, but the CV was truncated to minimize interference from the oxide current. The charge density corresponding to the Rh HUPD region has been estimated to be  $221 \mu\text{C/cm}^2_{\text{Rh}}$ . [47] The average area under each branch of the HUPD region was calculated for determining the active surface area and roughness factor, which was found to be  $13.6 \pm 0.4$ .

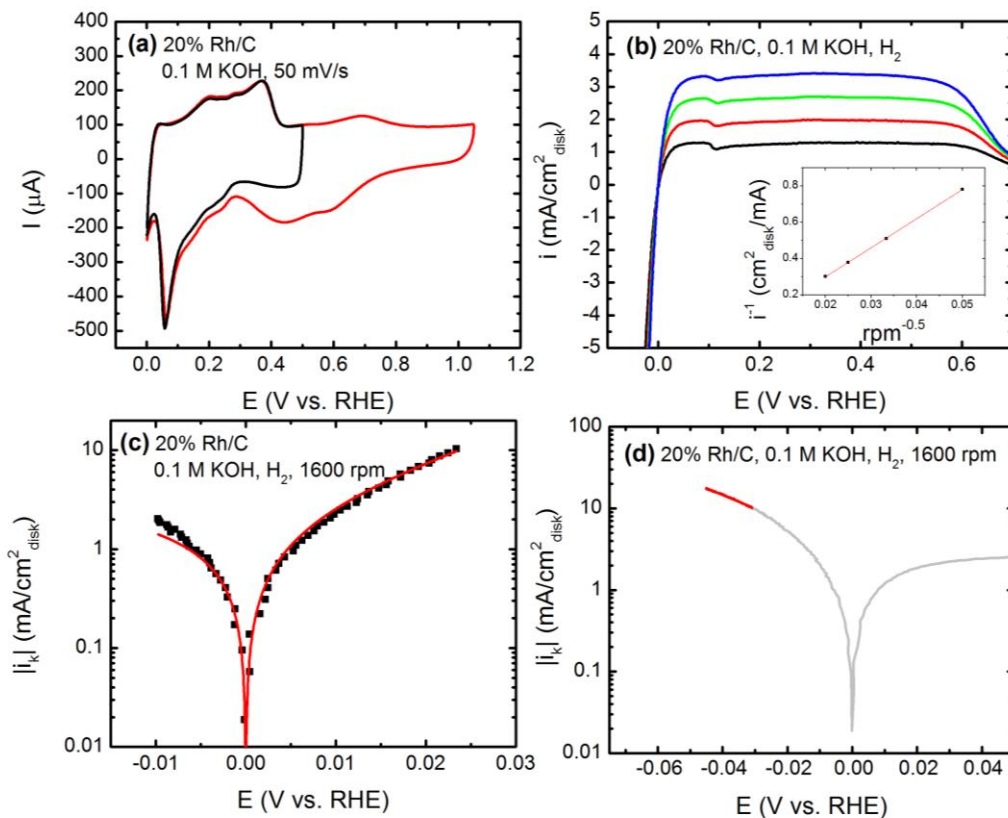


Figure 3.18: (a) CVs of 20% Rh/C at different upper potential limits. (b) HOR/HER polarization curves taken at 10 mV/s with Koutecky-Levich plot (inset). (c) LSV taken at 1600 rpm (black squares) and the fit to the Butler-Volmer equation (red line). (d) LSV taken at 1600 rpm in  $\text{H}_2$ -saturated 0.1 M KOH at 10 mV/s (grey line) and the data used for Tafel analysis (red line).

Table 3.10: Calculated roughness factors and exchange current densities (using both the Butler-Volmer equation and the Tafel equation) for 20% Rh/C.

	#1	#2	#3	#4	Average	
<b>20% Rh/C</b>	<b>Roughness Factor</b> ( $\text{cm}^2_{\text{Rh}}/\text{cm}^2_{\text{disk}}$ )	14.8	13.2	12.9	13.5	<b>13.6 ± 0.4</b>
	<b>log(<math>i_0</math> A/cm<sup>2</sup><sub>Rh</sub>)</b> Butler-Volmer	-3.79	-3.68	-3.73	-3.67	<b>-3.72 ± 0.02</b>
	<b><math>\alpha_a</math></b> ( $\alpha_a + \alpha_c = 2$ )	1.74	1.34	1.62	1.48	<b>1.55 ± 0.09</b>
	<b>log(<math>i_0</math> A/cm<sup>2</sup><sub>Rh</sub>)</b> Tafel	-3.67	-3.52	-3.58	-3.64	<b>-3.60 ± 0.03</b>
	<b>Tafel Slope</b> (mV/dec)	-60.4	-75.3	-68.0	-73.4	<b>69.3 ± 3</b>

The Rh/C electrodes shows that the polarization curves for HOR reach the mass transport limiting current density (Figure 3.18b). When using the Butler-Volmer equation to calculate the kinetic parameters, using the constraint of  $\alpha_a + \alpha_c = 1$  did not result in a physically viable answer. The best fit of the Butler-Volmer equation occurred when the constraint was changed to  $\alpha_a + \alpha_c = 2$ . Therefore all calculated transfer coefficients were over 1, with the average value being  $1.55 \pm 0.09$ . This suggests that the HOR/HER on Rh occurs through a different mechanism than on Pt.

There is a good agreement between the exchange current densities calculated from both methods. The Butler-Volmer equation yields an exchange current density of  $-3.72 \pm 0.02$ , compared to  $-3.60 \pm 0.03$  calculated from the Tafel equation. The Tafel slope of  $-69.3 \pm 3$  corresponds to a transfer coefficient of 0.85 at 298 K, indicating that there is some discrepancy between the methods for the Rh/C electrodes.

### 3.2.10 W and Fe Disks

Due to the difficulty determining the actual surface area of Fe and W, the current densities were normalized by the disk area. This only allows the accurate testing of a flat electrode, so no supported catalysts were investigated.

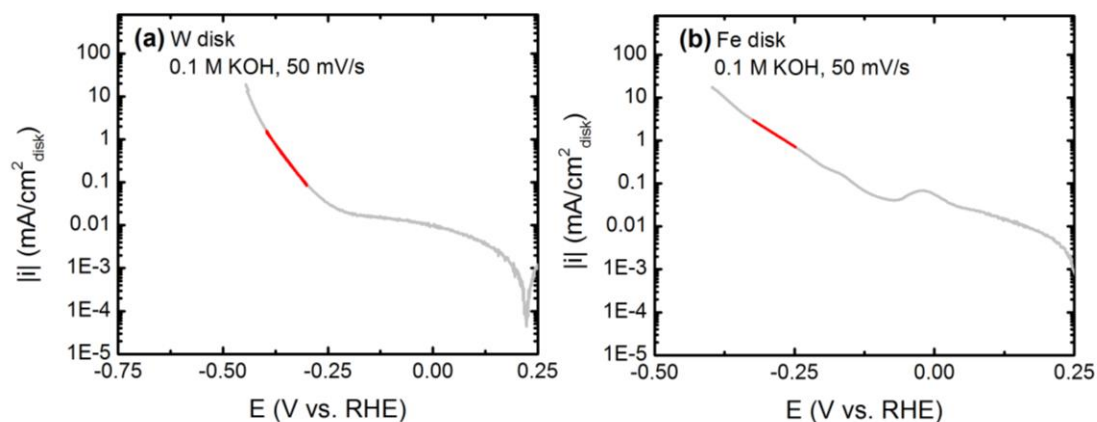


Figure 3.19: (a) LSV taken at 1600 rpm in  $\text{H}_2$ -saturated 0.1 M KOH (grey line) and the data used for Tafel analysis on the W disk. (b) LSV taken at 1600 rpm in  $\text{H}_2$ -saturated 0.1 M KOH at 10 mV/s (grey line) and the data used for Tafel analysis (red line) on the Fe disk.

Table 3.11: Calculated exchange current densities and Tafel slopes for each W and Fe disk electrode.

		#1	#2	#3	#4	Average
W disk	$\log(i_0 \text{ A/cm}^2_{\text{disk}})$	-7.89	-7.89	-7.97	-8.07	<b>-7.96 ± 0.04</b>
	Tafel Slope (mV/dec)	75.7	76.1	77.2	75.5	<b>76.1 ± 0.4</b>
Fe disk	$\log(i_0 \text{ A/cm}^2_{\text{disk}})$	-5.6	-5.6	-5.2	-5.2	<b>-5.4 ± 0.1</b>
	Tafel Slope (mV/dec)	-103	-101	-122	-122	<b>-112 ± 6</b>

The W disk was found to be very inactive in alkaline conditions, with a  $\log(i_0 \text{ A/cm}^2_{\text{disk}})$  value of  $-7.96 \pm 0.04$ . This activity is lower than what is found in literature.[16] However, since the area of the disk is being used to normalize the exchange current density, the quality of the disk electrode is very important in acquiring consistent data. The disk used in this study was brand new and therefore the kinetic parameters were found to be very consistent between trials. An older disk that has been polished significantly may become curved and therefore give skewed results. The Tafel slope of  $-76.1 \pm 0.1$  corresponds to a transfer coefficient of  $\sim 0.75$  at 298 K. This indicates the mechanism may be different on W than Pt.

The  $\log(i_0 \text{ A/cm}^2_{\text{disk}})$  value of  $-5.4 \pm 0.1$  found for the Fe disk was also lower than in previous studies.[16] This, again, may be due to the quality of the electrode used for testing. The Tafel slope of  $-112 \pm 6$  calculated for the Fe disk corresponds to a transfer coefficient of  $\sim 0.53$  at 298 K, suggesting that the HOR/HER is symmetric for the Fe surface.

### **3.3 Volcano Relationship for Supported Monometallic Catalysts**

The HER LSVs of each monometallic disk and supported electrode are compared in Figure 3.20. Each metal exhibits a different overpotential for the HER reaction, with Pt having the lowest and Ag having the highest. The LSVs for the disk electrodes do not change substantially when normalized by the actual metal area surface area (Figure 3.20b) instead of the disk area due to the relatively low roughness factors. The LSVs of the monometallic supported electrodes follow the same general trends as the disk electrodes. Specifically, Pt/C and Pt group metals have the lowest HER overpotential while Ag/C has the highest. However, the HER overpotential of each of the supported electrodes is generally lower than the corresponding disk

electrode. Due to the varying roughness factors of each supported catalyst electrode, the LSVs trends change when the current is normalized by the actual surface area of the catalyst, especially for the electrodes with a high roughness factor, such as Pd/C and Rh/C.

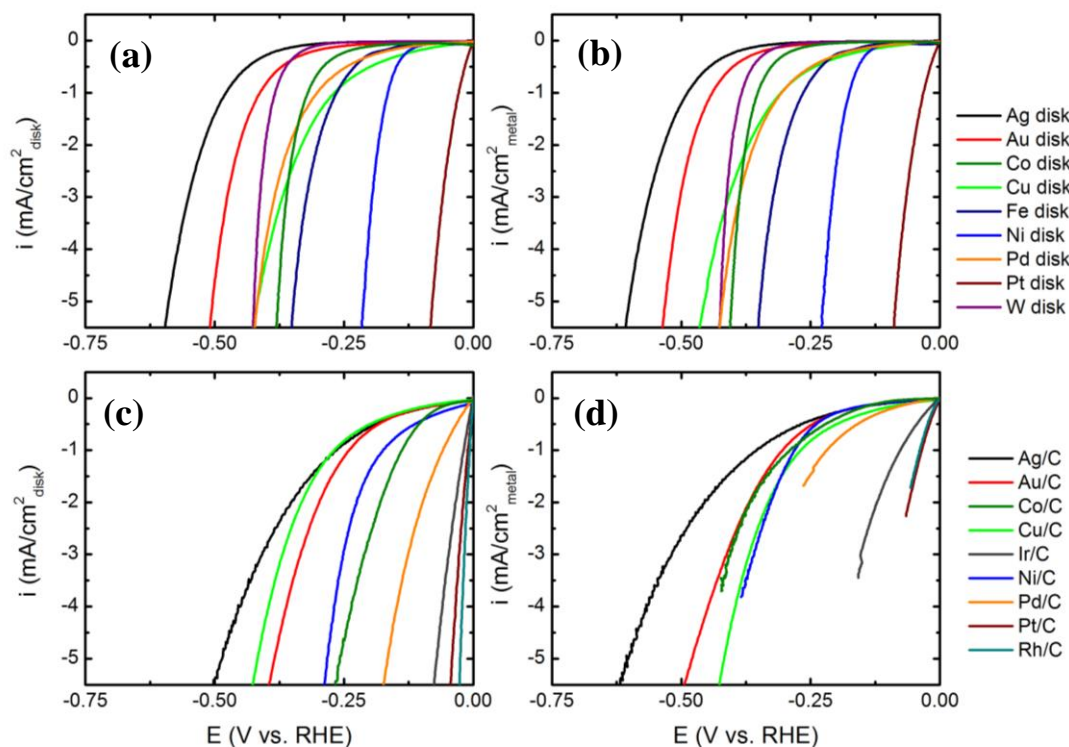


Figure 3.20: LSVs of (a),(b) monometallic disk electrodes and (c),(d) supported monometallic electrodes. The current densities are normalized both by the geometric and actual area of the electrode.

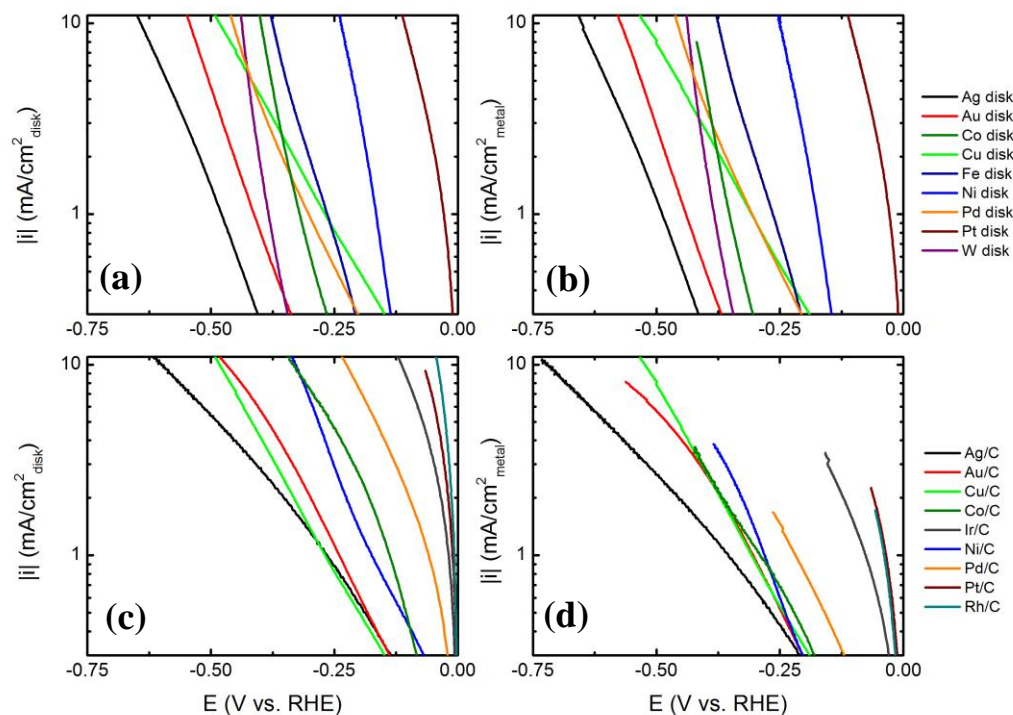


Figure 3.21: Tafel plots of (a),(b) monometallic disk electrodes and (c),(d) supported monometallic electrodes. The current densities are normalized both by the geometric and actual area of the electrode.

The Tafel plots of each disk and supported electrode are compared in Figure 3.21. The slope of each line was extrapolated to 0 V vs. RHE to find the exchange current density, except for the metals that the Tafel method was not appropriate (Pt/C, Ir/C, Pd/C, and Rh/C). A comparison of the Tafel plots of the disk and supported electrodes shows the significantly different Tafel slope for the supported catalysts.

Table 3.12: Summary of hydrogen binding energies, exchange current densities and Tafel slopes for each disk and supported catalyst electrode. The Fe and W disks are normalized by the geometric area of the disk only.

Catalyst	Hydrogen Binding Energy (eV)	$\log(i_0)$ A/cm <sup>2</sup> <sub>metal</sub> Disk	Tafel Slope (mV/dec) Disk	$\log(i_0)$ A/cm <sup>2</sup> <sub>metal</sub> Supported	Tafel Slope (mV/dec) Supported
Ag	0.27 [14]	-6.4 ± 0.1	132 ± 1	-4.1 ± 0.1	-318 ± 16
Au	0.21 [14]	-6.1 ± 0.1	175 ± 7	-4.2 ± 0.3	-201 ± 2
Co	-0.51 [14]	-5.8 ± 0.1	131 ± 3	-4.7 ± 0.2	-263 ± 4
Cu	-0.05 [14]	-5.6 ± 0.1	183 ± 7	-4.3 ± 0.3	-260 ± 35
Fe	-0.59 [16]	-5.4 ± 0.1	112 ± 6	--	--
Ir	-0.21 [14]	--	--	-3.50 ± 0.03	-163 ± 4
Ni	-0.51 [14]	-5.5 ± 0.1	66.8 ± 1	-4.6 ± 0.1	-166 ± 5
Pt	-0.33 [14]	-3.17 ± 0.03	112 ± 5	-3.34 ± 0.02	-127 ± 13
Pd	-0.38 [14]	-4.4 ± 0.1	198 ± 9	-4.2 ± 0.1	-168 ± 12
Rh	-0.34 [14]	--	--	-3.72 ± 0.02	-69.3 ± 3
W	-0.67 [14]	-7.96 ± 0.04	76.1 ± 0.4	--	--

Table 3.12 summarizes the kinetic data obtained for the disk and supported electrodes found in this chapter. Since there was a strong agreement between the Butler-Volmer and Tafel methods for calculating exchange current densities, only the activities calculated from the Tafel method were listed here for consistency. Also listed are the hydrogen binding energies taken from Reference [14] and [16]. These hydrogen binding energies were calculated using a coverage fraction of 0.25, but the trends remain intact when using binding energies calculated using a higher coverage of hydrogen.[14]

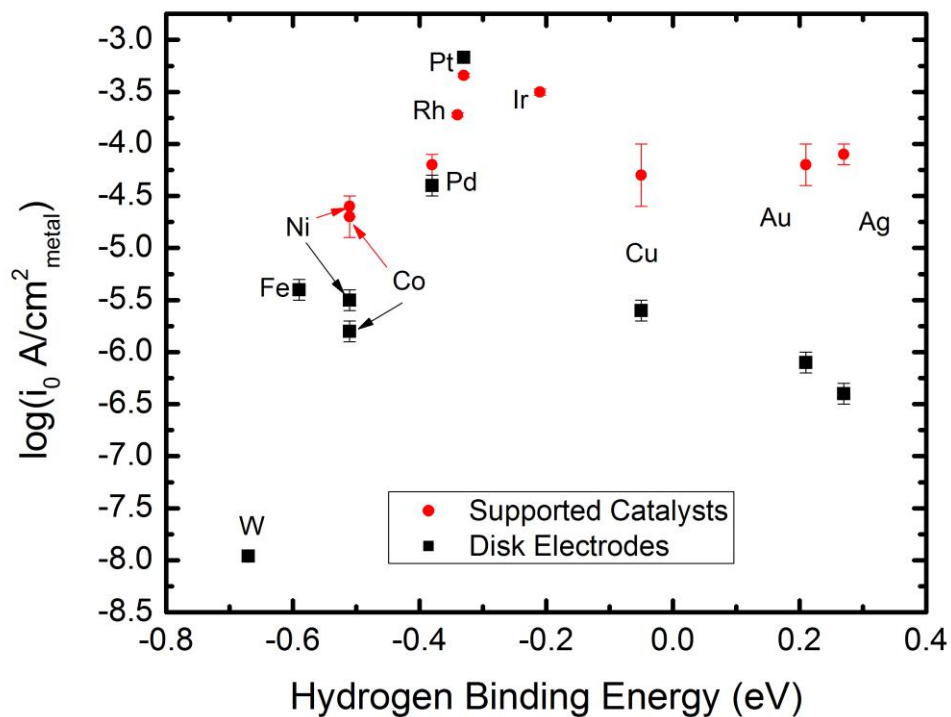


Figure 3.22: Volcano plot of monometallic disk and supported electrodes.

By plotting the exchange current densities of the disk and supported electrodes against the hydrogen binding energy values taken from literature, a volcano plot is obtained for the HOR/HER in alkaline conditions (Figure 3.22). The Pt disk and Pt/C electrodes show the highest activity for the HOR/HER in 0.1 M KOH. Surfaces that bind energy more strongly than Pt (Rh, Pd, Co, Ni, Fe, and W) fall to the left side of the volcano curve, while surfaces that bind hydrogen more weakly than Pt (Ir, Cu, Au,

Ag) fall to the right side. The Pt disk and Pt/C electrodes achieve the highest current density because Pt has an intermediate hydrogen binding energy, resulting in a high activity due to the competition between the adsorption and desorption of  $H_{ad}$  in the HOR/HER mechanism discussed in Chapter 1.3.

The supported catalysts follow the same trends as the disk electrodes, with Pt/C being the most active. However, some of the supported catalysts are orders of magnitude more active than the corresponding disk electrodes. This is especially apparent for Cu/C, Au/C, and Ag/C, which have activities on the order of Pd/C. Pt/C and Pd/C have activities much closer to the Pt and Pd disk, respectively. Ni/C and Co/C also have higher activities than the Ni and Co disk, respectively.

The reason for the apparent increase in activity with decreasing in particle size is not obvious from the kinetic data alone. It was suggested by Strmcnik et. al. that the HOR mechanism requires OH adsorbed on the catalyst surface in order to oxidize  $H_{ad}$ , and therefore the HOR/HER activity was shown to be higher than Pt on more oxophilic surfaces such as Ir and PtRu.[41] On Pt surfaces, where the Pt-OH species does not form until 0.6 V vs. RHE,  $OH_{ad}$  was hypothesized to form on defect sites at lower potentials. However, Sheng et. al. proved that the hydrogen binding energy alone was sufficient to predict the HOR/HER activity on Pt in electrolytes with varying pH, which disproves the  $OH_{ad}$  theory for the Pt surface.[46] The present work shows that Ir/C is less active than Pt/C, which is in direct opposition to the results and predictions of Strmcnik et. al. In fact, the increased oxophilicity of Ir in the HOR/HER regime is responsible for a decrease in the HOR current.[18] The increase in activity for the PtRu surface was also attributed to a shift in hydrogen binding energy on Pt due to the neighboring Ru atoms, rather than the promotion of  $OH_{ad}$  on the Ru

sites.[48] Overall, a large amount of evidence has been found against the hypothesis that  $\text{OH}_{\text{ad}}$  is an active species for HOR in alkaline conditions for Pt group metals. Instead, the activity seems to be dominated by hydrogen interactions with the catalytic surface.

Little work has been conducted on other catalysts concerning the mechanism of HOR/HER. Following the conclusions drawn for Pt group metals, it is possible that the hydrogen binding energy on nanoparticles is shifted toward more intermediate values, which would account for the large increase in activity. Small Au nanoparticles have been shown to have altered electronic states compared to bulk Au surfaces.[49] However, a large increase in activity on Au nanoparticle catalysts is noticed in many other oxidation reactions, including the electrooxidation of CO.[50,51] In the case of CO electrooxidation, the increase in activity on smaller particles is due to the increased interaction of Au with OH species in the alkaline electrolyte. If a similar case holds for HOR in alkaline conditions, then the  $\text{OH}_{\text{ad}}$  hypothesis may hold for the supported Au/C catalyst.

Similarly, Ag/C nanoparticles and high surface area Ag catalysts were found to have a large increase in activity toward the electroreduction of carbon dioxide over polycrystalline Ag surfaces due to the presence of more step sites.[27] The difference in Tafel slopes calculated for the Ag/C compared to the Ag disk in the present study also indicates that the HOR/HER most likely undergo a different mechanism on Ag/C than on the Ag disk. If the large increase in the HOR/HER activity on Ag/C were only due to shifts in hydrogen binding energy, the Tafel slope would not have been expected to change. Therefore, the possibility of an active  $\text{OH}_{\text{ad}}$  species on Au/C and Ag/C cannot be ruled out completely.

In conclusion, an existing volcano relationship for the alkaline HOR/HER was extended to include supported monometallic catalysts. The same general trends still hold; Pt/C remains the most active catalyst and the hydrogen binding energy is still a good thermodynamic descriptor. However, large increases in activity were measured for supported Au/C and Ag/C over their respective polycrystalline disk electrodes, which may be due to a change in mechanism on the nanoparticle surfaces.

## Chapter 4

### PLATINUM-MODIFIED GOLD ELECTROCATALYSTS FOR THE ALKALINE HYDROGEN OXIDATION REACTION

According to the volcano plot established for monometallic supported catalysts, Pt is still the most active metal for the alkaline HOR. To reduce the cost of HOR catalysts for HEMFCs, either another metal must be modified to yield an increased activity comparable to Pt, or the amount of Pt needed for HOR must be decreased. Ni alloys have been shown to be as active as Pt, and may offer a less expensive alternative to a Pt-based anode.[52] However, the mechanism of HOR on these surfaces is not as well-established as that on Pt. Therefore, Pt-based catalysts are still of interest.

To reduce the total amount of Pt needed for the HOR in an HEMFC, surfaces modified with monolayer amounts of Pt may be used. These types of Pt-modified electrocatalysts have been used to decrease the amount of Pt needed for the oxygen reduction reaction (ORR)[53–55] and hydrogen evolution reaction (HER)[56–58] in acidic environments. In previous studies, these catalysts have been referred to as Pt monolayers, though recent XAS studies have confirmed that Pt deposited in this manner manifests itself as small nanostructures on the substrate.[59] Scanning tunneling micrographs of Pt/Au samples prepared using this method also show small Pt nanostructures on the Au surface.[60] Though the total amount of Pt needed in these studies was greatly reduced, the Pt-modified catalysts retained catalytic activity similar to that of bulk Pt.

The current study examines the feasibility of the same Pt modification approach to HOR catalysts in alkaline electrolytes. Gold (Au) was chosen as a substrate due to its low HOR activity in alkaline electrolytes. HOR kinetic data in 0.1 M KOH were obtained on Au, Pt, and Pt-modified Au (Pt/Au) bulk disk electrodes (denoted as Au disk, Pt disk, and Pt/Au disk). While disk electrode studies are useful for determining trends on well-defined surfaces, supported catalysts are commercially viable. Therefore, the corresponding supported catalysts (denoted as Au/C, Pt/C, and Pt/Au/C) were also tested for activity toward the HOR. Pt/C thin film electrodes were prepared using 46 wt% Pt/C, following a previous study.[9] The Pt/C ink was prepared by dispersing ~0.15 mg/mL catalyst in deionized water via sonication. 20  $\mu\text{L}$  of the ink were deposited on a glassy carbon electrode and allowed to dry in air at room temperature, resulting in a Pt loading of  $\sim 7 \mu\text{g}_{\text{Pt}}/\text{cm}^2$ . Au/C thin film electrodes were prepared using 40 wt% Au/C. The Au/C ink was prepared by dispersing ~1.6 mg/mL in a solution of 50% isopropanol and 50% deionized water via sonication. 10  $\mu\text{L}$  of the ink were deposited on a glassy carbon electrode and allowed to dry in air at room temperature, resulting in a Au loading of  $\sim 33 \mu\text{g}_{\text{Au}}/\text{cm}^2$ . The Pt/Au/C electrodes were prepared using the same Au/C electrodes. This is the first time Pt/Au catalysts have been evaluated for HOR/HER in alkaline electrolytes.

#### **4.1 Synthesis of Cu/Au via Cu Underpotential Deposition**

Pt/Au catalysts were synthesized on Au through the galvanic displacement of a monolayer of copper (Cu).[20,21] Therefore, the behavior of the Cu underpotential deposition (UPD) process is vital in understanding the structure of the final Pt/Au surface. The ideal case of Cu UPD is illustrated in Figure 4.1. Cu UPD occurs because Au-Cu interactions are more favorable than bulk Cu-Cu interactions at certain

potentials. Above these potentials, Cu deposits on Au in bulk. Therefore, by controlling the potential of the system, Cu monolayers can be selectively grown.

Comparing CVs of the bare Au disk with and without  $\text{Cu}^{2+}$  ions present allows the analysis of the Cu monolayer (Figure 4.2). The polycrystalline Au disk CV in 0.05 M  $\text{H}_2\text{SO}_4$  without  $\text{Cu}^{2+}$  ions present (Figure 4.2a) is similar to those reported in literature.[61] In the cathodic scan, oxygen containing species do not adsorb to the surface until 1.30 V, where two oxidation peaks are clearly seen at 1.40 and 1.60 V. Comparison to single-crystalline Au CV data shows that the first oxidation peak at 1.4 V is apparent on the Au(111), Au(100), and Au(110) facets, but that the peak at 1.60 V is only indicative of Au(111).[62] This oxide layer is then reduced in the anodic scan, where there is one large reduction peak at 1.15 V. The area under the reduction peak can be integrated to find the active surface area of the electrode. As suggested in the so-called Burshtein minimum method, the upper potential limit of the CV used to calculate the surface area should correspond to the minimum cathodic current before oxygen evolution.[30,31] For this electrode, that potential was found to be  $\sim 1.65$  V. Using this upper potential limit ensures that one monolayer of oxide is formed, for which the charge density associated with reducing has been estimated to be  $390 \mu\text{C}/\text{cm}^2$  for polycrystalline Au electrodes.[32] Using this method, the Au roughness factor was calculated to be 1.37.

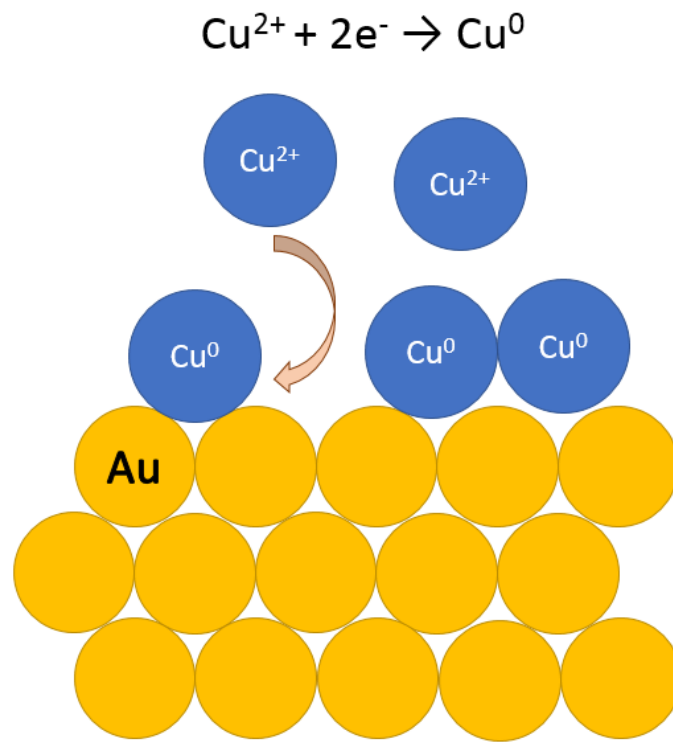


Figure 4.1: Cu underpotential deposition on an Au substrate.

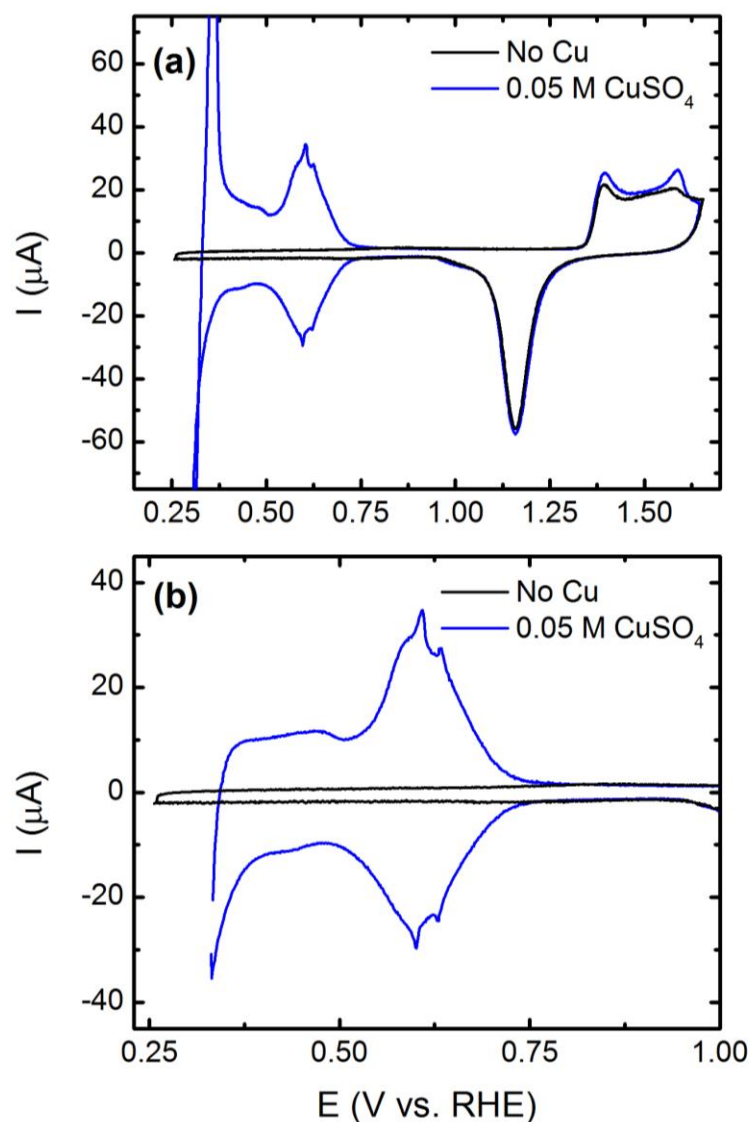


Figure 4.2: CVs of the Au disk in 0.05 M  $\text{H}_2\text{SO}_4$  with and without 0.05 M  $\text{CuSO}_4$ . Potential limits were chosen to show (a) Cu bulk deposition and UPD as well as (b) Cu UPD only.

In the presence of  $\text{Cu}^{2+}$  ions, the Au surface oxide formation and reduction behavior does not change significantly, suggesting that Cu deposition does not irreversibly change the Au substrate surface (Figure 4.2a). At 0.3 V, there is a large

anodic and cathodic current associated with the bulk deposition and removal of Cu. However, above  $\sim 0.4$  V, Cu UPD is evident. By limiting the lower potential limit of the CV, bulk Cu deposition can be avoided, resulting in only one layer of Cu deposited on the Au surface (Figure 4.2b). This CV shows two broad peaks in the anodic and cathodic scans occurring between 0.50 and 0.75 V. Two sharper peaks are observable at 0.60 and 0.63V. Au(111), Au(100), and Au(110) all show Cu UPD peaks in this potential range.[63] However, Cu UPD on Au(111) occurs in two steps, which results in the appearance of an additional Cu UPD peak at approximately 0.40 V.[64] A distinct UPD peak was not found for the Au disk in that potential range, but a broad feature is observed, indicating that the second step of Cu UPD may occur to a small extent.

The fact that the additional Cu UPD deposition peak is missing is essential when estimating the structure and coverage of the deposited Cu. Detailed scanning tunneling microscopy experiments of Cu UPD adlayers on single-crystalline Au(111) surfaces indicate that at  $\sim 0.50$  V, the honeycomb Cu adlayer structure has a coverage of  $2/3$ .[65] On Au(111), a full monolayer of Cu is not deposited until the potential is lowered beyond  $\sim 0.40$  V. Other studies of Pt/Au catalysts synthesized using sacrificial Cu UPD adlayers claim that the maximum coverage of Cu can only be 66% because of the Cu UPD behavior on Au(111).[66,67] The Cu UPD CVs shown in Figure 4.1 indicate that the second Cu deposition step on Au(111) does not occur on the polycrystalline Au electrode, which supports the hypothesis that there is not a full coverage of Cu deposited onto the Au substrate.

However, assuming the charge density associated with the monolayer deposition of divalent ions is  $400 \mu\text{C}/\text{cm}^2$ , [68] the integration of the cathodic Cu UPD

peak yields a roughness factor of 1.32, which suggests that there is over a 66% coverage of Cu. Literature suggests that the 66% coverage honeycomb Cu structure is unstable in certain conditions, specifically in the presence of  $\text{Cl}^-$  ions.[65,69] The use of a Ag/AgCl reference electrode may render the honeycomb Cu adlayer unstable, resulting in a higher coverage of the Au electrode with Cu.

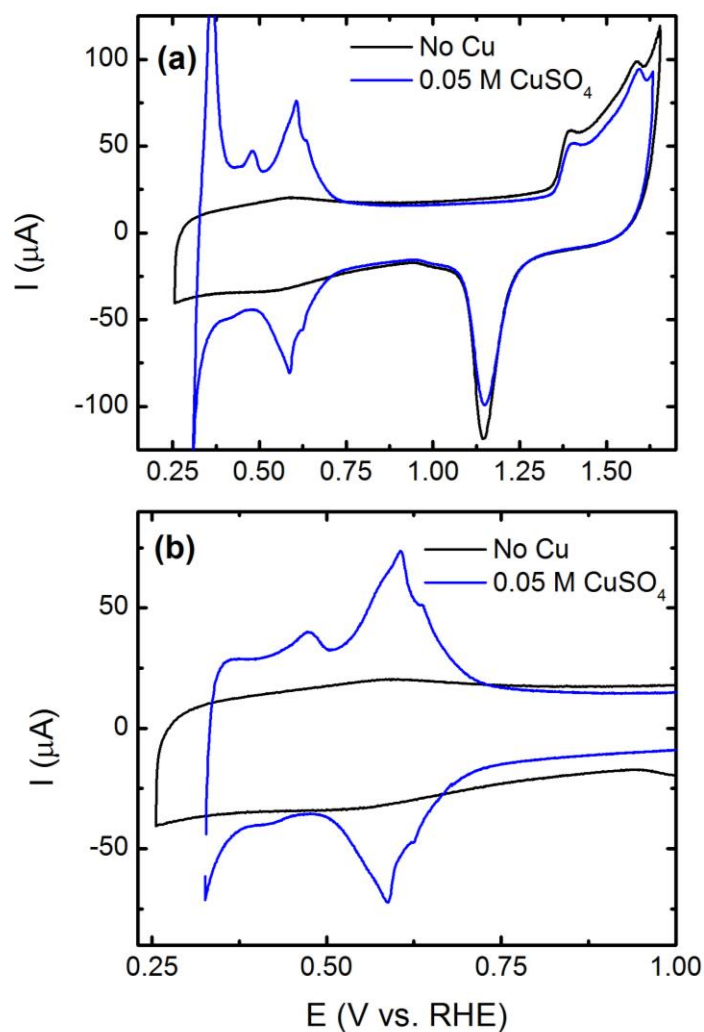


Figure 4.3: CVs of the 40% Au/C electrode in 0.05 M  $\text{H}_2\text{SO}_4$  with and without 0.05 M  $\text{CuSO}_4$ . Potential limits were chosen to show (a) Cu bulk deposition and UPD as well as (b) Cu UPD only.

The CV of Au/C contains the same main features as the Au disk (Figure 4.3a), specifically the formation and reduction of Au oxides above  $\sim 1.0$  V. The double layer current for the supported catalyst is greater than the Au disk, likely due to the higher surface area of Au present as well as the carbon support. Additionally, the Burshtein minimum for Au/C is more difficult to determine. The same upper potential limit as the Au disk was used for the determination of the active Au/C surface area, which resulted in a calculated roughness factor of 2.10.

The Cu UPD behavior on Au/C is also similar to the Au disk (Figure 4.3b). The distinct UPD peaks at 0.60 and 0.63V remain evident of Au/C. However, the appearance of an additional UPD peak at  $\sim 0.45$ V suggests that the behavior of Cu UPD on Au nanoparticles is somewhat different than on the disk. Specifically, this peak corresponds to the second step of the Cu monolayer discussed above, which may indicate a higher coverage of Cu deposited on the Au/C than on the Au disk. The charge associated with the Cu UPD process yields a roughness factor of 2.19 for the electrode shown in Figure 4.3, which also agrees with the roughness factor calculated for the Au/C substrate.

While the Cu UPD behavior is important in understanding the integrity and coverage of the final Pt/Au surface, the Cu/Au surface itself is difficult to characterize due to the oxidation of Cu upon exposure to air. Therefore, the majority of characterization must be completed on the Pt/Au surface.

## **4.2 Characterization of Pt, Au, and Pt/Au Surfaces**

After the Cu UPD process, the electrode is transferred to a deaerated platinum precursor, where the Cu monolayer is ideally completely displaced by metallic platinum. However, the realistic nature of the Pt overlayer is unknown. Therefore,

further characterization beyond the observance of Cu UPD behavior is required. Both electrochemical and traditional techniques were used to determine the structure of the Pt on the Au disk and Au/C substrates.

#### 4.2.1 TEM

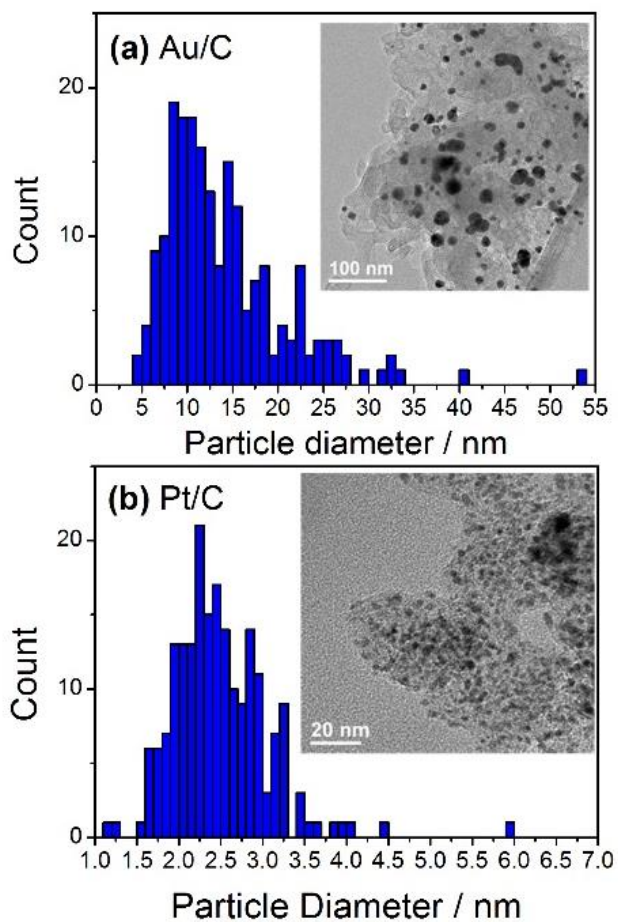


Figure 4.4: Particle size distributions and transmission electron micrographs (inset) of (a) Au/C and (b) Pt/C. The Pt particles and Au particles are approximately  $2.5 \pm 0.6$  nm and  $14 \pm 6.9$  nm in diameter, respectively.

TEM was used to assess the size of the Pt and Au particles in the supported catalysts (Figure 4.4). The Pt and Au particles are  $2.5 \pm 0.6$  nm and  $14 \pm 6.9$  nm in diameter, respectively, based on averaging 200 particles. The resolution of the TEM used was not strong enough to detect the Pt on the Pt/Au/C samples. The relatively large size of the Au particles suggests that Au/C may exhibit similar properties to the Au disk. Previous studies of Pt-modified Au on smaller nanoparticle Au substrates ( $< 3$  nm) for ORR in acidic electrolytes indicate that the additional compressive strain on the surface of the Au nanoparticles causes the Pt/Au behavior to deviate significantly from that of the Pt/Au deposited on single crystal Au substrates.[21] However, since the Au particles used in this study are much larger than 3 nm, the particles are assumed to behave more similarly to bulk Au.

#### 4.2.2 XPS

The XPS spectra of the Pt/Au disk immediately after galvanic displacement of the Cu UPD ML with Pt is shown in Figure 4.5. The detection of the Pt 4f features indicates the presence of Pt on the Au surface. In addition to metallic Pt, which is characterized by peaks at approximately 74 and 71 eV, peaks at  $\sim 78$  and 75 eV indicate the presence of Pt<sup>4+</sup> on the surface. This has been attributed to the fact that the galvanic displacement of Cu with Pt does not form an entirely reduced Pt overlayer on Au substrates for Pt overlayers under 2 monolayers in thickness.[70] Pt<sup>2+</sup> may also be present, but no peaks distinct from Pt<sup>0</sup> or Pt<sup>4+</sup> can be clearly observed.

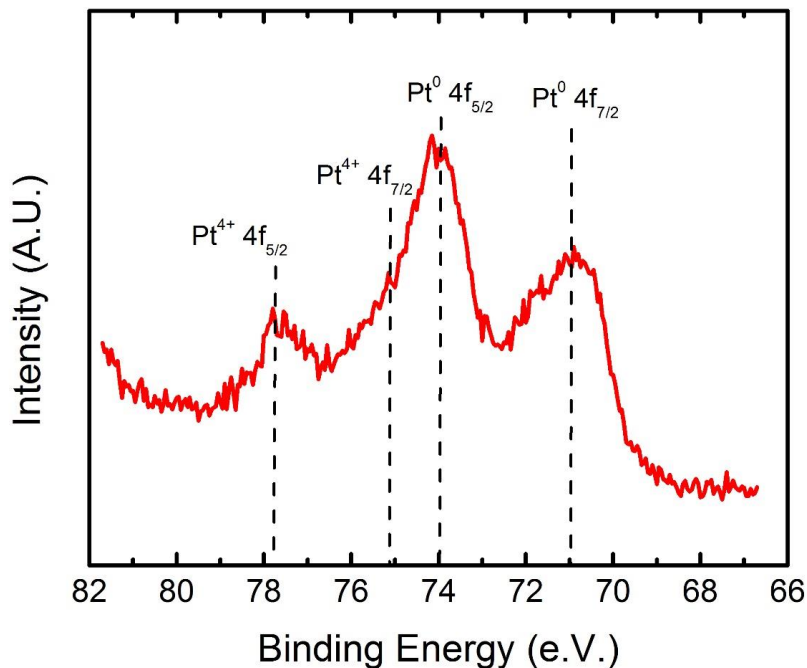


Figure 4.5: Pt 4f XPS spectra of the Pt/Au disk. Both Pt<sup>0</sup> and Pt<sup>4+</sup> species are observed, as marked by vertical dashed lines.

### 4.2.3 Cyclic Voltammetry

To confirm the presence of Pt on the surface of Au, the CVs of Au, Pt, and Pt/Au disk electrodes were compared in alkaline electrolytes (Figure 4.6a). The Au CV shows a hydroxyl adsorption peak at 1.2 V, but does not show hydrogen adsorption/desorption that is typical on Pt surfaces.[29,62] The Pt CV shows features characteristic of the hydrogen underpotential deposition (H-UPD) region on Pt(110) and Pt(100) at 0.3 V and 0.4 V, respectively, followed by the onset of the hydroxyl adsorption at above 0.6 V.[43] The presence of bulk Pt features in the CV of the Pt/Au disk confirms the presence of Pt on the Au substrate. The same trends follow for the Au/C, Pt/C, and Pt/Au/C supported electrodes (Fig. 1b).

In the CVs for both the Pt/Au disk and Pt/Au/C, the formation and reduction of Au oxides are visible, indicating that there is not a full coverage of Pt on the Au disk. Additionally, the reduction of the Pt in the Pt/Au sample occurs approximately 0.1 V lower than the reduction of the Pt disk. Similarly, the reduction of Pt on Pt/Au/C occurs at a lower potential than for Pt/C (Figure 4.6b), though the difference in reduction potentials is lower than the disk electrodes. This discrepancy in reduction potentials has been observed for Pt/Au surfaces in acidic media, where thinner Pt overlayers result in a lower reduction potential.[70] Since Pt forms small nanoislands on the Au surface instead of a fully developed epitaxial monolayer,[60,71] some amount of Au substrate is expected to be left uncovered. However, the AuO reduction peak in the Pt/Au/C CV is much smaller than the AuO reduction peak in the Pt/Au disk CV, suggesting that the coverage of Pt is higher for Pt/Au/C than the Pt/Au disk.

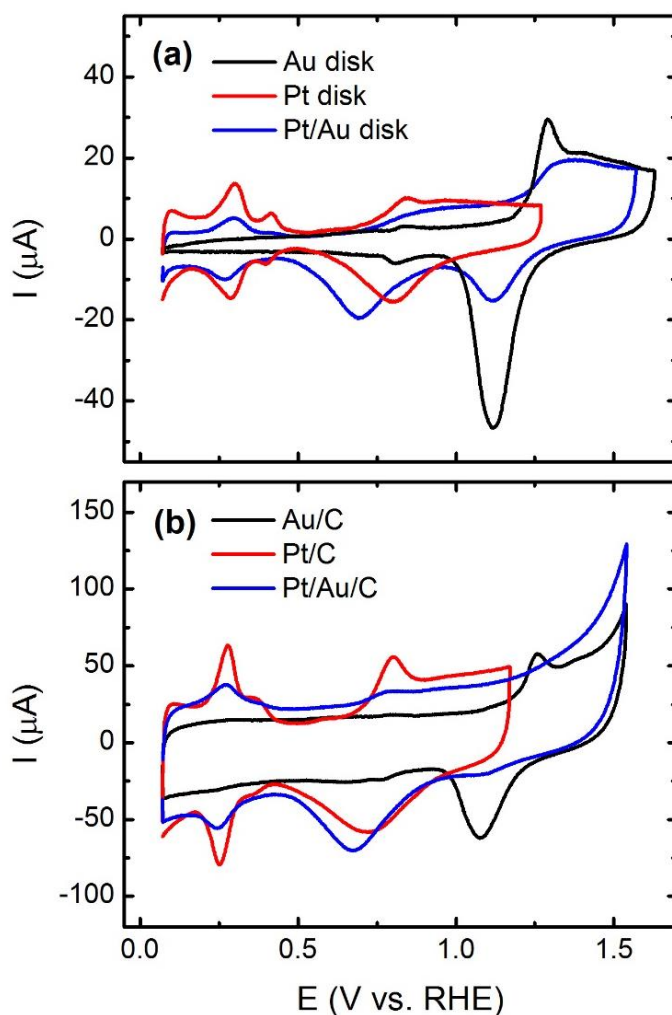


Figure 4.6: Cyclic voltammograms (CVs) of (a) disk electrodes and (b) supported catalysts on glassy carbon electrodes in Ar-purged 0.1 M KOH. The CVs for Au samples and Pt samples are taken at 100 mV/s and 50 mV/s, respectively.

#### 4.2.4 Determination of Electrochemically Active Surface Area

For the subsequent HOR kinetic analyses, the actual electrochemical surface areas (ECSA) are needed. Two methods were used to measure the surface area. The first method involves calculating the charge associated with certain voltammetric

features in the CVs of each electrode. The second method utilizes CO stripping on the Pt and Pt/Au surfaces.

#### **4.2.4.1 Pt H-UPD and AuO Integration**

The first method involves calculating the charge associated with the H-UPD region on Pt or the monolayer AuO formation on Au (Figure 4.6). For the Pt and Pt/Au samples, the H-UPD area is found by integrating the hydrogen adsorption and desorption peaks between 0.05 V and 0.5 V vs. RHE after subtracting the double layer current, then dividing by 2 and  $210 \mu\text{C}/\text{cm}^2_{\text{Pt}}$ . [44] Similarly, the surface area of Au can be calculated by integrating the peak corresponding to the reduction of AuO at approximately 1.05 V vs. RHE, normalized by a charge density of  $390 \mu\text{C}/\text{cm}^2_{\text{Au}}$ . [32]

#### **4.2.4.2 CO Stripping**

The second method measures the charge associated with the desorption of one monolayer of carbon monoxide (CO) on a Pt surface. This method is known as CO stripping and is only applicable to the Pt and Pt /Au samples. The background, CO-free current is subtracted from the CO desorption current and normalized by a charge density of  $420 \mu\text{C}/\text{cm}^2_{\text{Pt}}$ . [72]

The Au disk shows a small CO oxidation peak at 0.5 V that is attributed to CO adsorption on Au(111) (Figure 4.7a). [73] The Au/C catalyst also shows the Au(111) peak (Figure 4.8a). The charge from these peaks are a negligible contribution to the overall Pt /Au CO stripping curves. No surface area determinations can be made from this peak.

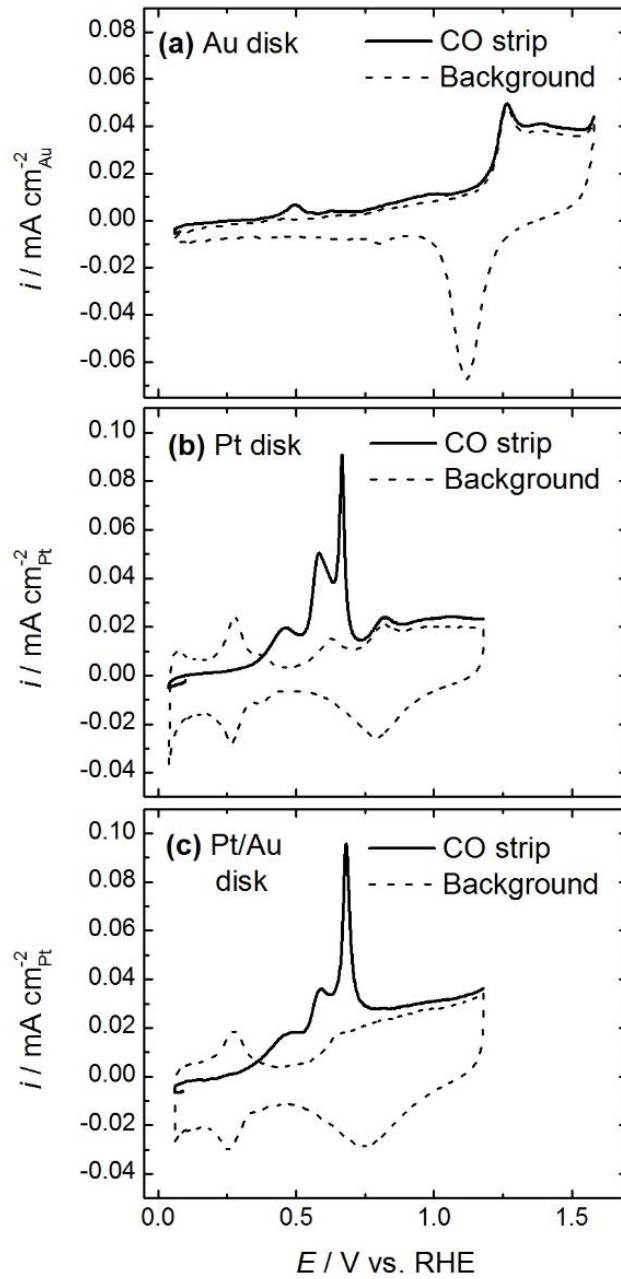


Figure 4.7: CO stripping and background curves for the (a) Au, (b) Pt, and (c) Pt/Au disks. Each was obtained at 20 mV/s in 0.1 M KOH. The Pt/Au sample shows similar CO stripping characteristics to bulk Pt.

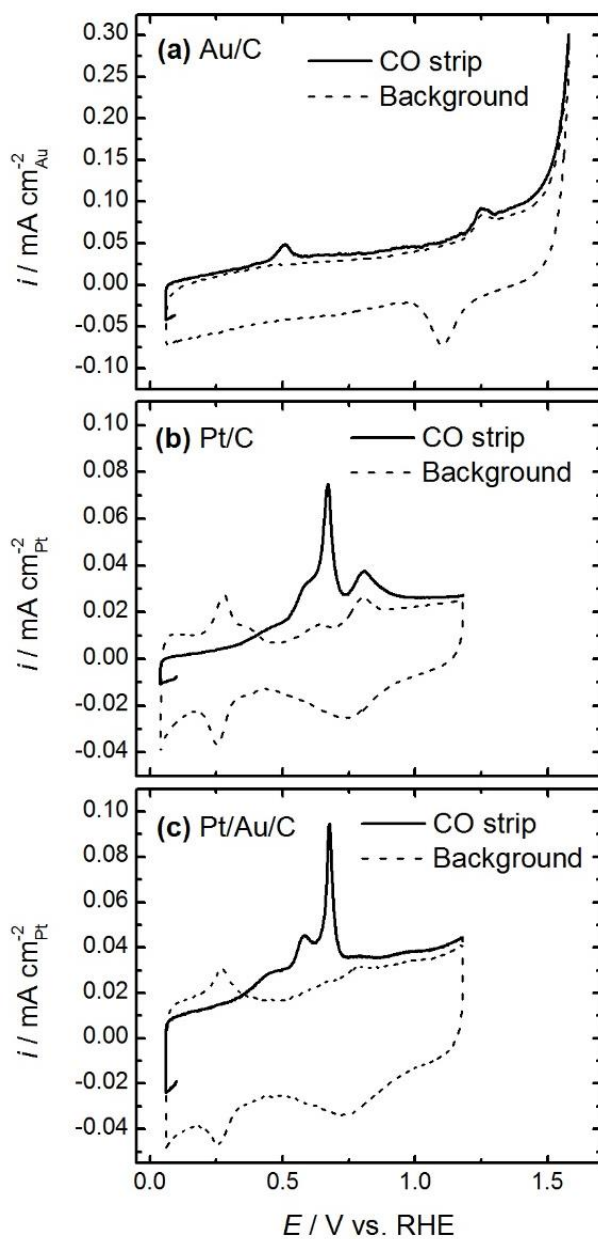


Figure 4.8: CO stripping and background curves for (a) Au/C, (b) Pt/C, and (c) Pt/Au/C. Each was obtained at 20 mV/s in 0.1 M KOH. The Pt/Au/C sample has more defined CO stripping characteristics than Pt/C.

The CO stripping voltammograms on Pt surfaces in alkaline media have been well studied.[23,74–76] CO is primarily oxidized by OH adsorbed on the edge and defect sites of Pt. The CO stripping voltammogram in alkaline conditions contains well defined, structure sensitive peaks, which have been attributed to low CO mobility and formation of carbonate on the surface.[77] These peaks are apparent on the Pt disk electrode (Figure 4.7b). The Pt disk CO stripping curve can be analyzed using data from single crystalline studies.[77–79] The onset of CO oxidation current at 0.4 V, commonly called the "prewave," is due to defect sites on the Pt surface. The peaks at ~0.6 V and ~0.7 V for the Pt disk are due to CO oxidation at Pt(110) step and Pt(100) step sites, respectively.

Studies of alkaline CO stripping on shape-controlled Pt particles show a dependence of particle structure on the main CO stripping peaks.[22,80] Spherical particles sized 4-5 nm in these studies are shown to behave similarly to polycrystalline Pt for CO stripping in alkaline media. While the Pt/C CO voltammograms do resemble the bulk Pt disk in our study (Figure 4.8b), the Pt/C voltammogram has a less defined prewave and defect site signature than the polycrystalline Pt disk. CO stripping peak broadening is observed for small Pt particles in acidic conditions, with the broadening becoming more apparent for smaller particles.[74,81] Considering the small size of the Pt/C particles used (~2.5 nm), the lack of peak definition for Pt/C may be attributed to this peak broadening.

The Pt/Au disk (Figure 4.7c) and Pt/Au/C (Figure 4.8c) have CO stripping voltammograms similar to the Pt disk, including the prewave as well as the Pt(110) and Pt(100) peaks. The CO stripping features of both the disk and supported Pt/Au samples closely resemble those of cubic Pt particles.[22] This supports the claim that

Pt does not form a true monolayer on the Au substrate, but instead aggregates to form nanostructures on the surface. A previous study shows that a true Pt monolayer on Rh(111) deposited in ultra high vacuum conditions behaves differently than a Pt monolayer synthesized by galvanic displacement.[59] In essence, the galvanic displacement method does not ensure a full Pt monolayer on the Rh(111) surface, but instead produces nanostructured Pt islands. The CO stripping results presented here conclude that this is also the case for Pt deposited on Au substrates via galvanic displacement.

#### 4.2.4.3 Comparison of Voltametric and CO Stripping Techniques for Pt/Au

The calculated surface area values from both methods are divided by the area of the electrode ( $0.196 \text{ cm}^2$ ) to give a roughness factor or by the mass of catalyst to give a specific area (Table 4.1).

Table 4.1: Calculated roughness factors and electrochemical surface areas for Au, Pt and Pt/Au catalysts.

Electrode	Roughness Factor ( $\text{cm}^2_{\text{metal}}/\text{cm}^2_{\text{disk}}$ )		Specific Area ( $\text{m}^2/\text{g}_{\text{metal}}$ )	
	H-UPD/AuO	CO Stripping	H-UPD/AuO	CO Stripping
Au disk	$1.18 \pm 0.02$	--	--	--
Pt disk	$1.34 \pm 0.04$	$1.2 \pm 0.1$	--	--
Pt/Au disk	$0.7 \pm 0.2$	$1.2 \pm 0.2$	--	--
Au/C	$1.9 \pm 0.1$	--	$5.8 \pm 0.3$	--
Pt/C	$3.5 \pm 0.5$	$3.5 \pm 0.3$	$50 \pm 7$	$50 \pm 4$
Pt/Au/C	$1.35 \pm 0.01$	$1.8 \pm 0.1$	$4.09 \pm 0.03^*$	$5.5 \pm 0.3^*$

\*Normalized by the total mass of Pt and Au

The roughness factors of the Au and Pt disks are close to 1, which indicates that the disk electrodes are smooth. For Pt, the roughness factors calculated from both

the H-UPD and CO stripping are similar, indicating that the two methods are comparable on the Pt surface. For the supported catalysts, the roughness factors depend on the particle size and loading. The roughness factor is 1.8 for Au/C and 3.3 for Pt/C. Similar roughness factors are calculated from both methods for Pt/C, though error for the H-UPD method is larger than for the CO stripping method.

While H-UPD and CO stripping agree for the roughness factors of Pt and Pt/C, there is a discrepancy between the two methods for the Pt/Au disk and Pt/Au/C. The H-UPD-calculated roughness factor is significantly lower than the value calculated by CO stripping for both Pt/Au and Pt/Au/C. Using the H-UPD-obtained roughness factors, a Pt coverage of ~60 - 70% is calculated for both the Pt/Au and Pt/Au/C samples, while the CO stripping roughness factors show a Pt coverage of ~90 - 100%.

This discrepancy may be a consequence of the nanostructuring of the Pt on the Au surface. For pure Pt nanoparticles less than 3 nm in diameter, the surface area calculated by the H-UPD area has been shown to be less than the area calculated by CO stripping.[81] It was therefore recommended to use the CO stripping surface area for small Pt particles to avoid error from the H-UPD suppression. The nanostructured Pt particles would experience H-UPD suppression resulting in a decreased calculated surface area.

It has also been shown that the coverage of CO on Pt surfaces can change depending on the surface structure in both acidic[82] and alkaline[83–85] media. For instance, the packing density of CO on a Pt(111) surface can change with the addition of steps on the surface.[82] Additionally, the adsorption configuration of CO on Pt(110) step sites is primarily linear, while CO on Pt(100) step sites can be in the linear and bridge configuration.[85] However, infrared studies indicated that only a

very small fraction of CO molecules in the adsorbed monolayer are in the bridge configuration.[86] Alternatively, it is also possible that the interchange of Pt and Au atoms on the surface may change the amount of Pt area calculated.[87] The presence of adsorbed hydrogen and CO has been shown to not change the composition of the bimetallic surface.[88,89]

### **4.3 HER/HOR Activity of Pt/Au and Pt/Au/C**

The exchange current density for the Au samples was found by extrapolating the linear portion of the Tafel plot (between approximately  $-1 \text{ mA/cm}^2_{\text{disk}}$  and  $-5 \text{ mA/cm}^2_{\text{disk}}$ ) to 0 V vs. RHE. Both Pt/Au and bulk Pt samples reach the theoretical hydrogen mass transport controlled current density for 1600 rpm (Figure 4.7a). The Pt/Au kinetic current density fits the Butler-Volmer equation very well (Figure 4.7c). From this fit, the transfer coefficient ( $\alpha$ ) and exchange current density ( $i_0$ ) were obtained (Table 4.2). Pt/Au exhibits activity similar to bulk Pt and far higher activity than bulk Au, though the discrepancy in roughness factors also causes a corresponding discrepancy in the HOR/HER exchange current density. The activity utilizing the CO stripping roughness factor is used to compare between samples.

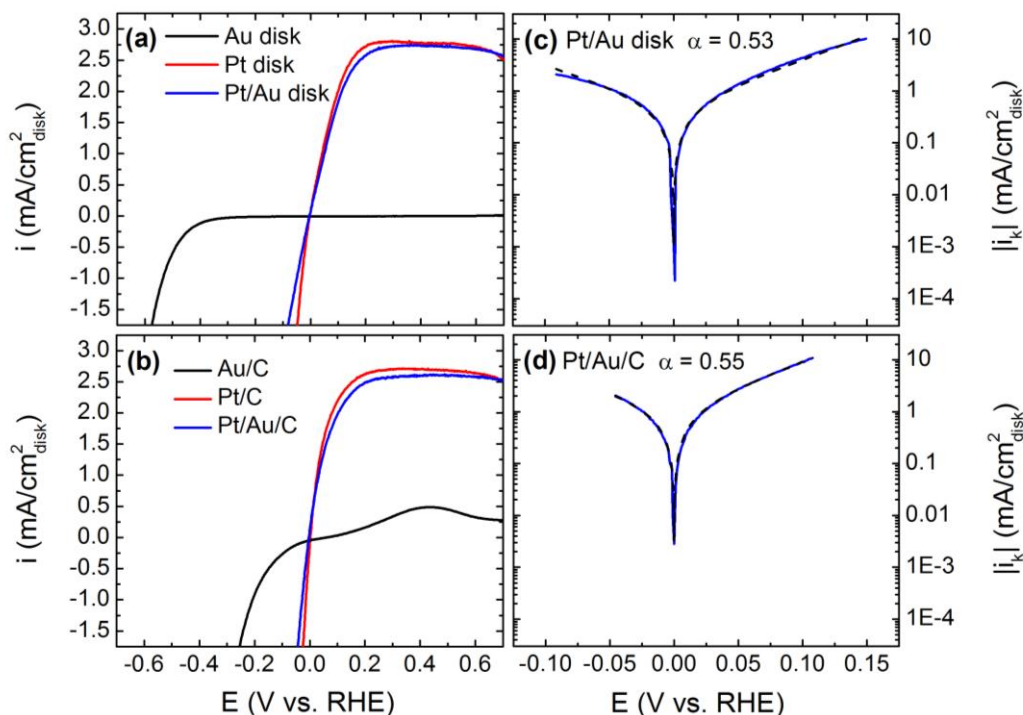


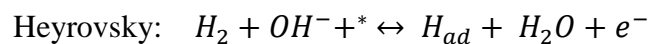
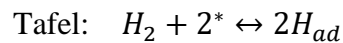
Figure 4.7:  $iR$ -corrected polarization curves of HER/HOR on (a) Au disk, Pt disk, Pt/Au disk, (b) Au/C, Pt/C, and Pt/Au/C in  $H_2$  saturated 0.1 M KOH. Kinetic current of HER/HOR on (c) the Pt/Au disk electrode and (d) Pt/Au/C (solid blue line) and their fit to the Butler-Volmer equation (dashed black line). The bulk Pt samples and Pt/Au samples exhibit similar activity and are both superior to the Au samples. Au/C shows higher activity than bulk Au. Both Pt/Au and Pt/Au/C show excellent fit to the Butler-Volmer equation.

Table 4.2: The HER/HOR exchange current densities for each electrode in 0.1 M KOH, normalized by the electrochemical surface area for each metal.

Electrode	$\log(i_0 [A/cm^2_{\text{metal}}])$		Transfer Coefficient ( $\alpha$ )
	H-UPD/AuO	CO stripping	
Au disk	$-5.23 \pm 0.01$	--	--
Pt disk	$-3.18 \pm 0.01$	$-3.13 \pm 0.04$	0.50
Pt/Au disk	$-3.1 \pm 0.1$	$-3.4 \pm 0.1$	0.53
Au/C	$-4.35 \pm 0.02$	--	--
Pt/C	$-3.32 \pm 0.06$	$-3.32 \pm 0.04$	0.50
Pt/Au/C	$-3.130 \pm 0.003$	$-3.26 \pm 0.02$	0.55

The HER/HOR kinetics of the supported Pt/C, Au/C and Pt/Au/C catalysts were analyzed in the same fashion as the bulk disk electrodes. The iR-corrected polarization curves of the supported catalysts at 1600rpm exhibit similar trends as the bulk electrodes (Figure 4.7b). The Pt/Au/C kinetics current density also fits the Butler-Volmer equation (Figure 4.7d). Pt/Au/C exhibits equivalent activity as bulk Pt (Table 4.2). The Au/C particles show an increase in activity over the bulk Au disk electrode. Considering the large size of the Au particles, it is expected that they would behave more like the bulk Au disk. However, Au is known to exhibit unusual size- and support-dependant behavior in a number of other electrocatalytic systems that are not discussed here.

Under alkaline conditions, the mechanism of HOR proceeds through a combination of two of the following steps:[13]



where \* represents an empty catalytic site. The mechanism is dependant on adsorbed hydrogen ( $H_{ad}$ ) in all steps, which is thermodynamically dictated by the hydrogen binding energy (HBE). In acidic conditions, the HBE has been shown to produce a volcano relationship with hydrogen oxidation and evolution activity.[14]

In alkaline conditions, a volcano relationship has also been established between the hydrogen evolution reaction activity and the HBE,[15] but the

catalytically active form of  $\text{OH}^-$  is not specified in the mechanism. Recently, Strmcnik et al. hypothesized that  $\text{OH}_{\text{ad}}$  is the catalytically active species for the alkaline HOR.[41] However, Durst et al. suggest  $\text{OH}_{\text{ad}}$  plays no role in alkaline HOR and the decrease in HOR activity is due to stronger hydrogen binding energies in base compared to acid.[90] Sheng et. al. also proved that the activity of Pt for HOR/HER is directly correlated to the hydrogen binding energy. [46] Pt/Au samples likely undergo HOR through the same mechanism as bulk Pt because the transfer coefficients are equal for the Pt and Pt/Au samples.

The similar activities of bulk Pt and Pt/Au suggest that the active sites on Pt/Au are bulk Pt. A true Pt monolayer on an Au support would increase the HBE due to the expansive strain on the Pt overlayer.[20] According to the volcano relationship for alkaline HER/HOR, an increased HBE would decrease the activity of the catalyst. However, our results show no decrease in activity for the Pt/Au catalysts. The alkaline CO stripping data, which illustrates that the Pt/Au surface closely resembles bulk Pt, also supports the idea that Pt does not form a true monolayer on the Au surface.

Although the data indicates that the synthesis method used in this study does not produce a true Pt monolayer, the Pt/Au catalysts may still have a higher Pt utilization than bulk Pt catalysts. This is true for Pt-modified catalysts for ORR in acid.[20,21] While Au may be an expensive substrate, the possibility remains open to electrochemically deposit Pt nanoparticles on less expensive substrates and maintain a high alkaline HER/HOR current density.

In summary, Pt/Au catalysts were synthesized using a galvanic displacement technique. These catalysts show similar activity as bulk Pt for the alkaline HOR/HER

while utilizing far less Pt metal, though the Cu monolayer displacement method has been shown to not produce a full monolayer. This opens future study for other low-Pt catalysts for this reaction in order to decrease the cost of HEMFCs, such as depositing monolayer loadings of Pt onto other non-Pt metal substrates.

## Chapter 5

### PLATINUM-MODIFIED TRANSITION METAL CARBIDES FOR THE ALKALINE HYDROGEN OXIDATION REACTION

In Chapter 4, it was shown that monolayer amounts of Pt deposited on Au substrates exhibits similar activity as bulk Pt for the alkaline HOR. While the Pt/Au catalysts provide a high HOR activity using less Pt, Au is still a very expensive substrate. Therefore, it is important to find a less expensive substrate to support Pt. Carbon is usually used as a substrate for Pt electrocatalysts because it is inexpensive as well as conductive. However, Pt is not stable on carbon supports in acidic electrolytes, which has promoted research into alternative supports.[90]

In 1973, it was shown that tungsten carbide (WC) behaves similarly to Pt in some catalytic reactions due to electronic changes in tungsten when carburized.[91] Previously, monolayer depositions of Pt on WC thin films have shown identical HER, ORR, and methanol oxidation activity as Pt in acidic electrolytes.[54,55,92] Additionally, a library of other transition metal carbides (TMCs) was developed to show that carbides other than WC are stable in acidic and alkaline media under the operating conditions for the HOR/HER reactions.[93]

While TMCs may prove to be excellent substrates for low-Pt loading electrocatalysts, one drawback of these studies is that the thin films used cannot be used in actual fuel cell devices. Therefore, it is important to transition from Pt deposited on thin films to Pt deposited on powder catalysts. This chapter focuses on the testing of 5 wt% Pt supported on niobium carbide (NbC), tantalum carbide (TaC),

vanadium carbide (VC), zirconium carbide (ZrC), and titanium carbide (TiC) powders for the alkaline HOR. Due to the difficulty of obtaining electrochemically active surface areas through the integration of the HUPD region of Pt in the Pt/TMC samples, copper stripping was used instead.

### Preparation and Electrode Synthesis of 5% Pt/TMC Electrocatalysts

Pt was deposited on NbC, TaC, VC, ZrC, and TiC powders through incipient wetness impregnation (Chapter 2.1.3). Table 5.1 includes the ink recipes used for the preparation of the electrodes. For some of the catalysts, specifically 5% Pt/NbC and 5% Pt/TiC, more than one drop of catalyst was required due to the nature of the solvent. In between each drop, the electrode was allowed to dry completely before the next drop was deposited. In the case of Pt/TiC, where ethylene glycol was used as the solvent, the solvent was evaporated by drying the electrode in an oven at 100 °C for 1 hour.

Table 5.1: Ink recipes used for 5% Pt/TMC catalysts.

Catalyst	$\text{mg}_{\text{catalyst}}/\text{mL}_{\text{ink}}$	Solvent	Drop Volume ( $\mu\text{L}$ )	$\mu\text{g}_{\text{metal}}/\text{cm}^2_{\text{disk}}$	$\mu\text{g}_{\text{support}}/\text{cm}^2_{\text{disk}}$
5% Pt/NbC	17.4	100% isopropanol	3 (x3)	40	760
5% Pt/TaC	15.7	50% isopropanol 50% H <sub>2</sub> O	10	40	760
5% Pt/TiC	7.8	100% ethylene glycol	10 (x2)	40	760
5% Pt/VC	15.7	50% isopropanol 50% H <sub>2</sub> O	10	40	760
5% Pt/ZrC	15.7	50% isopropanol 50% H <sub>2</sub> O	10	40	760

Since the TMC supports have high molecular weights and the loading of Pt on the TMC support is low, the loading of support on the electrode is much higher than the recommended  $50 \mu\text{C}/\text{cm}^2_{\text{disk}}$  for carbon supported Pt catalysts. The corresponding molar loading for carbon supported catalysts is  $4.2 \mu\text{mol}/\text{cm}^2_{\text{disk}}$ , while the molar loadings for the Pt/TMC catalysts range from  $3.9 \mu\text{mol}/\text{cm}^2_{\text{disk}}$  for NbC to  $12.7 \mu\text{mol}/\text{cm}^2_{\text{disk}}$  for TaC. Therefore, the TMC loading for the electrodes is within reason. The cell resistance was slightly higher for the electrodes with a high TMC loading due to the

### **Comparison of 5% Pt/TMC Electrocatalysts for Alkaline HOR/HER**

#### **Determination of Electrochemically Active Surface Area of Pt/TMC Electrodes**

In order to obtain exchange current densities that are normalized by the actual Pt surface area of the Pt/TMC catalysts, copper stripping was used to calculate the roughness factors. CVs of the Pt/TMC catalysts did not display the Pt HUPD region, so copper stripping is used to estimate of the active surface area.

Figure 5.1 shows the copper stripping LSVs for each Pt/TMC catalyst with the background current subtracted. The copper stripping LSV for Pt/C is also shown for reference (Figure 5.1f). The different peaks in the LSV appear due to reconstructions of the copper overlayer on different Pt facets. Specifically, the peaks at  $\sim 0.40 \text{ V}$ ,  $0.55 \text{ V}$ , and  $0.70 \text{ V}$  vs. RHE that appear in the LSV for Pt/C due to the presence of the Pt(100), Pt(110), and Pt(111), respectively.[94]

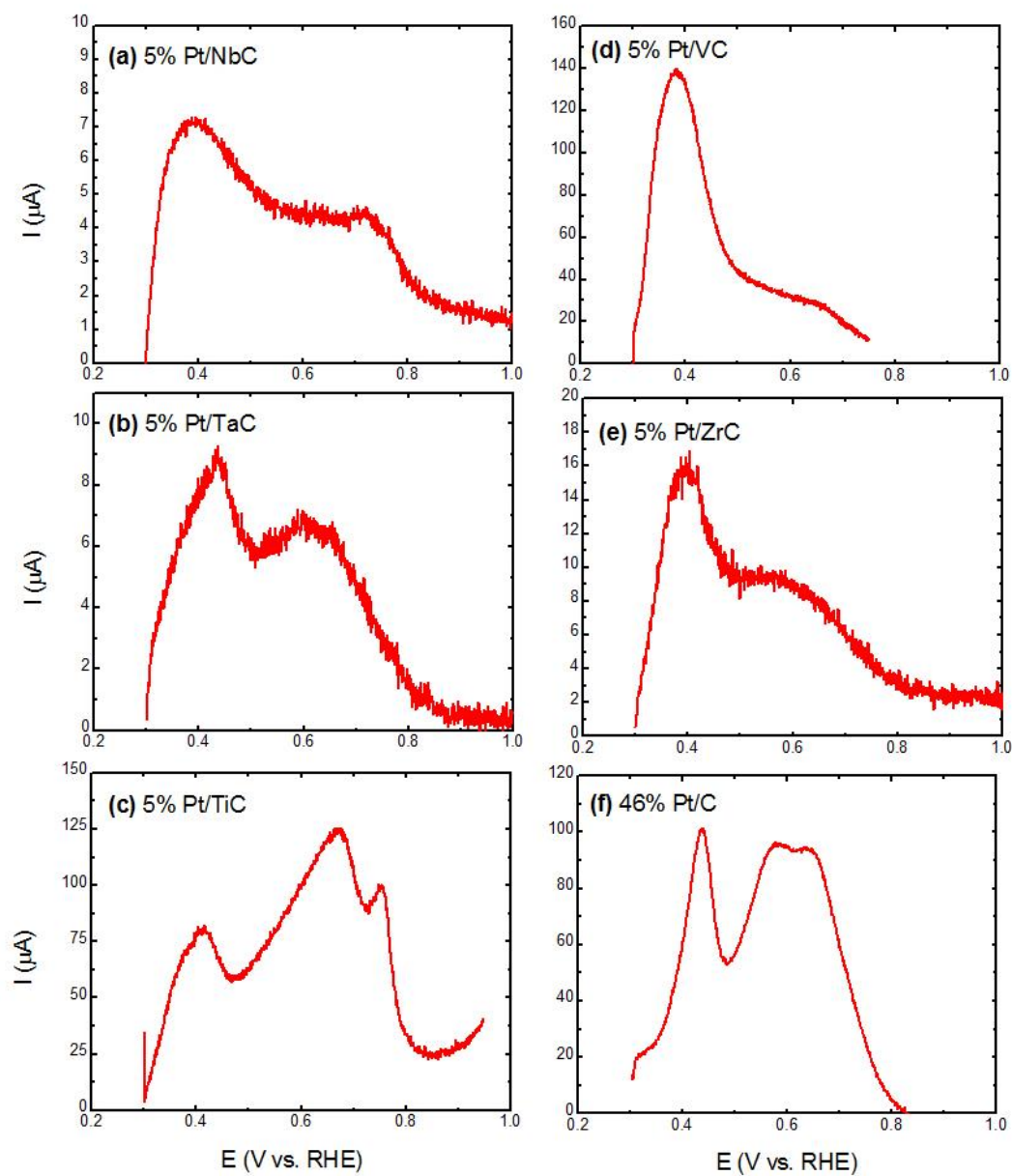


Figure 5.1: Copper stripping LSVs for each Pt/TMC catalyst as well as 46% Pt/C for comparison. Each LSV has had the background current subtracted. Each catalyst displays the general copper stripping features of Cu.

For each of the 5% Pt/TMC electrocatalysts, the peak corresponding to Pt(100) is visible. On 5% Pt/VC, this peak is especially strong compared to the other peaks, suggesting that Pt(100) is the main crystalline facet active on this catalyst. Previously, Pt particles that were electrodeposited on WC substrates that showed this copper stripping feature were found to have a cubic shape.[95] This feature is also the strongest in the copper stripping LSVs of 5% Pt/NbC, 5% Pt/Ta/C, and 5% Pt/ZrC, indicating that Pt(100) is present in these catalysts as well.

The copper stripping features of the 5% Pt/TiC are the most similar to those of Pt/C. All copper stripping features for the Pt(100), Pt(111), and Pt(110) facets are present. However, the Pt(100) peak at 0.4 V vs. RHE is the smallest, suggesting that there is a small fraction of the Pt(100) facets on the surface.

Table 5.2: Roughness factors calculated for each Pt/TMC catalyst using copper stripping.

Catalyst	Roughness Factor ( $\text{cm}^2_{\text{Pt}}/\text{cm}^2_{\text{disk}}$ )			
	#1	#2	#3	Average
<b>5% Pt/NbC</b>	1.1	1.2	0.5	<b><math>0.9 \pm 0.2</math></b>
<b>5% Pt/TaC</b>	0.7	0.7	1.4	<b><math>0.92 \pm 0.2</math></b>
<b>5% Pt/TiC</b>	6.9	7.4	7.6	<b><math>7.3 \pm 0.2</math></b>
<b>5% Pt/VC</b>	3.4	6.0	5.5	<b><math>5.0 \pm 0.8</math></b>
<b>5% Pt/ZrC</b>	1.2	0.5	1.2	<b><math>1.0 \pm 0.2</math></b>

The electrochemically active surface areas of the catalysts were calculated by integrating the copper stripping LSVs. The roughness factors for each electrode are shown in Table 5.2, which varied for each catalyst depending on the support used. The 5% Pt/TiC catalyst has the highest roughness factor at  $7.3 \pm 0.2$ , indicating the dispersion on the TiC support is the highest compared to the other supports. Additionally, the copper stripping LSV of the 5% Pt/TiC has the highest current and has well-defined copper stripping features. 5% Pt/VC was also found to have a high roughness factor of  $5.0 \pm 0.8$ , but there was a high variability, meaning the dispersion is not consistent for each electrode. The other Pt/TMC catalysts have roughness factors of  $\sim 1.0$ . Comparing these values to a roughness factor of  $4.1 \pm 0.2$  for Pt/C electrodes of lower loading indicates that the Pt/NbC, Pt/TaC, and Pt/ZrC are not well dispersed.

### **5% Pt/TMC Alkaline HOR Activity**

Separate 5% Pt/TMC electrodes were prepared for measuring HOR/HER activity so the electrolyte was not contaminated from the copper stripping solution. The average roughness factor was used to normalize the current density for the kinetic analyses. A summary of the exchange current densities, Tafel slopes, and transfer coefficients are listed in Table 5.3.

Both 5% Pt/TiC and 5% Pt/VC electrodes were active enough to reach mass-transport limiting current densities and were analyzed by fitting to the Butler-Volmer equation (Figure 5.2). The polarization curves for both electrodes were started under 0.6 V vs. RHE so the TMC supports were not oxidized.[93] While the polarization curves for 5% Pt/TiC plateau above 0.3 V vs. RHE, the mass transport limiting current density is lower than for Pt/C. At 1600 rpm, the maximum current for 5% Pt/TiC is

$\sim 2.0 \text{ mA/cm}^2_{\text{disk}}$ , where for Pt/C the maximum current at 1600 rpm is  $\sim 2.8 \text{ mA/cm}^2_{\text{disk}}$  (Figure 5.2a). This may be due to mass transport problems caused by the thickness

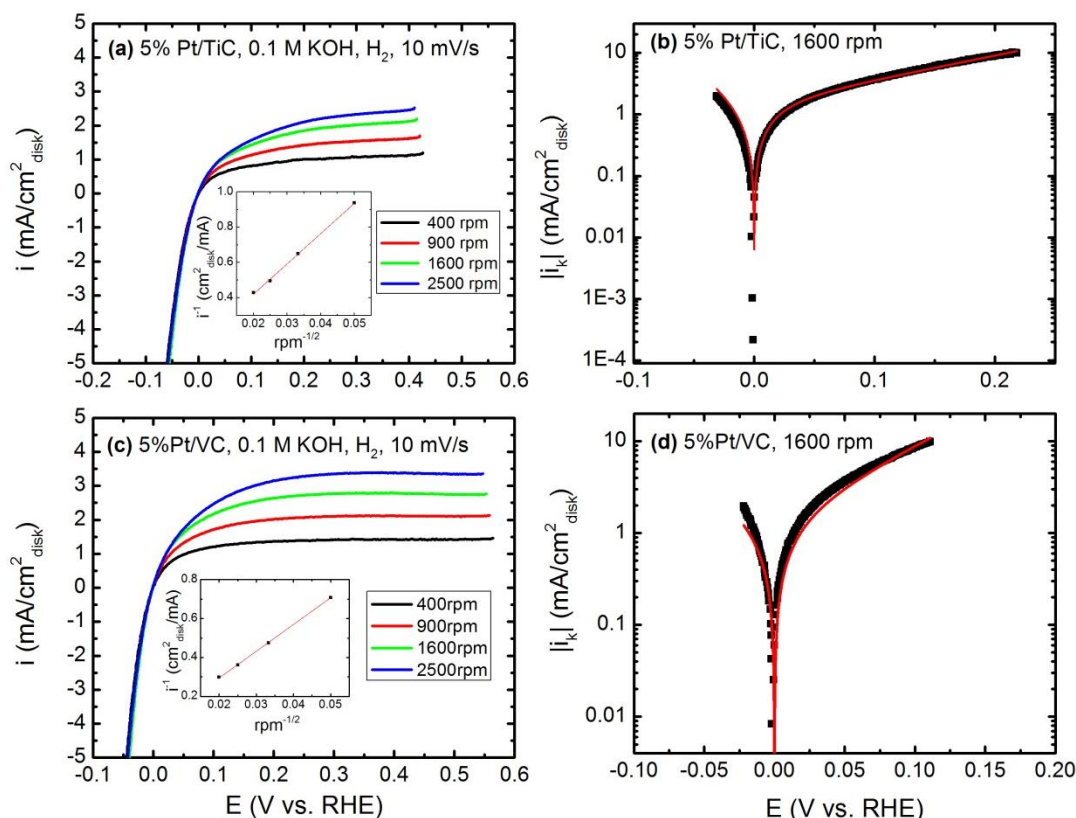


Figure 5.2: Polarization curves and fits to the Butler-Volmer equation for (a),(b) 5% Pt/TiC and (c),(d) 5% Pt/VC.

of the TMC support on the electrode. The loading of TiC on the electrode is  $760 \mu\text{g}_{\text{TiC}}/\text{cm}^2_{\text{disk}}$ , which corresponds to a molar loading of  $12.7 \mu\text{mol}_{\text{TiC}}/\text{cm}^2_{\text{disk}}$ . This is much higher than the recommended carbon loading of  $4.2 \mu\text{mol}_{\text{C}}/\text{cm}^2_{\text{disk}}$ . Therefore this electrode will have mass transport contributions that cannot be accounted for. This is also apparent in fit to the Butler-Volmer equation for 5% Pt/TiC, where the

HOR branch is not symmetric with the HER branch (Figure 5.2b). The transfer coefficient calculated for this catalyst was  $0.24 \pm 0.02$ , which reflects this problem. The exchange current density of 5% Pt/TiC obtained from the fit was  $-3.67 \pm 0.01$ , which may be skewed due to the additional mass transport contributions that were not able to be corrected.

The 5% Pt/VC electrodes also reach a mass transport limiting current. Unlike 5% Pt/TiC, the maximum current of  $\sim 2.8 \text{ mA/cm}^2_{\text{Pt}}$  at 1600 rpm closely matches that of Pt/C (Figure 5.2c). The HOR branch and HER branch in the fit to the Butler-Volmer equation are more symmetric than for the 5% Pt/TiC electrode (Figure 5.2d). The transfer coefficient obtained from the fit to the Butler-Volmer equation was  $0.34 \pm 0.02$ , which is lower than the expected transfer coefficient of  $\sim 0.5$  for Pt catalysts.

The 5% Pt/NbC, 5% Pt/TaC, and 5% Pt/ZrC catalysts were not active enough to reach mass transport limiting current densities and were therefore analyzed using the Tafel slope method (Figure 5.3). This is likely due to the fact that the electrodes for these catalysts have relatively low roughness factors or  $\sim 1.0$ . The  $\log(i_0 \text{ A/cm}^2_{\text{Pt}})$  values calculated were  $-3.8 \pm 0.5$ ,  $-3.5 \pm 0.3$ , and  $-3.4 \pm 0.1$  for 5% Pt/NbC, 5% Pt/TaC, and 5% Pt/ZrC, respectively. The high variation in these numbers is likely due to inherent inaccuracies in using the Tafel slope to extract kinetic data, but also because the current density could only be normalized by an average roughness factor and not a sample-specific roughness factor. Therefore, the exchange current density is expected to have higher uncertainty for these samples. The Tafel slopes calculated for 5% Pt/NbC, 5% Pt/TaC, and 5% Pt/ZrC were  $-127 \pm 13$ ,  $-547 \pm 90$ , and  $-373 \pm 19$ , respectively. These correspond to transfer coefficients at 298 K of 0.47,

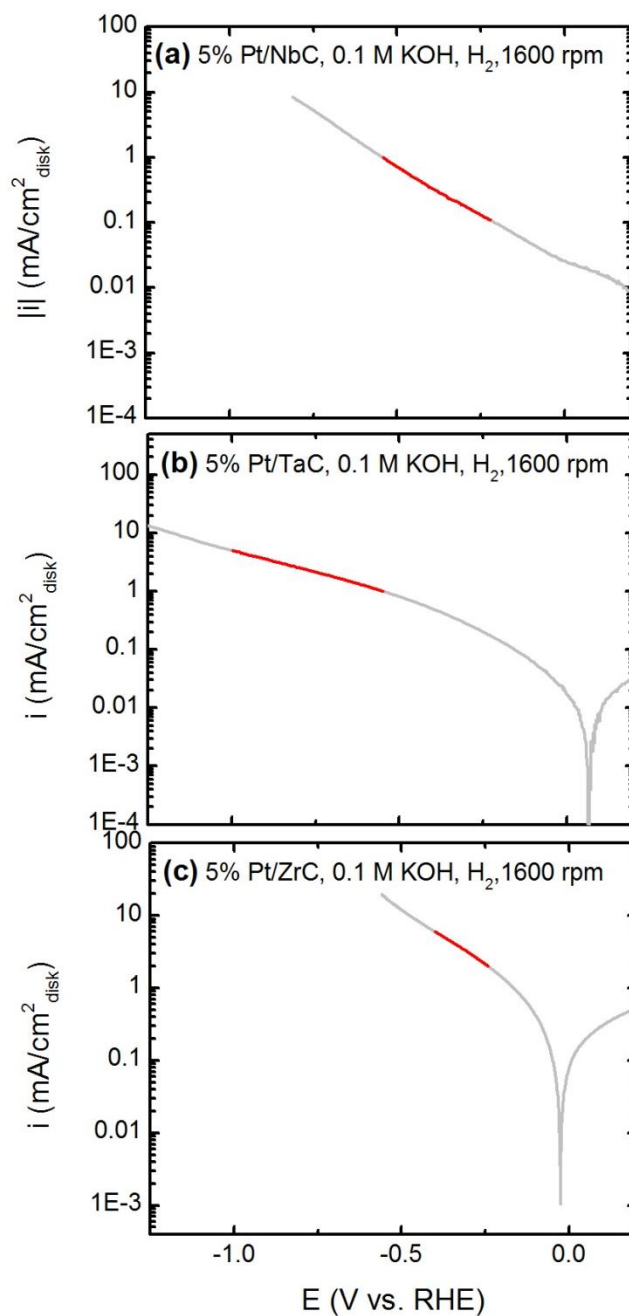


Figure 5.3: LSVs at 1600 rpm in H<sub>2</sub>-saturated 0.1 M KOH for (a) 5% Pt/NbC, (b) 5% Pt/TaC, and 5% Pt/ZrC. The red lines are the data used for the linear fit and extrapolation to 0 V vs. RHE.

Table 5.3: Measured exchange current densities for each 5% Pt/TMC catalyst. The Tafel slope or transfer coefficient is also listed for each depending on whether the Tafel or Butler-Volmer method was used, respectively.

		#1	#2	#3	Average
5% Pt/NbC	$\log(i_0 \text{ A/cm}^2_{\text{Pt}})$ Tafel	-4.7	-3.2	-3.5	<b>-3.8 ± 0.5</b>
	Tafel Slope (mV/dec)	-336.7	-220.8	-408.2	<b>-127 ± 13</b>
5% Pt/TaC	$\log(i_0 \text{ A/cm}^2_{\text{Pt}})$ Tafel	-3.8	-3.2	--	<b>-3.5 ± 0.3</b>
	Tafel Slope (mV/dec)	-656	-437	--	<b>-547 ± 90</b>
5% Pt/TiC	$\log(i_0 \text{ A/cm}^2_{\text{Pt}})$ Tafel	-3.69	-3.65	-3.67	<b>-3.67 ± 0.01</b>
	$\alpha_a$ ( $\alpha_a + \alpha_c = 1$ )	0.24	0.29	0.24	<b>0.25 ± 0.02</b>
5% Pt/VC	$\log(i_0 \text{ A/cm}^2_{\text{Pt}})$ Tafel	-3.45	-3.40	-3.48	<b>-3.44 ± 0.02</b>
	$\alpha_a$ ( $\alpha_a + \alpha_c = 1$ )	0.32	0.38	0.32	<b>0.34 ± 0.02</b>
5% Pt/ZrC	$\log(i_0 \text{ A/cm}^2_{\text{Pt}})$ Tafel	-3.2	-3.4	-3.5	<b>-3.4 ± 0.1</b>
	Tafel Slope (mV/dec)	-386	-336	-398	<b>-373 ± 19</b>

0.11, and 0.16, respectively. While the transfer coefficient of 5% Pt/NbC is close to the value of ~0.48 obtained for Pt/C catalysts, the values of 0.11 and 0.16 for 5% Pt/TaC and 5% ZrC are much lower.

The exchange current densities of each Pt/TMC are plotted in Figure 5.4 and compared to Pt/C. While the average exchange current density of each 5% Pt/TMC catalyst is lower than that of Pt/C, the actual activity seems to be comparable to Pt once the uncertainty is taken into account. Since one of the goals of this study was to find if the TMC support could tune the activity of the deposited Pt, this is an important

conclusion. From what is seen in Figure 5.4, no discernable differences can be seen between the activity of Pt/C and the 5% Pt/TMC catalysts, especially for the catalysts analyzed with the Tafel slope method (5% Pt/NbC, 5% Pt/TaC, and 5% Pt/ZrC). The inherently higher uncertainty in the measured exchange current densities makes this conclusion difficult to make.

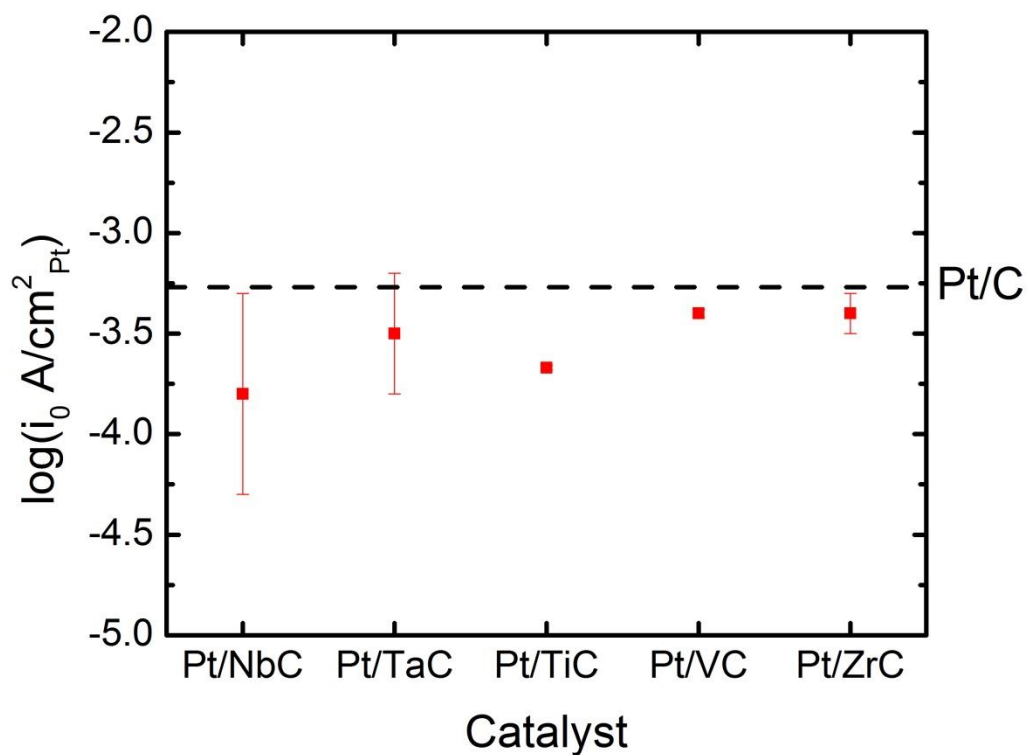


Figure 5.4: Exchange current densities of each 5% Pt/TMC catalyst compared to Pt/C (black dotted line).

One reason the Pt in these catalysts may not be subject to tuning from the TMC support is the particulate nature of the impregnated Pt. What is evident from the measured roughness factors of the 5% Pt/TMC catalysts is that the impregnation method used to synthesize the samples results in very different dispersions for each support. Though the same methods were used for all catalysts, the roughness factors for the Pt/NbC, Pt/TaC, and Pt/ZrC are quite low compared to the Pt/TiC and Pt/VC, even though the electrodes are prepared with the same loading of Pt. This indicates that larger Pt particles form on the NbC, TaC, and ZrC supports, while smaller particles with a higher active surface area are formed on the TiC and VC supports. This is likely due to different Pt interactions with each TMC. While this effect does not seem to dictate HOR/HER activity alone, the catalysts with larger Pt particles may not undergo tuning from the TMC at all, since there is low contact between the Pt and support. There may be a higher degree of tuning for the Pt/TiC and Pt/VC catalysts, if any, since there is a higher coverage of Pt on the support.

In conclusion, the 5% Pt/TMC catalysts were found to have comparable activity to state-of-the-art Pt/C. No tuning of Pt from the TMC support could be found from this study. In order to further investigate the effect of the TMC support on Pt nanoparticles, better synthesis techniques or conditions should be considered to increase the dispersion of Pt on the NbC. In addition, the surface area of the catalysts should be estimated using a technique such as CO stripping, so that each catalyst can be normalized by its specific surface area instead of an average. This will decrease the uncertainty in the measurement of the exchange current density and unravel any differences from the activity of Pt/C.

## Chapter 6

### PLATINUM-MODIFIED GOLD ELECTROCATALYSTS FOR THE OXIDATION OF ETHYLENE GLYCOL AND GLUCOSE

Despite the advantages of using biomass-derived oxygenates as a fuel cell feedstock, the development of commercially viable fuel cells has also been hindered by the prohibitive cost and scarcity of platinum (Pt) electrocatalysts. Although the ideal electrocatalysts for ethylene glycol oxidation (EGO) and glucose oxidation (GlcO) in alkaline media are Pt- and palladium-based electrocatalysts, which are too expensive for widespread applications,[4,97] using a Pt-modified electrocatalyst with very low Pt loadings would reduce the cost of the fuel cell. Pt-modified electrocatalysts have been previously used to minimize the expense of the catalysts for the oxygen reduction reaction (ORR)[53–55] and hydrogen evolution reaction (HER)[56–58] in acidic electrolytes. In this study, we report the evaluation of the activity of Pt-modified gold (Pt/Au) disk and supported (Pt/Au/C) electrodes for EGO and GlcO. To synthesize the Pt/Au catalysts, a coverage equivalent to a monolayer of Pt was deposited on Au substrates via the galvanic displacement of a copper monolayer (Chapter 4.1). The EGO and GlcO activity in 0.1 M KOH was obtained on Pt, Au, and Pt/Au disk electrodes, as well as on the corresponding supported catalysts Pt/C, Au/C, and Pt/Au/C because of the practical application of supported catalysts in fuel cell devices. Furthermore, *in-situ* FTIR was performed on each disk electrode to gain further insight into the mechanism by which the EGO and GlcO reactions are completed in alkaline electrolytes.

## 6.1 Ethylene Glycol Oxidation on Pt/Au Surfaces

### 6.1.1 Electrochemical Activity

The activity of the Pt/Au catalysts was tested for EGO in alkaline electrolytes via CV and compared to the activity of monometallic Pt and Au catalysts for both disk and supported electrodes (Figure 6.1). The current was normalized by the Pt area determined from CO stripping for the Pt and Pt/Au disk and supported samples. All surfaces show two anodic peaks in the forward and reverse scans of each CV. In the forward scan for the Pt and Pt/Au disks (Figure 6.1a), oxidation occurs at approximately 0.5 V vs, RHE, though the Pt/Au sample has a slightly lower onset potential. After achieving a maximum current density at ~1.2 V vs. RHE, the oxidation currents of the Pt and Pt/Au disks precipitously decrease due to the formation of Pt surface oxides that render the surface inactive. In the reverse scan, the surface oxides are reduced and the oxidation current increases again. The oxidation onset potentials for the Pt and Pt/Au disks are approximately 0.2 V lower than that of the Au disk. For the Au disk, the maximum occurs at ~1.5 V vs. RHE. The Pt/C and Pt/Au/C catalysts produce less current than their respective disk electrodes (Figure 6.1b), but follow the same trends. Au/C and the Au disk, however, both achieve the same maximum current density.

The Pt/Au disk achieves a slightly higher maximum current density than the Pt disk. This may be due to the uncovered Au substrate participating in the reaction at potentials above the oxidation onset potential of the Au disk. This is also apparent by the appearance of small shoulders in the CVs of the Pt/Au disk and Pt/Au/C corresponding to the formation of AuO.

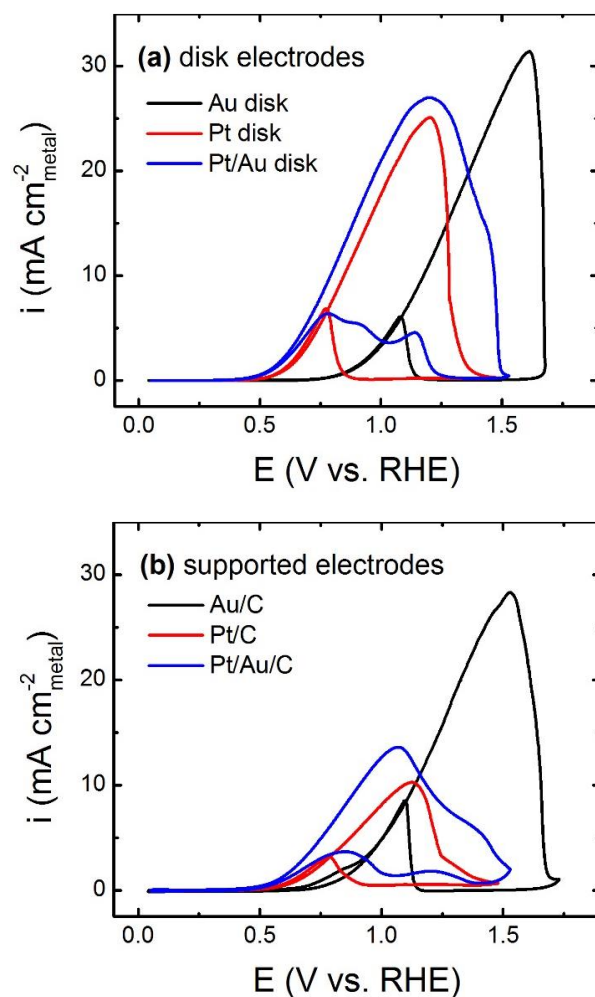


Figure 6.1: CVs taken at  $50 \text{ mV s}^{-1}$  of (a) Pt, Au, and Pt/Au disk electrodes and (b) Pt/C, Au/C, and Pt/Au/C electrodes in deaerated  $0.1 \text{ M KOH}$  and  $1 \text{ M EG}$ .

However, below the Au onset potential, the surface area of the Pt/Au determined by CO stripping is accurate and therefore the current density is correctly normalized.

Chronoamperometry (CA) measurements were performed to evaluate the steady-state activity and stability of each disk electrode for the oxidation of EG at  $0.8 \text{ V vs. RHE}$  (Figure 6.2). This potential was chosen since it is plausible in a HEMFC

utilizing EG as a feedstock. While Au is an active metal for this reaction, it is not active at this potential, which hinders its use for fuel cell use. In addition, the inactivity of Au at this potential allows a better comparison between the activity of Pt and Pt/Au. The uncovered substrate in the Pt/Au sample will not participate in oxidation at this potential. The Pt and Pt/Au disks initially yield a current density of  $8 \text{ mA cm}^{-2}_{\text{Pt}}$  and  $6 \text{ mA cm}^{-2}_{\text{Pt}}$ , respectively, but Pt rapidly deactivates to a steady-state current of  $\sim 0.3 \text{ mA cm}^{-2}_{\text{Pt}}$ . Pt/Au, however, retains a current of  $\sim 4.25 \text{ mA cm}^{-2}_{\text{Pt}}$  until 3600 seconds.

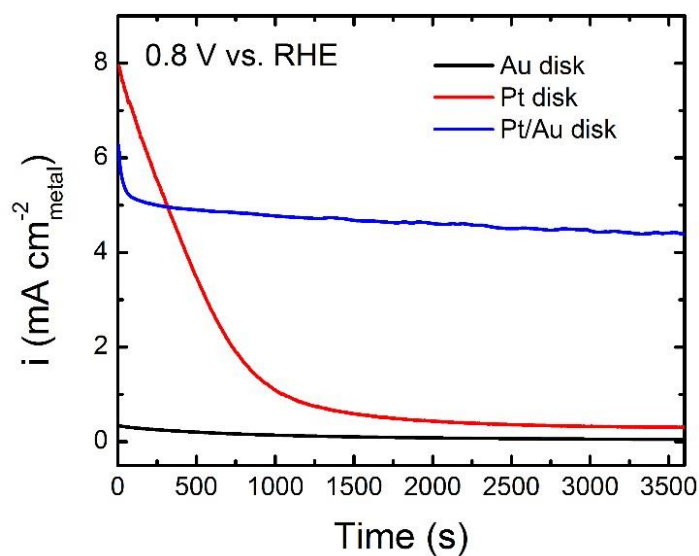


Figure 6.2: Chronoamperometry measurements for the Au, Pt, and Pt/Au disk electrodes taken at 0.8 V vs. RHE in 0.1 M KOH and 1 M EG.

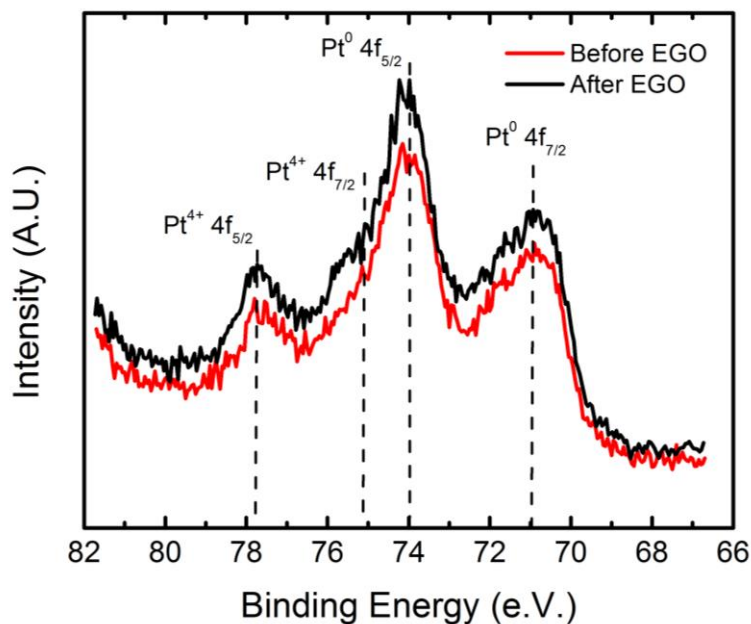


Figure 6.3: Pt 4f XPS spectra of the Pt/Au disk before and after the EGO CA at 0.8 V vs. RHE for 3600 seconds. The Pt surface remains unchanged after EGO at this potential.

To further analyze the stability of the Pt/Au disk at 0.8 V vs. RHE, XPS was performed after the CA and compared to the spectra before the reaction (Figure 6.3). The Pt 4f features of the Pt/Au disk, explained in Chapter 4.2.2, remain unchanged after the EGO CA experiment, indicating the Pt/Au surface is preserved for EGO at this potential.

While the CV and CA results can show general trends for each electrode, information regarding the EGO mechanism is difficult to obtain from these methods alone. Therefore, in-situ FTIR was used to analyze the reaction products.

### 6.1.2 Mechanistic Interpretation of EGO on Pt/Au Using FTIR

The mechanism of EGO on Pt and Au catalysts in alkaline media has been well studied,[98] but how the mechanism changes on the Pt/Au surface is unclear.

Therefore, FTIR was used to analyze the EGO intermediates and products on the Pt, Au, and Pt/Au disks (Figure 6.4) using known vibrational peak assignments (Table 6.1).

The FTIR spectra for EGO on the Au disk agrees with previous spectra obtained in 0.5 M KOH (Figure 6.4a).[98] Vibrational features appear at around ~1.0 V vs. RHE, similar to the onset potential observed in the Au disk EGO CV (Figure 6.1a). The peaks at 1577, 1409, 1323, 1237, and 1074  $\text{cm}^{-1}$  indicate that glyoxal and glycolate are present after the onset of oxidation at ~1.0 V vs. RHE. A peak at 1353  $\text{cm}^{-1}$  appears at 1.3 V vs. RHE, suggesting the formation of formate. This formate species may come from the oxidation of glycolate at higher potentials.[99] The lack of a peak at 2341  $\text{cm}^{-1}$  indicates that very little  $\text{CO}_2$  is produced on the Au surface. It is well established that Au electrocatalysts in alkaline media do not break the C–C

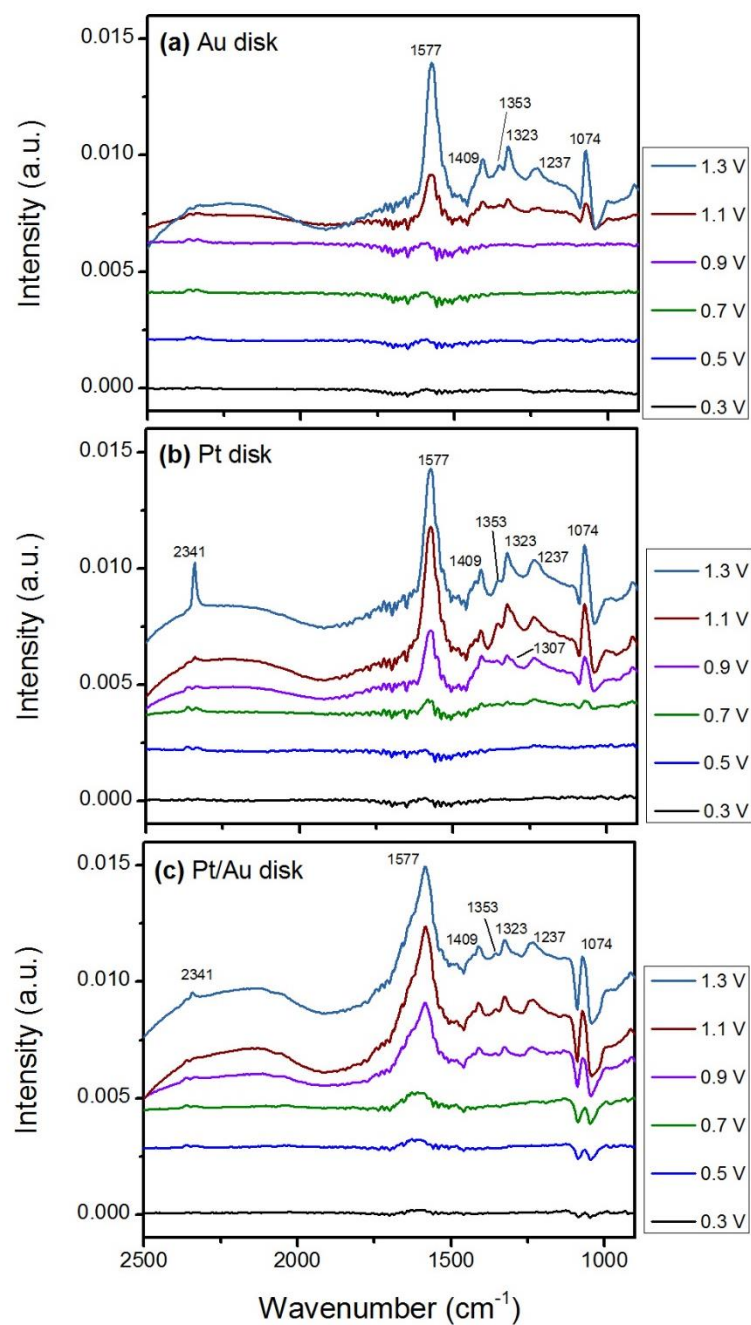


Figure 6.4: Selected FTIR spectra of the (a) Au, (b) Pt, and (c) Pt/Au disk electrode during EGO. Spectra were obtained in 0.1 M KOH and 0.2 M EG purged in  $N_2$  while the potential was scanned at  $1 \text{ mV s}^{-1}$ . All potentials are referred to RHE.

Table 6.1: Peak assignments for the FTIR spectra of EGO.

Frequency (cm <sup>-1</sup> )	Assignment
1074	Aldehyde stretch in glyoxal and glycolate[98,100,101]
1237	C–O stretch of glycolate[100,102]
1323	Symmetric COO <sup>-</sup> stretch of glycolate, glyoxal, and oxalate[100,102]
1353	Symmetric COO <sup>-</sup> stretch in formate[98,99,101] Adsorbed carbonylate[100,102]
1409	Symmetric COO <sup>-</sup> stretch in glycolate[98,101] Carbonate (CO <sub>3</sub> <sup>-2</sup> ) [100,103]
1577	Asymmetric COO <sup>-</sup> stretch in glyoxal and glycolate[98,100–102]
2341	Asymmetric CO <sub>2</sub> stretch[98,100–102]

bond and instead provides a hydroxylated surface on which a deprotonated alcohol may react.[104]

Conversely, the Pt surface is able to break the C–C bond in EG at high overpotentials, as evident by the onset of the CO<sub>2</sub> band at 2341 cm<sup>-1</sup> at 1.3 V vs. RHE (Figure 6.4b). At 0.7 V vs. RHE, small vibrational peaks appear, which by 0.9 V vs. RHE have developed into peaks at 1577, 1409, 1323, 1237, and 1074 cm<sup>-1</sup>, corresponding to the characteristic vibrational frequencies of glyoxal, glycolate, and oxalate. The small shoulder at 1307 cm<sup>-1</sup> also suggests that oxalate is produced.

The Pt/Au disk spectra show a weak CO<sub>2</sub> peak at 2341 cm<sup>-1</sup> by 1.3 V vs. RHE (Figure 6.4c), but it is not as prominent as that of the Pt surface. The peak at 1577

$\text{cm}^{-1}$  associated with glyoxal and glycolate is broadened in the Pt/Au spectra. Otherwise, the IR features at 1577, 1409, 1323, 1237, and 1074  $\text{cm}^{-1}$  on the Pt/Au surface are similar to Au, indicating that the main products on the Pt-modified surface are glyoxal and glycolate.

While the Pt/Au surface does decrease the onset potential of the EGO reaction compared to pure Au, which is important for fuel cell applications, the FTIR results indicate that the Pt/Au surface does not oxidize EG completely to  $\text{CO}_2$  as efficiently as Pt. While this decreases the overall Faradaic efficiency for the Pt/Au surface, it increases the stability of the catalyst (Figure 6.2a). One possible explanation is that since the Pt/Au does not break the C-C bond, no carbon residues are produced to poison the catalyst surface.

## **6.2 Glucose Oxidation on Pt/Au Surfaces**

### **6.2.1 Electrochemical Activity**

The activities of Pt/Au catalysts were tested for GlcO under alkaline conditions and compared to Pt and Au (Figure 6.5). The Au disk and supported Au/C for GlcO have onset potentials of 0.3 V vs. RHE, which are much lower than those of the Au catalysts for EGO. In addition, even at low potentials, the Au disk and Au/C achieve a higher current density than the Pt catalysts for GlcO. During the forward scan, the Au disk attains a current density of about  $8 \text{ mA cm}^{-2}_{\text{Au}}$  at 0.75 V vs. RHE. The oxidation current subsides at 1.6 V vs. RHE, which coincides with the formation of oxides on the Au surface.[71] In the reverse scan, after the Au surface is reduced, there is a sharp increase in oxidation current, suggesting that the oxidized Au surface does not participate in GlcO.[105] The supported Au/C electrode for GlcO also has an

onset potential at 0.3 V vs. RHE and reaches approximately the same current density as the Au disk, but there are two oxidation peaks in the forward scan at  $\sim 0.8$  and 1.5 V vs. RHE.

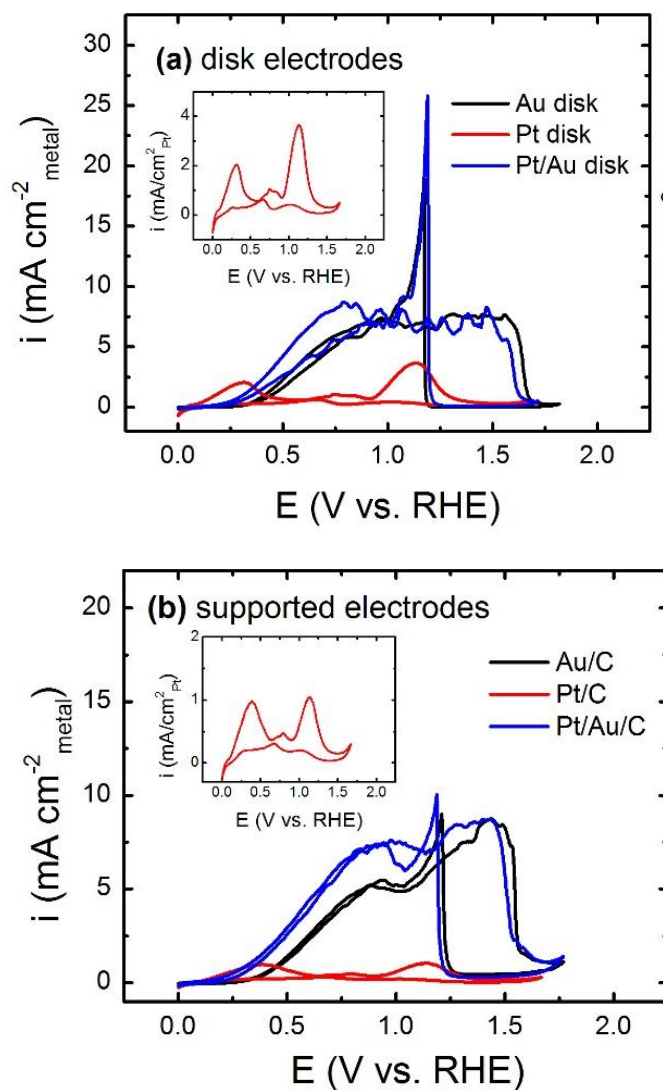


Figure 6.5: CVs taken at 50 mV/s of (a) Pt, Au, and Pt/Au disk electrodes and (b) Pt/C, Au/C, and Pt/Au/C electrodes in Ar-purged 0.1 M KOH and 0.1 M Glc. The inset graphs are zoomed in on the Pt CVs to show more detail.

This is likely due to the presence of different Au facets on the Au particles to the Au disk.[106] The reverse oxidation peak of the Au/C CV for GlcO is not as pronounced as the Au disk.

In agreement with literature on GlcO, the Pt disk CV has three oxidation peaks in the forward scan, appearing at 0.3, 0.75, and 1.1 V vs. RHE, and three smaller oxidation peaks in the reverse scan.[107–109] The first peak has been attributed to the dehydration and adsorption of Glc onto the Pt surface, the second to oxidation of adsorbed Glc by the  $\text{OH}_{\text{ad}}$  species, and the third to oxidation of Glc in solution with the oxidized Pt surface.[109–112] The reverse scan peaks occur at similar potentials as the forward scan peaks. While Pt has a lower onset potential than Au with oxidation commencing at slightly above 0 V vs. RHE, the Pt electrode achieves a lower peak current density, with the highest current being  $4 \text{ mA cm}^{-2}_{\text{Pt}}$  at 1.2 V vs. RHE. The Pt/C GlcO CV is similar to the Pt disk GlcO CV, but with two differences (Figure 6.5b). First, Pt/C achieves approximately half the current density as the Pt disk. Second, the ratio between the forward oxidation peaks is different between supported Pt/C and the Pt disk. Specifically, the last oxidation peak for Pt/C is about equal in magnitude to the first peak, while on the Pt disk it is about twice as large. This difference can also be attributed to the presence of different Pt facets on the particles compared to the disk.[112]

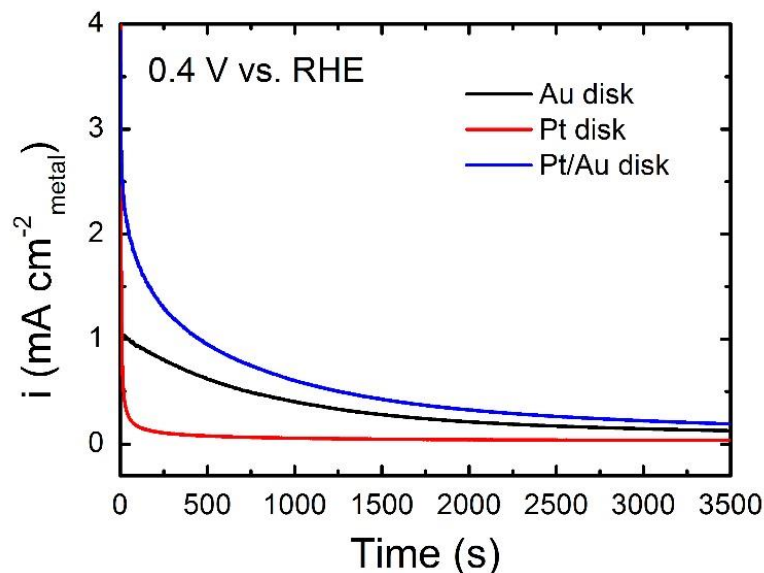


Figure 6.6: CA measurements for the Au, Pt, and Pt/Au disk electrodes taken at 0.4 V vs. RHE in Ar-purged 0.1 M KOH and 0.1 M Glc.

Both Pt/Au catalysts have a slightly lower onset potential for GlcO than their respective Au substrates. In the case of Pt/Au/C for GlcO, the onset potential matches that of Pt/C. However, unlike for EGO, the Pt/Au disk and Pt/Au/C oxidation CVs for GlcO are more similar to the Au and Au/C catalysts.

The steady-state activities of the Pt, Au, and Pt/Au disks for GlcO were compared by CA measurements at 0.4 V vs. RHE (Figure 6.6). This potential was chosen due to its physical viability for an HEMFC utilizing a glucose feedstock. Similar to the EGO CA experiments, Pt/Au was found to be more active and more stable than Pt at the chosen potential, though the difference is relatively small. In the case of GlcO, Au is more active than Pt at 0.4 V vs. RHE.

### 6.2.2 Mechanistic Interpretation of EtO on Pt/Au Using FTIR

To elucidate the GlcO reaction pathways occurring on Au, Pt, and Pt/Au, *in-situ* FTIR was used on each disk surface during the GlcO reaction (Figure 6.7) and compared to known peak assignments (Table 6.2). On the Au surface (Figure 6.7a), a broad peak is evident at  $1639\text{ cm}^{-1}$  from 0.3 V onward. At 0.5 V, a small shoulder appears that corresponds to gluconate at  $1595\text{ cm}^{-1}$ , which is also represented by the peak at  $1043\text{ cm}^{-1}$ . By 0.9 V, this gluconate shoulder is mostly overtaken by the large peak at  $1639\text{ cm}^{-1}$ . The consumption of Glc is indicated by the negative-going peaks at  $1388$  and  $1177\text{ cm}^{-1}$  starting at 0.5 V. Also at 0.7 V, a shoulder appears at about  $1740\text{ cm}^{-1}$  along with the peaks at  $1226$ ,  $1191$ , and  $1056\text{ cm}^{-1}$ , indicating that gluconolactone is formed.

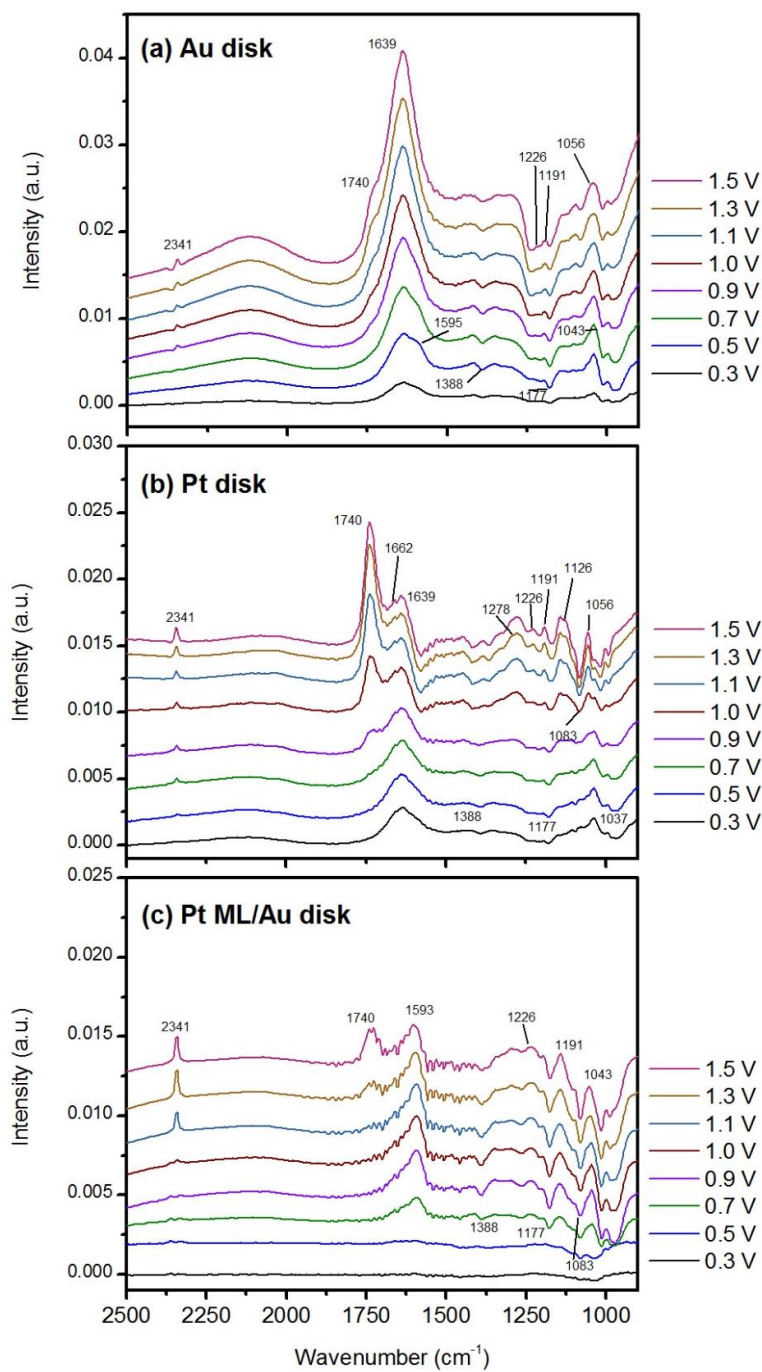


Figure 6.7: Selected FTIR spectra of the (a) Au disk, (b) Pt disk, and (c) Pt/Au disk during GlcO. Spectra were obtained in 0.1 M KOH and 0.2 M Glyc purged in  $\text{N}_2$  while the potential was scanned at 1 mV/s.

Table 6.2: Peak assignments for the IR spectra of GlcO.

Wavenumber (cm <sup>-1</sup> )	Assignment
1043	V(C -O) in CH <sub>2</sub> OH in gluconate[113]
1098	V(C -O) in CH <sub>2</sub> OH in gluconate[113]
1126	V(C-O) from CHOH in δ-gluconolactone[113]
1191	Unknown peak in δ-gluconolactone[113]
1226	CH wag in δ-gluconolactone[113]
1177 (negative)	V(C-O) from CH <sub>2</sub> OH in glucose[113]
1388 (negative)	C-H bending in glucose[108,113]
1593	Asymmetric stretch of O - C - O in gluconate[108,113]
1639	C=O of ring-opened glucose
1740	v(C=O) of δ-gluconolactone[108,113]
2341	Asymmetric CO <sub>2</sub> stretch[108,113]

The Au surface produces a small amount of CO<sub>2</sub>, as evidenced by the relatively weak peak at 2341 cm<sup>-1</sup>. Previous studies confirm that in 0.1 M NaOH, the Au surface produces a significant amount of gluconate as a final oxidation product.[107]

The Pt disk spectra differ from those of the Au disk (Figure 6.7b). At the beginning of the scan, broad positive-going peaks at  $1639\text{ cm}^{-1}$  and  $1039\text{ cm}^{-1}$  are apparent, though they are not as dominant as in the Au scan, along with negative going peaks at  $1388$  and  $1177\text{ cm}^{-1}$  indicating the consumption of Glc. The  $\text{CO}_2$  peak at  $2341\text{ cm}^{-1}$  starts to appear at approximately  $0.5\text{ V}$ . By  $0.9\text{ V}$ , and peaks at  $1740$ ,  $1226$ ,  $1191$ ,  $1126$  and  $1056\text{ cm}^{-1}$  start to form, indicating the production of gluconolactone.

It is interesting to note that the broad peak at  $1639\text{ cm}^{-1}$  is absent from the spectra of the Pt/Au disk. There is a peak located at  $1593\text{ cm}^{-1}$ , which is more consistent with the formation of gluconate. The production of gluconate is also confirmed by the peak at  $1043\text{ cm}^{-1}$ . Production of gluconolactone starts at about  $1.3\text{ V}$  with the appearance of vibrational features at  $1740$ ,  $1226$ , and  $1191\text{ cm}^{-1}$ .

For the Pt and Au disks, the peak at  $1639\text{ cm}^{-1}$  is dominant in the spectra over all potentials, but is not associated with glucose or any of the expected oxidation products. It was observed in the spectra of Pt in NaOH for GlcO in a previous study, but was not assigned.[113] This may be due to the adsorption of ring-opened glucose on the Pt and Au disks. While  $\beta - \text{D} - \text{glucose}$  is known to be the most reactive species in solution for GlcO, there still may be an adsorption of ring-opened glucose that occurs at all potentials, leading to the large feature at  $1639\text{ cm}^{-1}$  on Pt and Au. The Pt/Au surface does not show this peak, suggesting that the nature of the adsorbed species is different from that on Pt and Au, and that the Pt/Au surface selectively binds the reactive  $\beta - \text{D} - \text{glucose}$  species.

Overall, the pathways of GlcO on the Pt, Au, and Pt/Au disks follow the mechanism that is outlined in literature on metal surfaces.[105,107–109,113] First, the glucose adsorbs on the surface by reacting with solution phase  $\text{OH}^-$ , forming a

dehydrogenated molecule. This molecule can be oxidized directly to gluconate, which is observed in the IR spectra at all potentials. Alternatively, the adsorbed glucose can also be oxidized to gluconolactone, which reacts in alkaline solutions to form gluconate. While CO<sub>2</sub> is produced, it is not the main product. The production of CO<sub>2</sub> likely occurs from the further oxidation of gluconate and gluconolactone.

While the Pt/Au disk electrode has a mechanism similar to the Au disk for EGO, in the GlcO reaction the Pt/Au disk more closely resembles that of the Pt disk. This makes Pt/Au catalysts promising candidates for polyol oxidation while retaining a low Pt loading. While Au is an expensive support, the results demonstrate the proof-of-principle of using an equivalent of monolayer coverage of Pt to approach Pt-like properties, suggesting that modifying other, less expensive substrates with Pt may also be plausible.

Although EG can be used as a probe molecule for Glc, the results show that there are differences in activity and oxidation mechanism for EGO and GlcO. For example, Pt/Au does not break the C-C bond in EGO and therefore has a higher stability than Pt or Au. In contrast, Pt/Au does break the C-C bond for GlcO, but deactivates quickly. Further studies are needed to identify reaction intermediates and pathways that lead to these differences.

### **6.3 Ethanol Oxidation on Pt/Au Surfaces**

#### **6.3.1 Electrochemical Activity**

The activity of the Pt/Au catalysts was tested for EtO in alkaline electrolytes via CV and compared to the activity of monometallic Pt and Au catalysts for both disk and supported electrodes (Figure 6.8). The current was normalized by the Pt area

determined from CO stripping for the Pt and Pt/Au disk and supported samples. All surfaces show two anodic peaks in the forward and reverse scans of each CV. In the forward scan for the Pt disk (Figure 6.8a), oxidation occurs at approximately 0.3 V vs. RHE, though the Pt/Au sample has a slightly lower onset potential. After achieving a maximum current density at ~0.75 V vs. RHE, the oxidation currents of the Pt disk decreases due to the formation of Pt surface oxides that render the surface inactive. In the reverse scan, the surface oxides are reduced and the oxidation current increases again. The onset potential for the Pt/Au disk is 0.5 V vs. RHE, which is higher than the Pt disk. The oxidation onset potentials for the Pt and Pt/Au disks are lower than that of the Au disk, which does not oxidize ethanol until 0.75 V vs. RHE. For the Au disk, the maximum occurs at ~1.5 V vs. RHE. The Pt/C catalyst produces less current than the Pt disk electrode (Figure 6.8b), but follows the same trend. Au/C and the Au disk, however, both achieve the same maximum current density.

The Pt/Au disk achieves a higher maximum current density than the Pt disk. This may be due to the uncovered Au substrate participating in the reaction at potentials above the oxidation onset potential of the Au disk. This is also apparent by the appearance of small shoulders in the CVs of the Pt/Au disk and Pt/Au/C corresponding to the formation of AuO.

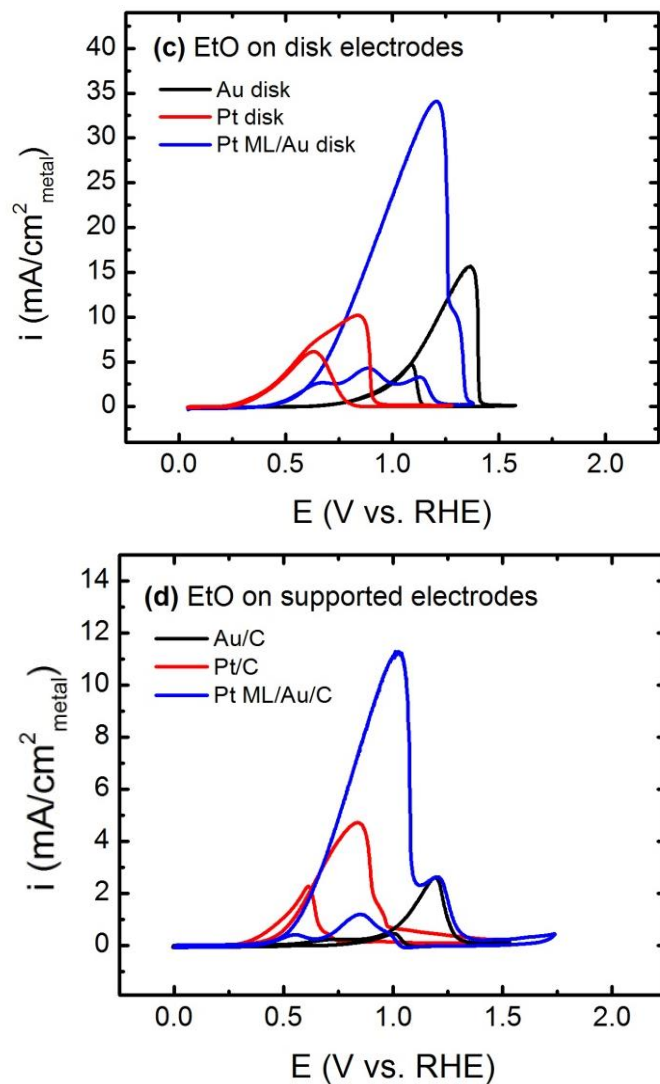


Figure 6.8: CVs of the (a) Pt, Au, and Pt/Au disk electrodes and (b) Pt/C, Au/C, and Pt ML/Au/C electrodes in 0.1 M KOH and 1 M EtOH.

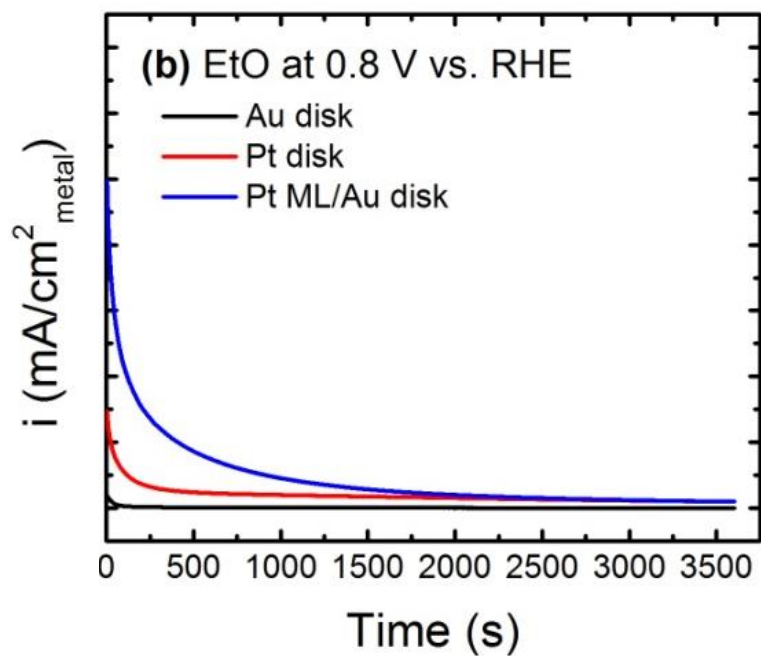


Figure 6.9: CA measurements for the Au, Pt, and Pt/Au disk electrodes taken at 0.8 V vs. RHE in Ar-purged 0.1 M KOH and 1 M EtOH.

### 6.3.2 Mechanistic Interpretation of EtO on Pt/Au Using FTIR

The mechanisms of EtO on Au, Pt, and Pt/Au were analyzed using in-situ FTIR (Figure 6.9), according to peak assignments found in the literature (Table 6.3).

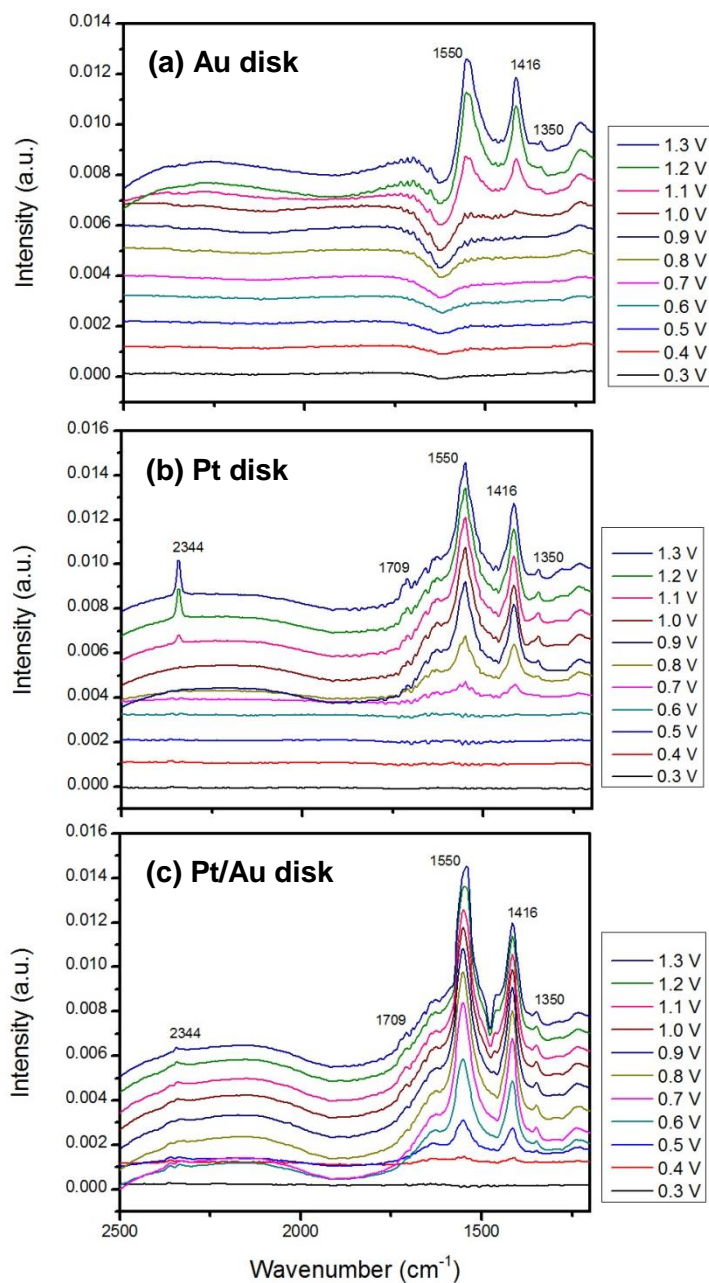


Figure 6.9: FTIR spectra of the (a) Au disk, (b) Pt disk, and (c) Pt/Au disk during EtO. Spectra were obtained in 0.1 M KOH and 0.2 M EtOH purged in N<sub>2</sub>. The scan rate was 1 mV/s.

Table 6.3: Peak assignments for the IR spectra of EtO.

Wavenumber ( $\text{cm}^{-1}$ )	Functional Group	Assignment
2341	$\text{CO}_2$	O-C-O asymmetric stretching[114]
1709	CHO or COOH	C=O stretching of acetaldehyde or acetic acid[114]
1550	COO-	O-C-O asymmetric stretching[114]
1414	COO-	O-C-O symmetric stretching[114]
1350	$\text{CH}_3$	$\text{CH}_3$ bending in acetaldehyde[114]

The oxidation mechanisms of EtO on Pt and Au in alkaline conditions have been well studied.[114–116] In short, ethanol is reacted through a pathway that either breaks the C-C bond, leading to the more complete oxidation of the alcohol to form  $\text{CO}_2$ , or one that leaves the C-C bond intact to produce incompletely oxidized species such as acetate and acetaldehyde. In the context of fuel utility, the former mechanism is preferred due to a higher faradaic efficiency. On Pt in 0.1 M KOH, both mechanisms occur, as evident by the appearance of the  $\text{CO}_2$  band ( $2341 \text{ cm}^{-1}$ ) as well as the two large peaks corresponding to acetate formation ( $1550 \text{ cm}^{-1}$  and  $1414 \text{ cm}^{-1}$ ). Acetaldehyde and acetic acid are also evident due to the appearance of peaks at  $1709 \text{ cm}^{-1}$  and  $1350 \text{ cm}^{-1}$ . On Au, the dominant IR peaks belong to acetate ( $1550 \text{ cm}^{-1}$  and  $1414 \text{ cm}^{-1}$ ) and acetaldehyde ( $1350 \text{ cm}^{-1}$ ), meaning no  $\text{CO}_2$  is produced. It is well established that Au does not break the C-C bond under these conditions.[115,117]

The Pt/Au disk has a similar IR spectra to the Pt disk, though far less CO<sub>2</sub> is produced and the dominant peaks belong to acetate. However, the onset potential of oxidation activity for Pt/Au is much lower than bulk Au.

The vast majority of oxidation products in these conditions are glycolaldehyde and glycolic acid, which are incomplete oxidation products from adsorbed ethylene glycol on the Pt surface.[118]

## Chapter 7

### CONCLUSIONS AND FUTURE DIRECTIONS

The focus of this dissertation was to investigate and develop supported catalysts for the oxidation of fuels for HEMFC. HEMFCs have been touted as being possible replacements of PEMFCs due to several opportunities to lower the overall cost. First, the actual polymer membranes used in HEMFCs are less expensive than Nafion, which is used in PEMFCs. Second, more metal catalysts are stable in the alkaline environment of HEMFCs, unlike in acidic electrolytes where many metals are not. Since Pt-group metals are the only stable and active electrocatalysts for PEMFCs, the cost of the electrodes remains high. If less expensive electrocatalysts can be developed for the alkaline HOR and ORR for HEMFCs, then the cost of the HEMFC could potentially be reduced.

However, the kinetics of the HOR and ORR are subject to change with the increased pH. The ORR, which is the main source of potential losses in PEMFCs, remains just as sluggish in alkaline electrolytes. The wider range of electrocatalysts available for the reaction may drive the development of a less expensive electrocatalyst for the alkaline ORR in order to decrease the potential losses from the fuel cell cathode. The anode, where the HOR reaction occurs, experiences little to no kinetic losses in acidic electrolytes, as the HOR is extremely fast on Pt. In alkaline electrolytes, however, the HOR is much slower than in acidic electrolytes, which requires either a higher Pt loading on the anode, or a less expensive, active catalyst.

The majority of this dissertation focuses on developing new catalysts for the alkaline HOR, with an emphasis on supported catalysts. While some work has been done studying catalytic trends of disk electrodes for the alkaline HOR/HER, disk electrodes or metal foils cannot be used in actual fuel cell devices. Therefore, Chapter 3 focused on comparing the catalytic trends for alkaline HOR/HER on monometallic supported electrodes to those developed for the disk electrodes. Carbon supported catalysts are standard electrocatalysts for fuel cells and therefore the trends on these surfaces are more relevant to HEMFC catalyst development. Therefore, a volcano plot consisting of the activity of several monometallic, carbon supported catalysts correlated to the hydrogen binding energy was compared to the one for the disk electrodes. Pt/C was found to be the most active for alkaline HOR/HER due to its intermediate hydrogen binding energy, while catalysts with weaker or stronger hydrogen binding energies were less active. This also occurs for the disk electrodes, but Cu/C, Au/C, and Ag/C were found to be significantly more active than the respective disk electrodes.

In Chapter 4, an Au disk electrode and supported Au/C particles were modified with Pt via the galvanic displacement of an underpotentially deposited monolayer of copper and tested for the alkaline HOR/HER. These Pt/Au and Pt/Au/C catalysts were found to have similar activity as the Pt disk and Pt/C electrodes. Further characterization of the Pt/Au catalysts confirms that the active sites on the surface are small Pt nanoparticles. Considering that the Pt/Au catalysts retain a Pt-like HOR/HER activity while utilizing very little Pt, these catalysts offer a possible route to decreasing the anode cost of HEMFCs.

Since Au is still an expensive metal, using it as a substrate will not significantly reduce the cost of the catalyst. Therefore, Chapter 5 focuses on finding a less expensive support for Pt in the form of TMC powders. 5% Pt/NbC, 5% Pt/TaC, 5% Pt/TiC, 5% Pt/VC, and 5% Pt/ZrC were synthesized via incipient wetness impregnation and then tested for the alkaline HOR. Each catalyst was found to have activity similar to bulk Pt/C or slightly lower.

One major conclusion from these studies is that any expected electronic tuning of Pt from the catalyst support will be less noticeable for powder catalysts. For instance, depositing a Pt monolayer on a single crystalline Au substrate will tune the hydrogen binding energy of the Pt, making the surface less active for HOR. However, this effect is essentially negligible for powder catalysts where the active Pt is in the nanoparticle state and is not as affected by the substrate.

While hydrogen is an ideal fuel for HEMFCs, the production of hydrogen from primarily fossil fuel sources and difficulties in storage for mobile applications have caused some scrutiny for its commercial viability. CO<sub>2</sub>-neutral fuels such as EG, Glc, and EtOH can be produced from biomass and used as fuels for HEMFCs as well. However, the oxidation of these fuels on the HEMFC anode also requires expensive electrocatalysts. Therefore, the Pt/Au catalysts were also tested for the oxidation of these fuels in alkaline electrolytes and were compared to pure Pt and Au catalysts for the electrocatalysis of EGO, GlcO, and EtO in alkaline conditions. For EGO the Pt/Au disk electrode and Pt/Au/C have a similar onset potential as the Pt disk and Pt/C, respectively. Pt/Au catalysts are more stable for EGO than either Pt or Au. Using *in-situ* FTIR, it was confirmed that Pt/Au does not break the C-C bond in EG. For GlcO, the Pt/Au surface shows behavior similar to Au and provides a current density that is

slightly higher than Pt. Both Pt and Pt/Au are active for breaking the C-C bond in Glc, as indicated by the presence of CO<sub>2</sub> in the FTIR spectra.

While the goal of this work was to develop new catalysts for HEMFCs, all studies were completed in 0.1 M KOH to best simulate the environment of a fuel cell. However, fuel cell electrodes are more complex and contain an interface between the catalyst, the polymer membrane, and the gas. While the activities of the catalysts tested in this dissertation are not expected to change significantly between an electrochemical cell and actual device, they must be tested in a more realistic environment before they can be implemented.

First, it is recommended that the HOR kinetics of each catalyst be measured in a H<sub>2</sub>-pump set up, which is being developed for HEMFCs currently in the Yan lab. This is done in a traditional fuel cell testing station, but only the HOR kinetic are measured on the anode. This allows polarization curves similar to be gathered to those obtained in the electrochemical set up used in this dissertation. The same methods can also be used to extract exchange current densities as well as other kinetic data in the same fashion. This would allow the comparison of activities in an RDE set up and a fuel cell set up so the effect of the polymer membrane on the HOR kinetics can be analyzed.

After this is completed, the catalysts can then be tested in a normal fuel cell testing device. Here, the cathode would be a high loading of Pt in order to minimize potential losses from the alkaline ORR. An interesting study would be to continue the scale up strategy employed in Chapter 3 and create volcano plots for each supported catalyst using kinetic data obtained from the fuel cell testing station using the same hydrogen binding energies.

The hydrogen binding energies used in Chapter 3 were calculated using DFT in a simple system consisting of a single crystalline surface and hydrogen in a vacuum. These values are applicable for establishing trends as has been done in this dissertation, but may not accurately represent the system being measured. For instance, one way to further explore the differences between the Au, Ag, and Cu disk and supported electrodes in Chapter 3 would be to calculate hydrogen binding energies in more realistic environments such as in the presence of an electrolyte or on a stepped surface to see if the hydrogen binding energy on the nanoparticle surface is actually weaker than predicted.

In the case of the Pt/TMC catalysts, only Pt loadings of 5% were synthesized. Some of these catalysts had very low dispersion, which caused a higher amount of error in the average activities calculated. One way to further investigate the effect of the substrate on the activity of the Pt would be to first find a new synthesis method to increase the dispersion of the catalyst. In addition, a wider range of Pt loadings should be tested to see how the activity of the catalysts changes with the wt% of Pt impregnated onto the TMC support.

## REFERENCES

- [1] M.K. Mathe, T. Mkwizu, M. Modibedi, *Energy Procedia* 29 (2012) 401.
- [2] N. Ji, M. Zheng, A. Wang, T. Zhang, J.G. Chen, *ChemSusChem* 5 (2012) 939.
- [3] R.B. de Lima, V. Paganin, T. Iwasita, W. Vielstich, *Electrochim. Acta* 49 (2003) 85.
- [4] H. Yue, Y. Zhao, X. Ma, J. Gong, *Chem. Soc. Rev.* 41 (2012) 4218.
- [5] M. Saliccioli, W. Yu, M. a Barteau, J.G. Chen, D.G. Vlachos, *J. Am. Chem. Soc.* 133 (2011) 7996.
- [6] A.L. Stottlemyer, H. Ren, J.G. Chen, *Surf. Sci.* 603 (2009) 2630.
- [7] A. Brouzgou, L.L. Yan, S.Q. Song, P. Tsiakaras, *Appl. Catal. B Environ.* 147 (2014) 481.
- [8] J. Spendelow, J. Marcinkoski, DOE Fuel Cell Technologies Office Record #14012, 2014.
- [9] W. Sheng, H.A. Gasteigert, Y. Shao-Horn, *J. Electrochem. Soc.* 157 (2010) B1529.
- [10] S. Lu, J. Pan, A. Huang, L. Zhuang, J. Lu, *PNAS* 105 (2008) 20611.
- [11] G.F. Mclean, T. Niet, N. Djilali, *Int. J. Hydrogen Energy* 27 (2002) 507.
- [12] J.R. Varcoe, R.C.T. Slade, *Fuel Cells* 5 (2005) 187.
- [13] K.J. Vetter, *Electrochemical Kinetics: Theoretical and Experimental Aspects*, Academic Press, New York, 1967.
- [14] J.K. Nørskov, T. Bligaard, a. Logadottir, J.R. Kitchin, J.G. Chen, S. Pandelov, U. Stimming, *J. Electrochem. Soc.* 152 (2005) J23.
- [15] W. Sheng, M.N.Z. Myint, J. Chen, Y. Yan, *Energy Environ. Sci.* (2013).

- [16] W. Sheng, M. Myint, J.G. Chen, Y. Yan, (2013).
- [17] A. Bard, L. Faulkner, *Electrochemical Methods: Fundamentals and Applications*, 2nd ed., John Wiley and Sons, 2001.
- [18] J. Durst, a. Siebel, C. Simon, F. Hasché, J. Herranz, H. a. Gasteiger, *Energy Environ. Sci.* 7 (2014) 2255.
- [19] Y.-C. Lu, H. a Gasteiger, Y. Shao-Horn, *J. Am. Chem. Soc.* 133 (2011) 19048.
- [20] R.R. Adzic, J. Zhang, K. Sasaki, M.B. Vukmirovic, M. Shao, J.X. Wang, a. U. Nilekar, M. Mavrikakis, J. a. Valerio, F. Uribe, *Top. Catal.* 46 (2007) 249.
- [21] M. Shao, A. Peles, K. Shoemaker, M. Gummalla, P.N. Njoki, J. Luo, C.-J. Zhong, *J. Phys. Chem. Lett.* 2 (2011) 67.
- [22] F.J. Vidal-iglesias, R.M. Ara, J. Solla-gullo, E. Herrero, J.M. Feliu, *ACS Catal.* 2 (2012) 901.
- [23] G. Garcia, M.T.M. Koper, *ChemPhysChem* 12 (2011) 2064.
- [24] P. Rodríguez, G. García, E. Herrero, J.M. Feliu, M.T.M. Koper, *Electrocatalysis* 2 (2011) 242.
- [25] C.L. Green, A. Kucernak, 2 (2002) 1036.
- [26] J.G. Becerra, R.C. Salvarezza, A.J. Arvia, *Electrochim. Acta* 33 (1988) 1431.
- [27] Q. Lu, J. Rosen, Y. Zhou, G.S. Hutchings, Y.C. Kimmel, J.G. Chen, F. Jiao, *Nat. Commun.* 5 (2014) 3242.
- [28] C. Coutanceau, L. Demarconnay, C. Lamy, J.M. Léger, *J. Power Sources* 156 (2006) 14.
- [29] A. Hamelin, M.J. Sottomayor, F. Silva, S. Chang, M.J. Weaver, *J. Electroanal. Chem.* 295 (1990) 291.
- [30] A. Michri, A. Pshchenichikov, R. Burshtein, *Elektrokhimiya* 8 (1972) 351.
- [31] H. Angerstein-Kozłowska, B.E. Conway, A. Hamelin, L. Stoicoviciu, *J. Electroanal. Chem.* 228 (1987) 429.
- [32] S. Trasatti, O.A. Petrii, *J. Electroanal. Chem.* 327 (1992) 353.

- [33] N. Pentland, J.O. Bockris, E. Sheldon, *J. Electrochem. Soc.* 104 (1957) 182.
- [34] B.S. Yeo, A.T. Bell, *J. Am. Chem. Soc.* 133 (2011) 5587.
- [35] W. Sheng, M. Myint, J.G. Chen, Y. Yan, *Energy Environ. Sci.* 6 (2013) 1509.
- [36] O. Barbieri, M. Hahn, a. Herzog, R. Kötz, *Carbon N. Y.* 43 (2005) 1303.
- [37] S. Fletcher, R.G. Barradas, J.D. Porter, *J. Electrochem. Soc.* 125 (1978) 1960.
- [38] T. Pauporte, F. Andolfatto, R. Durand, *Electrochim. Acta* 45 (1999) 431.
- [39] V. Ganesh, V. Lakshminarayanan, *Electrochim. Acta* 49 (2004) 3561.
- [40] J.L. Weininger, M.W. Breiter, *J. Electrochem. Soc.* 111 (1964) 707.
- [41] D. Strmcnik, M. Uchimura, C. Wang, R. Subbaraman, N. Danilovic, D. Van Der Vliet, A.P. Paulikas, V.R. Stamenkovic, N.M. Markovic, *Nat. Chem.* (2013) 1.
- [42] P.N.R. Jr, N.M. Markovic, (n.d.).
- [43] N.M. Markovic, S.T. Sarraf, H.A. Gasteigert, P.N. Ross, *J. Chem. Soc.* 92 (1996) 3719.
- [44] T.J. Schmidt, H.A. Gasteiger, G.D. Stab, P.M. Urban, D.M. Kolb, R.J. Behm, *J. Electrochem. Soc.* 145 (1998) 2354.
- [45] R. Subbaraman, D. Tripkovic, D. Strmcnik, K.-C. Chang, M. Uchimura, A.P. Paulikas, V. Stamenkovic, N.M. Markovic, *Science* (80-. ). 334 (2011) 1256.
- [46] W. Sheng, Z. Zhuang, M. Gao, J. Zheng, J.G. Chen, Y. Yan, *Nat. Commun.* 6 (2015) 5848.
- [47] D.A.J. Rand, R. Woods, *Electroanal. Chem. Interfacial Electrochem.* 31 (1971) 29.
- [48] Y. Wang, G. Wang, G. Li, B. Huang, J. Pan, Q. Liu, J. Han, L. Xiao, J. Lu, L. Zhuang, *Energy Environ. Sci.* 8 (2015) 177.
- [49] J. Radnik, C. Mohr, P. Claus, *Phys. Chem. Chem. Phys.* 5 (2002) 172.
- [50] M. Haruta, *Catal. Today* 36 (1997) 153.

- [51] S. Kumar, S. Zou, *Langmuir* 25 (2009) 574.
- [52] W. Sheng, A.P. Bivens, M. Myint, Z. Zhuang, R. V. Forest, Q. Fang, J.G. Chen, Y. Yan, *Energy Environ. Sci.* 7 (2014) 1719.
- [53] J. Zhang, M.B. Vukmirovic, K. Sasaki, A.U. Nilekar, M. Mavrikakis, R.R. Adzic, (2005) 12480.
- [54] K. Sasaki, J.X. Wang, H. Naohara, N. Marinkovic, K. More, H. Inada, R.R. Adzic, *Electrochim. Acta* 55 (2010) 2645.
- [55] K. Gong, D. Su, R.R. Adzic, *J. Am. Chem. Soc.* 132 (2010) 14364.
- [56] D. V. Esposito, J.G. Chen, *Energy Environ. Sci.* 4 (2011) 3900.
- [57] D. V Esposito, S.T. Hunt, Y.C. Kimmel, J.G. Chen, *J. Am. Chem. Soc.* 134 (2012) 3025.
- [58] D. V Esposito, S.T. Hunt, A.L. Stottlemeyer, K.D. Dobson, B.E. McCandless, R.W. Birkmire, J.G. Chen, *Angew. Chem. Int. Ed. Engl.* 49 (2010) 9859.
- [59] D. Friebel, V. Viswanathan, D.J. Miller, T. Anniyev, H. Ogasawara, A.H. Larsen, C.P. O'Grady, J.K. Nørskov, A. Nilsson, *J. Am. Chem. Soc.* 134 (2012) 9664.
- [60] K. Sasaki, Y. Mo, J.X. Wang, M. Balasubramanian, F. Uribe, J. McBreen, R.R. Adzic, *Electrochim. Acta* 48 (2003) 3841.
- [61] H. Angerstein-Kozłowska, B.E. Conway, B. Barnett, J. Mozota, *J. Electroanal. Chem.* 100 (1979) 417.
- [62] A. Hamelin, *J. Electroanal. Chem.* 407 (1996) 1.
- [63] O.M. Magnussen, J. Hotlos, G. Beitel, D.M. Kolb, R.J. Behm, *J. Vac. Sci. Technol. B Microelectron. Nanom. Struct.* 9 (1991) 969.
- [64] I.H. Omar, H.J. Pauling, K. Juttner, *J. Electrochem. Soc.* 140 (1993) 2187.
- [65] T. Hachiya, H. Honbo, K. Itaya, *J. Electroanal. Chem.* 315 (1991) 275.
- [66] S. Cheng, R.E. Rettew, M. Sauerbrey, F.M. Alamgir, *ACS Appl. Mater. Interfaces* 3 (2011) 3948.

- [67] F.M. Alamgir, A. Vitale, (2013) 2392.
- [68] R.J. Randler, D.M. Kolb, B.M. Ocko, I.K. Robinson, *Surf. Sci.* 447 (2000) 187.
- [69] F.A. Moller, O.M. Magnussen, R.J. Behm, *Phys. Rev. B* 51 (1995) 2484.
- [70] R.E. Rettew, S. Cheng, M. Sauerbrey, T. a. Manz, D.S. Sholl, C. Jaye, D. a. Fischer, F.M. Alamgir, *Top. Catal.* 56 (2013) 1065.
- [71] E.G. Mahoney, W. Sheng, Y. Yan, J.G. Chen, *ChemElectroChem* 1 (2014) 2058.
- [72] T. Vidaković, M. Christov, K. Sundmacher, *Electrochim. Acta* 52 (2007) 5606.
- [73] G. Garcia, P. Rodriguez, S. Frank, A.A. Koverga, M.T.M. Koper, *ECS Trans.* 25 (2009) 203.
- [74] M.T.M. Koper, *Nanoscale* 3 (2011) 2054.
- [75] J.S. Spendelow, J.D. Goodpaster, P.J. a Kenis, a Wieckowski, *J. Phys. Chem. B* 110 (2006) 9545.
- [76] T.J. Schmidt, P.N. Ross, N.M. Markovic, *J. Phys. Chem. B* 105 (2001) 12082.
- [77] E. Herrero, Q.-S. Chen, J. Hernández, S.-G. Sun, J.M. Feliu, *Phys. Chem. Chem. Phys.* 13 (2011) 16762.
- [78] N.P. Lebedeva, M.T.M. Koper, J.M. Feliu, R. a. van Santen, *J. Phys. Chem. B* 106 (2002) 12938.
- [79] G. Garcia, M.T.M. Koper, *Phys. Chem. Chem. Phys.* 10 (2008) 3802.
- [80] M.J.S. Farias, F.J. Vidal-Iglesias, J. Solla-Gullón, E. Herrero, J.M. Feliu, *J. Electroanal. Chem.* 716 (2014) 16.
- [81] F. Maillard, S. Pronkin, E.R. Savinova, in: M.T.M. Koper (Ed.), *Fuel Cell Catal. A Surf. Sci. Approach*, Wiley, Hoboken, NJ, 2009, pp. 507–566.
- [82] A. Rodes, R. Go, J.M. Feliu, M.J. Weaver, *Langmuir* 16 (2000) 811.
- [83] A.M. Gomez-Marin, J.P. Hernandez-Ortiz, *J. Phys. Chem. C* 118 (2014) 2475.

- [84] P. Rodriguez, G. Garcia, E. Herrero, J.M. Feliu, M.T.M. Koper, *Electrocatalysis* 2 (2011) 242.
- [85] M.J.S. Farias, E. Herrero, J.M. Feliu, *J. Phys. Chem. C* 117 (2013) 2903.
- [86] A. Cuesta, A. Couto, A. Rincón, M.C. Pérez, A. López-Cudero, C. Gutiérrez, *J. Electroanal. Chem.* 586 (2006) 184.
- [87] B.L. Abrams, P.C.K. Vesborg, J.L. Bonde, T.F. Jaramillo, I. Chorkendorff, *J. Electrochem. Soc.* 156 (2009) B273.
- [88] M.Ø. Pedersen, S. Helveg, a. Ruban, I. Stensgaard, E. Lægsgaard, J.K. Nørskov, F. Besenbacher, *Surf. Sci.* 426 (1999) 395.
- [89] C. Menning, J.G. Chen, *J. Chem. Phys.* 130 (2009) 174709.
- [90] J. Durst, A. Siebel, S. Simon, F. Hasche, J. Herranz, H.A. Gasteiger, *Energy Environ. Sci.* (2014).
- [91] Y. Shao-Horn, W.C. Sheng, S. Chen, P.J. Ferreira, E.F. Holby, D. Morgan, *Top. Catal.* 46 (2007) 285.
- [92] R.B. Levy, M. Boudart, *Science* (80-. ). 181 (1973) 547.
- [93] I.J. Hsu, D. a. Hansgen, B.E. Mccandless, B.G. Willis, J.G. Chen, *J. Phys. Chem. C* 115 (2011) 3709.
- [94] Y.C. Kimmel, X. Xu, W. Yu, X. Yang, J.G. Chen, *ACS Catal.* 4 (2014) 1558.
- [95] A.I. Danilov, R.R. Nazmutdinov, T.T. Zinkicheva, E.B. Molodkina, A. V. Rudnev, Y.M. Polukarov, J.M. Feliu, *Russ. J. Electrochem.* 44 (2008) 697.
- [96] I.J. Hsu, D. V. Esposito, E.G. Mahoney, A. Black, J.G. Chen, *J. Power Sources* 196 (2011) 8307.
- [97] H.J. Kim, S.M. Choi, S. Green, G. a. Tompsett, S.H. Lee, G.W. Huber, W.B. Kim, *Appl. Catal. B Environ.* 101 (2011) 366.
- [98] S.C. Chang, Y. Ho, M.J. Weaver, *J. Am. Chem. Soc.* 113 (1991) 9506.
- [99] F. Kadirgan, C. Lamy, J.M. Lkger, B. Beden, *J. Electroanal. Chem.* 286 (1990) 41.

- [100] A. Falase, M. Main, K. Garcia, A. Serov, C. Lau, P. Atanassov, *Electrochim. Acta* 66 (2012) 295.
- [101] L. Wang, H. Meng, P.K. Shen, C. Bianchini, F. Vizza, Z. Wei, *Phys. Chem. Chem. Phys.* 13 (2011) 2667.
- [102] L. Demarconnay, S. Brimaud, C. Coutanceau, J.-M. Léger, *J. Electroanal. Chem.* 601 (2007) 169.
- [103] P.A. Christensen, A. Hamnet, *J. Electroanal. Chem.* 260 (1989) 347.
- [104] Y. Kwon, S.C.S. Lai, P. Rodriguez, M.T.M. Koper, *J. Am. Chem. Soc.* 133 (2011) 6914.
- [105] M. Pasta, F. La Mantia, Y. Cui, *Electrochim. Acta* 55 (2010) 5561.
- [106] R.R. Adzic, M.W. Hsiao, E.B. Yeager, *J. Electroanal. Chem.* 260 (1989) 475.
- [107] K. Kokoh, J.-M. Leger, B. Beden, H. Huser, C. Lamy, *Electrochim. Acta* 37 (1992) 1909.
- [108] I.T. Bae, E. Yeager, X. Xing, C.C. Liu, *J. Electroanal. Chem. Interfacial Electrochem.* 309 (1991) 131.
- [109] L.H. Essis Yei, B. Beden, C. Lamy, *J. Electroanal. Chem* 246 (1988) 349.
- [110] M.F.L. de Mele, H.A. Videla, A.J. Arvia, *Bioelectrochemistry Bioenerg.* 10 (1983) 239.
- [111] Y.B. Vassilyev, O.A. Khazova, N.N. Nikolaeva, *J. Electroanal. Chem.* 196 (1985) 105.
- [112] K.D. Popovic, N.M. Markovic, A. V Tripkovic, R.R. Adzic, *J. Electroanal. Chem.* 313 (1991) 181.
- [113] B. Beden, F. Largeaud, K.B. Kokoh, C. Lamy, *Electrochim. Acta* 41 (1996) 701.
- [114] S.C.S. Lai, S.E.F. Kleijn, F.T.Z. Öztürk, V.C. van Rees Vellinga, J. Koning, P. Rodriguez, M.T.M. Koper, *Catal. Today* 154 (2010) 92.
- [115] G. Catalysis, Y. Kwon, S.C.S. Lai, P. Rodriguez, M.T.M. Koper, (2011) 6914.
- [116] S.C.S. Lai, M.T.M. Koper, *Phys. Chem. Chem. Phys.* 11 (2009) 10446.

- [117] G. Tremiliosi-filho, E.R. Gonzalez, A.J. Motheo, E.M. Belgsir, J.M. Leger, C. Lamy, J. Electroanal. Chem 444 (1998) 31.
- [118] J. Schnaidt, M. Heinen, Z. Jusys, R.J. Behm, Catal. Today 202 (2013) 154.



## Reprint Permission for Figure 1.8:

### ROYAL SOCIETY OF CHEMISTRY LICENSE TERMS AND CONDITIONS

Jul 20, 2015

This is a License Agreement between Elizabeth Mahoney ("You") and Royal Society of Chemistry ("Royal Society of Chemistry") provided by Copyright Clearance Center ("CCC"). The license consists of your order details, the terms and conditions provided by Royal Society of Chemistry, and the payment terms and conditions.

**All payments must be made in full to CCC. For payment instructions, please see information listed at the bottom of this form.**

License Number	3673161227972
License date	Jul 20, 2015
Licensed content publisher	Royal Society of Chemistry
Licensed content publication	Energy & Environmental Science
Licensed content title	Correlating the hydrogen evolution reaction activity in alkaline electrolytes with the hydrogen binding energy on monometallic surfaces
Licensed content author	Wenchao Sheng, MyatNoeZin Myint, Jingguang G. Chen, Yushan Yan
Licensed content date	Apr 2, 2013
Volume number	6
Issue number	5
Type of Use	Thesis/Dissertation
Requestor type	academic/educational
Portion	figures/tables/images
Number of figures/tables/images	1
Format	print
Distribution quantity	3
Will you be translating?	no
Order reference number	None
Title of the thesis/dissertation	The Development of Supported Electrocatalysts for the Oxidation of Fuels in Hydroxide Exchange Membrane Fuel Cells
Expected completion date	Aug 2015
Estimated size	150
Total	0.00 USD

#### Terms and Conditions

This License Agreement is between {Requestor Name} ("You") and The Royal Society of Chemistry ("RSC") provided by the Copyright Clearance Center ("CCC"). The license consists of your order details, the terms and conditions provided by the Royal Society of Chemistry, and the payment terms and conditions.